MSc thesis Geoscience & Remote Sensing

Retrieving the Median Volume Diameter with a Polarimetric Cloud Radar

Y.A. van den Brule
January, 2022

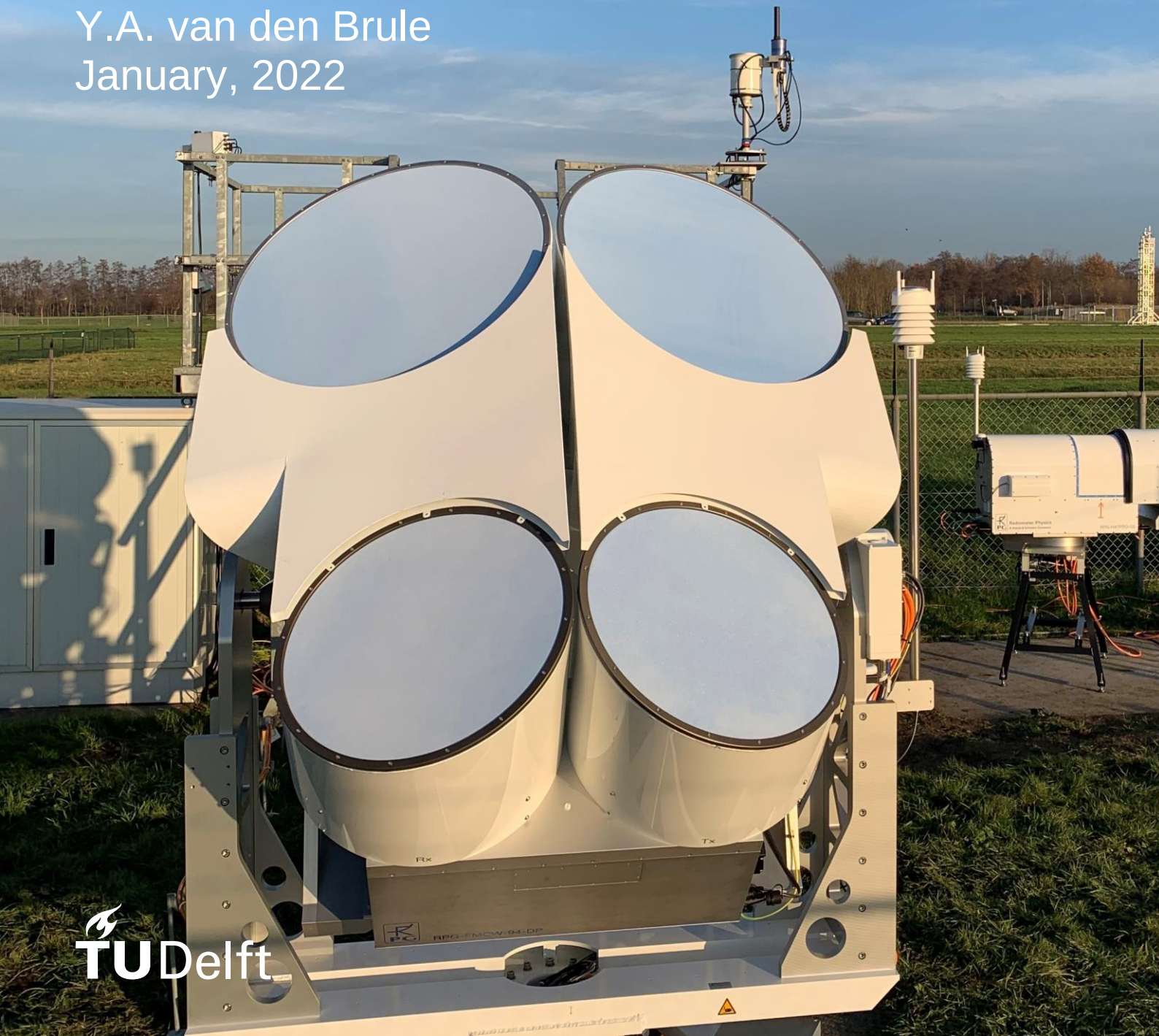

TU Delft

Retrieving the Median Volume Diameter with a Polarimetric Cloud Radar

by

Yannick Anthonius van den Brule

to obtain the degree of Master of Science
at the Delft University of Technology,
to be defended publicly on Monday January 17, 2022 at 2:00 PM.

Student number:	4493672	
Project duration:	February 12, 2021 – January 17, 2022	
Thesis committee:	Ir. C.M.H. Unal,	TU Delft, Supervisor/Chair
	Prof.Dr.Ir. H.W.J. Russchenberg,	TU Delft
	Dr.Ir. M.A. Schleiss,	TU Delft
	Dr.sc. F. Glassmeier,	TU Delft

TU Delft

Acknowledgements

During my master thesis, I have had help from people that I would like to thank.

Firstly, I would like to thank my supervisor Ir. Christine Unal for all the help during this thesis. We have had a zoom meeting of about 2 hours every week which were invaluable for my research. I really enjoyed all these meetings. At every meeting, I gave a small Powerpoint presentation, were I showed what I had achieved in the last week. She always gave me good advice and helped me to understand the radar meteorology topic better. What I really appreciated was that she always tried to help me and really wanted me to understand everything. It really felt like she would always say it if she knew something what could help me. She also helped me to get a good structure in my report and gave detailed feedback about all chapters that I wrote, which helped a lot to improve these chapters. I also want to thank her for providing me with the results of simulations that she made, which were essential in my research. At last, I want to thank her for all the help she gave via e-mail. She always replied quickly and extensive, what I really appreciate.

Secondly, I would like to thank PhD candidate Christos Gatidis for providing me with the mass-weighted mean diameter as a function of time measured by a disdrometer, which was very important for my research as I could use this to compare my thesis results with.

Thirdly, I would like to thank Prof.dr.ir. Herman Russchenberg, Dr.ir. Marc Schleiss and Dr.sc. Franziska Glassmeier for the advice during the mid-term review of this thesis. Especially the advice to focus on something and do a comparison with other instruments rather than to continue with a variety of research ideas.

At last, I would like to thank my girlfriend, friends and family for all their support and the nice time I had with them outside of my research.

Abstract

The knowledge of the raindrop size distribution is key for characterizing precipitation. It is however still a challenge to retrieve it with radars. Several polarimetric and spectral techniques are proposed for cm-wavelength radars (weather radars). What about the mm-wavelength radars (cloud radars), which have a better spatial and time resolution and can still measure light and moderate rain? Knowing that 90% of the rain volume in Europe comes from rainfall rates between 0.1 mm/h and 10 mm/h, this is worthwhile to investigate. The goal of this thesis is to retrieve 1 of the 3 parameters of the modelled gamma raindrop size distribution, the median volume diameter (D_0), during stratiform rainfall events using a slantwise profiling dual-frequency polarimetric cloud radar. Focus is given to phase measurements, which are not affected by attenuation. Simulations show that the differential backscatter phase (δ_{co}) strongly depends on D_0. At mm-wavelength, backscattering and propagation effects need to be disentangled first. To achieve this, an algorithm to detect and characterize Rayleigh plateaus is proposed and implemented. After the application of this algorithm, a methodology to estimate the differential backscatter phase and its error is given. The 95% confidence interval of δ_{co} is estimated with the re-sampling method bootstrapping.

Using simulation results, an attempt is made to find combinations of D_0 and the raindrop size distribution shape parameter μ that match with the confidence interval of δ_{co}. The confidence interval of δ_{co} restricts D_0, but not μ in most cases. This proposed technique is applied for both the 35 and 94 GHz frequency band of the new cloud radar at Cabauw (Ruisdael Observatory site near Utrecht). The resulting 95% confidence intervals of D_0 with 35 and 94 GHz and their overlap are compared with in-situ disdrometer measurements of the mass-weighted mean diameter (D_m) which is closely related to D_0. The median volume diameter retrieved with the 35 and 94 GHz frequency bands both shows a normalized cross correlation coefficient of 0.845 with the measured D_m of the disdrometer. Therefore, the cloud radar seems to have the capability to provide the detailed variations of the raindrops mean/median diameter like a local disdrometer, but at different heights. Nonetheless, the values differ. The disdrometer provides higher values than the cloud radar. One possible explanation is the inability of the disdrometer to measure raindrops smaller than 0.25 mm and the expected underestimation of the number of raindrops with sizes between 0.25 and 0.375 mm. However, because D_0 values retrieved from 35 GHz data are also higher than the ones at 94 GHz, further research, which can use all the methodologies proposed in this master thesis work, is needed to examine the quantitative values of the median volume diameter retrieval.

These techniques can be implemented for all the single-frequency cloud radars (94 GHz) of the national Ruisdael Observatory (cloud and precipitation profiling mobile station and Lutjewad site above Groningen).

Contents

Abstract v

1 Introduction 1
- 1.1 Why Raindrop Size Distribution? . . . 1
- 1.2 How to Determine the Raindrop Size Distribution? . . . 1
- 1.3 Research Questions . . . 2
- 1.4 Raindrop Size Distribution Model . . . 2
- 1.5 Radar Parameters . . . 3
  - 1.5.1 Doppler Spectra . . . 3
  - 1.5.2 Power Based Parameters . . . 3
  - 1.5.3 Phase Based Parameters . . . 5
- 1.6 Outline of the Report . . . 5

2 Literature Review 7
- 2.1 Cloud Radar . . . 7
  - 2.1.1 How Cloud Radar Works . . . 7
  - 2.1.2 Where are Cloud Radars Used for? . . . 7
  - 2.1.3 Limitations . . . 8
- 2.2 Cloud Radar for Rain Observations . . . 8
  - 2.2.1 Vertically Profiling . . . 9
  - 2.2.2 Slantwise Profiling . . . 11
- 2.3 Simulations . . . 11

3 Data, Error and Preprocessing 13
- 3.1 Used Cloud Radar . . . 13
- 3.2 Measurement Files . . . 13
- 3.3 Rainfall Event Selection . . . 15
- 3.4 Plotting Cloud Radar Variables . . . 16
- 3.5 Disdrometer . . . 18
- 3.6 Error Calculation . . . 18
  - 3.6.1 Confidence Interval of the Mean . . . 18
  - 3.6.2 Confidence Interval of the Difference of Two Dependent Variables . . . 18
- 3.7 Polarimetric Calibration Correction . . . 19
  - 3.7.1 Principle . . . 19
  - 3.7.2 Drizzle File Selection . . . 19
  - 3.7.3 Requirement in SNR . . . 20
  - 3.7.4 Polarimetric Calibration Corrections . . . 20

4 Estimating δ_{co} and K_{dp} after Disentangling Propagation and Backscattering 23
- 4.1 Rayleigh Plateau Detection . . . 23
  - 4.1.1 Step 1: Filtering out Data . . . 25
  - 4.1.2 Step 2: Look for Possible Rayleigh Plateaus . . . 26
  - 4.1.3 Step 3: Calculate Cost Function of all Possible Plateaus . . . 27
  - 4.1.4 Step 4: Repeat Steps 1-3 for other Heights and Times . . . 28
  - 4.1.5 Check Performance . . . 28
  - 4.1.6 Summary of Rayleigh Plateau Detection Method . . . 31

4.2 Estimating the Differential Backscatter Phase . . . 34
4.3 Estimating the Specific Differential Phase . . . 37
4.4 Polarimetric Calibration Results . . . 37
4.4.1 Spectral Differential Reflectivity and Spectral Differential Phase . . . 37
4.4.2 Differential Backscatter Phase . . . 40
4.4.3 Specific Differential Phase and Differential Propagation Phase . . . 40
4.5 Summary . . . 40

5 Retrieving the Median Volume Diameter 45
5.1 Consistency of the δ_{co} Estimation . . . 45
5.2 Estimating D_0 . . . 47
5.3 Consistency of the D_0 Estimation . . . 51
5.4 Comparing D_0 Estimates with Disdrometer Measurements . . . 52
5.4.1 Comparing D_0 with D_m . . . 53
5.4.2 Time Lag Correction . . . 54
5.4.3 Cross Correlation Between D_0 and D_m . . . 55
5.4.4 Observed Bias . . . 55
5.4.5 Recommendations . . . 57
5.4.6 Width of the Confidence Interval at 94 GHz . . . 58
5.4.7 Combined Method . . . 58

6 Conclusions and Recommendations 61
6.1 Answers to the Research Sub-questions . . . 61
6.1.1 Are the polarimetric measurements well calibrated? . . . 61
6.1.2 How to disentangle propagation and backscattering effects? . . . 61
6.1.3 How can the differential backscatter phase be estimated? . . . 61
6.1.4 How can the error of the differential backscatter phase be evaluated? . . . 62
6.1.5 How can the median volume diameter be retrieved from the estimate of the differential backscatter phase? . . . 62
6.1.6 How does the retrieved median volume diameter compare with disdrometer measurements? . . . 62
6.2 Answer to the Main Research Question . . . 63
6.3 Recommendations . . . 63

Bibliography 65

A Appendix A - Non Used Parameters 67
A.1 Power Based Parameters . . . 67
A.1.1 Linear Depolarization Ratio . . . 67
A.2 Phase Based Parameters . . . 68
A.2.1 Mean Doppler Velocity and Spectrum Width . . . 68
A.3 Remaining Parameters without Explanation . . . 69

B Appendix B - Polarimetric Calibration Correction Table 71

C Appendix C - Specific Differential Reflectivity 73

1 Introduction

This master thesis was written as part of the Geoscience and Remote Sensing track of Civil Engineering at Delft University of Technology. The research work relates to rain microphysics: the raindrop size distribution, which leads to the rainfall rate or the number of raindrops per m^3. Significant research has been carried out for retrieving the raindrop size distribution with weather radar polarimetric data. What about polarimetric cloud radars? In this master thesis, this new topic is explored.

In this chapter, first, the relevance of the raindrop size distribution is discussed in section 1.1, then in section 1.2 it will be discussed how the raindrop size distribution can be determined, next, in section 1.3 the research questions will be given. In section 1.4, it will be explained what approach will be used to be able to answer the research questions. Section 1.5 will introduce some useful parameters which are used in this research and finally, in section 1.6 the structure of this thesis will be discussed.

1.1. Why Raindrop Size Distribution?

Humans have always tried to understand the skies. Already 3000 years BC, in ancient Mesopotamia, people recorded the skies and created calendars based on the lunar cycle [1]. Observations and consequently the understanding of weather and climate have drastically improved. Because of this, people can even predict the weather. Relatively recent, the rise of computers made it possible to use computer algorithms and this led to more reliable weather predictions. A lot of different weather prediction algorithms exist at this moment, but the same general principle is always used: Measurements of the past are used in combination with a model to predict the future. As a result, the weather predictions depend highly on the quality of the measurements. Moreover, weather models, as well as climate models, are build by trying to understand observations. In conclusion, improving the quality of observations does not only directly improve the quality of weather/climate predictions, but also makes it possible to increase our understanding of weather/climate and therefore increase the quality of the models and consequently future predictions. The raindrop size distribution is such a parameter that is essential for a lot of meteorological research, like quantitative precipitation estimation and numerical modeling of micro-physical processes of rain formation and evolution [2]. Moreover, rainfall plays an important role in the Earths water and energy cycle and the duration and intensity of this rainfall are of interest for many Earth science applications [3]. The raindrop size distribution is an important parameter, as the liquid water content, the rainfall rate and the number of drops per m^3 are all a function of the raindrop size distribution. Furthermore, the raindrop size distribution gives information on the type of precipitation. A lot of small falling raindrops can for example result into the same rainfall rate as fewer bigger falling raindrops, but this difference cannot be noticed by only measuring rainfall intensity. In conclusion, the raindrop size distribution gives a detailed description of a rainfall event.

1.2. How to Determine the Raindrop Size Distribution?

The cheapest and easiest way to measure rainfall is using a rain gauge. However, this only results in the rain accumulation at one local point. This device cannot be used to measure the rain drop size distribution. A disdrometer however, which is an other in-situ measurement device, can be used for

this purpose. There are different type of disdrometers, varying from laser disdrometer to 2D video disdrometers, but they all measure raindrop sizes. A disadvantage of disdrometers is that they cannot accurately characterize the small raindrops in the raindrop size distribution [4]. Moreover, because it is an in-situ measurement device, the measurements are only representative for a small volume and this is usually on the surface. Polarimetric radars can also be used to retrieve the raindrop size distribution [5][6][7][8]. These retrieval methods make use of for example the reflectivity at horizontal polarization (z_h), the differential reflectivity (z_{dr}) and the specific differential phase (K_{dp}) [5] to retrieve the raindrop size distribution by using a weather radar (S-,C-,X-band). This thesis research uses a polarimetric cloud radar to retrieve the raindrop size distribution, which is a literature gap.

1.3. Research Questions

The context of this master thesis is the retrieval of the raindrop size distribution as a function of height and time during statiform rainfall events using a polarimetric cloud radar which is located at Cabauw. The overall research question is therefore:

- How can the median volume diameter (D_0) be retrieved using a polarimetric cloud radar?

To be able to answer the research question, the following sub-questions have been formulated:

1. Are the polarimetric measurements well calibrated?
2. How to disentangle propagation and backscattering effects?
3. How can the differential backscatter phase be estimated?
4. How can the error of the differential backscatter phase be evaluated?
5. How can the median volume diameter be retrieved from the estimate of the differential backscatter phase?
6. How does the retrieved median volume diameter compare with disdrometer measurements?

By answering the sub-questions in order, the research question will be answered. As can be seen in the sub-questions, the focus in this research is given to retrieve the median volume diameter, which is one of the three parameters of the gamma-modeled rain drop size distribution, as will be discussed in the next section.

1.4. Raindrop Size Distribution Model

Raindrop size distributions are often retrieved by first assuming a general distribution and by then estimating the parameters of the distribution. Two often used distributions are the (two-parameter) exponential distribution and the (three-parameter) gamma distribution. An exponential raindrop size distribution retrieval is easier, as one less parameter needs to be estimated, but the gamma distribution can approximate the real raindrop size distribution better. Exponential distributions are generally used if drop size distribution are averaged in space and/or time [9]. In this research, the raindrop size distribution is retrieved by using a gamma distribution. The gamma distribution is given in equation 1.1 [9]:

$$N(D) = N_w f(\mu) \left(\frac{D}{D_0}\right)^{\mu} \exp\left[-(3.67+\mu)\frac{D}{D_0}\right] \tag{1.1}$$

with

$$f(\mu) = \frac{6}{(3.67)^4} \frac{(3.67+\mu)^{\mu+4}}{\Gamma(\mu+4)} \tag{1.2}$$

where $N(D)$ is the raindrop size distribution in $\text{mm}^{-1}\text{m}^{-3}$, D is the raindrop diameter in mm, N_w is the intercept parameter in $\text{mm}^{-1}\text{m}^{-3}$, D_0 is the median volume diameter in mm, μ is the shape parameter and Γ is the gamma function. When μ equals 0, the gamma distribution is equal to the exponential distribution. In other words, the exponential distribution is a special case of the gamma distribution.

The introduction of the third parameter μ gives more flexibility regarding the shape of the distribution.

The research goal is to estimate the parameters N_w, D_0 and μ from radar variables to obtain a realistic model of the raindrop size distribution. To do this, it is necessary to know how these variables derived from radar measurements depend on N_w, D_0 and μ. These dependencies can be derived by using simulations of the whole propagation and scattering process in a rainfall event.

Possibilities are power measurements like the equivalent reflectivity factor at horizontal polarization (z_{hh}), the differential reflectivity (z_{dr}) and the differential attenuation (A_{dp}). A disadvantage of these first two measurements is that they suffer from attenuation and this means that first the attenuation should be determined. The total attenuation is the sum of the attenuation due to raindrops and the attenuation due to gasses. As estimating this attenuation is complex and it brings an extra uncertainty to the attenuated corrected variables, the focus in this research will be on phase measurements, which do not suffer from attenuation. There are two phase variables which might be of interest in this research, the differential backscatter phase (δ_{co}) and the specific differential phase (K_{dp}). The next section will elaborate on these parameters, among others. They first need to be derived from the measurements. Next, when the variables and simulations are combined, conclusions can be drawn about the parameters N_w, D_0 and μ. For example, the differential backscatter phase, mainly depends on D_0, a little bit on μ and is independent of N_w. Continuing with such an approach applied to different variables, the estimation of N_w, D_0 and μ could be obtained.

1.5. Radar Parameters

This section will focus on the meaning of some useful parameters in this research. As the use of Doppler spectra is necessary for determining some of the useful parameters, first, it will be explained what Doppler spectra are in subsection 1.5.1. Then in subsections 1.5.2 and 1.5.3 useful power and phase based parameters will be discussed, respectively. This introduction is based on the radar meteorology lectures of the master course Atmospheric Remote Sensing at Delft University of Technology.

1.5.1. Doppler Spectra

The used polarimetric cloud radar continuously measures Doppler spectra. This means that the measurements, for example the differential phase, are measured for different Doppler velocities. The differential phase is thus measured as a function of time, range and Doppler velocity. The Doppler velocity is the velocity component of the falling velocity of the raindrop in the direction of the radar. Without horizontal wind and turbulence, this would allow to calculate the falling velocity, as the elevation angle of the radar is known (45 deg). In practise, horizontal wind and turbulence make it challenging to do this. However, the Doppler velocity is still helpful in this research, as will be explained later in this thesis in section 4.1.

1.5.2. Power Based Parameters

Equivalent Reflectivity Factor

The equivalent reflectivity factor follows from the radar equation:

$$z_e = \frac{P_r r^2}{C_{wr}} \tag{1.3}$$

where z_e is the equivalent reflectivity factor in mm^6/m^3, P_r is the received power in W, r is the range in m and C_{wr} is a constant with the unit W m^5/mm^6, depending on the radar system. The equivalent reflectivity factor is not dependent on range, but the received power is. As the received power becomes less at higher range, the signal-to-noise ratio decreases at larger distance, which may lead to inaccurate results. Moreover, absorption of gasses and particles will lead to lower P_r values and when one does not correct for this, one will see a decrease of z_e as a result of this. The difference between the reflectivity factor and the equivalent reflectivity factor is that the equivalent reflectivity factor assumes the dielectric value of liquid water (K_w), even while observing hail or snow, the (actual) reflectivity factor could be calculated by using the following conversion:

$$z = z_e \frac{|K_w|^2}{|K|^2} \tag{1.4}$$

where K is the dielectric factor. As the equivalent reflectivity factor varies a lot during different precipitation intensities and types, usually a decibel scale is used. If one uses the standard definition of the decibel, one can calculate the equivalent reflectivity factor in decibel while using z_0, 1 mm^6/m^3, as a reference, this is usually called decibel relative to Z, or dBZ:

$$Z_e = 10 \log_{10} \left(\frac{z_e}{z_0} \right) \tag{1.5}$$

Where Z_e and z_e are the equivalent reflectivity factor in dBZ and mm^6/m^3, respectively. In the literature, the following equivalent definition is also used with the same units (dBZ and mm^6/m^3):

$$Z_e = 10 \log_{10} (z_e) \tag{1.6}$$

The equivalent reflectivity factor is useful because plots of Z_e quickly show critical information of the rainfall event. For example, one can see whether the rainfall is stratiform or convective. When the melting layer can be identified in the plot, the rainfall is called stratiform. In this research, only stratiform rainfall is considered. Moreover, one can see the melting layer in such a plot and thus one can estimate the melting layer height.

Differential Reflectivity

Differential reflectivity is defined as the horizontally polarized equivalent reflectivity factor (z_{hh}) divided by the vertically polarized one (z_{vv}):

$$z_{dr} = \frac{\left\langle |S_{hh}|^2 \right\rangle}{\left\langle |S_{vv}|^2 \right\rangle} = \frac{z_{hh}}{z_{vv}} \tag{1.7}$$

where z_{hh} and z_{vv} are in mm^6/m^3 and the S terms come from the scattering matrix:

$$\begin{bmatrix} E_h^s \\ E_v^s \end{bmatrix} = \begin{bmatrix} S_{hh} & S_{hv} \\ S_{vh} & S_{vv} \end{bmatrix} \begin{bmatrix} E_h^i \\ E_v^i \end{bmatrix} \tag{1.8}$$

where E is the electric field, s means scattered wave, i means incident wave, h stands for horizontal polarization and v stands for vertical polarization. Often, the differential reflectivity is expressed in dB:

$$Z_{dr} = 10 \log_{10} (z_{hh}) - 10 \log_{10} (z_{vv}) = Z_{hh} - Z_{vv} \tag{1.9}$$

The differential reflectivity depends on the particle shapes and permitivities. Spherical particles have a z_{dr} of 1, so a Z_{dr} of 0 dB. For rain, there is a relationship between size and shape. Small droplets are approximately spherical and bigger droplets are oblate spheroids. The following approximation can be used to see the relation between the shape of the raindrop and z_{dr} [9]:

$$z_{dr} = \frac{|S_{hh}|^2}{|S_{vv}|^2} \approx \left(\frac{b}{a} \right)^{-\frac{7}{3}} \tag{1.10}$$

where b and a are the two different radii of the oblate spheroid (raindrop) in m. When looking to the zenith, the cross section of the droplet is a circle with radius a. This means that this relation cannot be used when looking at the zenith and gives the best result when looking at an angle of 0 deg. It's easy to confirm that when the particle is spherical, so when $a = b$, z_{dr} is indeed equal to 1. Z_{dr} is high in rain and low in hail, so Z_{dr} is a good hail indicator. The differential reflectivity is largely weighted by the bigger particles, so oblate droplets and spherical hailstones would lead to a Z_{dr} of approximately 0 dB.

Equation 1.10 describes one raindrop in the Rayleigh scattering regime (weather radar). This equation is not valid anymore in the Mie scattering regime (cloud radar).

1.5.3. Phase Based Parameters

Differential Propagation Phase, Specific Differential Phase and Differential Backscatter Phase

The differential phase (Ψ_{dp}) can directly be calculated from the measurements, as will be explained in more detail in section 4.2. The differential phase is the sum of the differential propagation phase and the differential backscatter phase. The differential propagation phase Φ_{dp} is the phase shift that occurs between vertically and horizontally polarized waves, because horizontally polarized electromagnetic waves slow down more in rain than vertically polarized electromagnetic waves because of the oblate shape of raindrops (when not looking at the zenith). The differential propagation phase can be calculated in the following way:

$$\Phi_{dp} = 2\,(\Phi_{hh} - \Phi_{vv}) \tag{1.11}$$

where Φ_{hh} and Φ_{vv} are the propagation phases in deg with horizontal and vertical polarization, respectively. A well-known parameter in radar meteorology is the specific differential phase (K_{dp}), which is related to the propagation differential phase in the following way:

$$\Phi_{dp} \equiv 2K_{dp}r \tag{1.12}$$

where K_{dp} is the specific differential phase in deg/km.

Co-polar Correlation Coefficient

The co-polar correlation coefficient (ρ_{co}) is a statistical parameter that is between 0 and 1 which gives an indication of how uniform the sky is in terms of shape and relative permittivity of the medium with hydrometeors. A higher value means more uniformity. In rainfall, one can expect a value close to 1, while in hail, a mixture of rain and hail or wet aggregates, a lower value than 0.95 is expected. Moreover, clutter like birds will also lead to lower values of ρ_{co}. Because of the melting process, the melting layer is a non-uniform medium. Therefore, the co-polar correlation coefficient can also be used for melting layer detection. The mathematical definition of ρ_{co} is given in the following equation:

$$|\rho_{co}| = \left| \frac{\langle S_{hh}^{*} S_{vv} \rangle}{\sqrt{\langle |S_{hh}|^2 \rangle \langle |S_{vv}|^2 \rangle}} \right| \tag{1.13}$$

1.6. Outline of the Report

In chapter 2, a literature review on the topic is given, followed by chapter 3 which explains what data the cloud radar provides, how the errors are estimated in this research and how an extra polarimetric calibration is applied. After this, in chapter 4, it is explained how propagation and scattering effects are disentangled and how this is used for an estimation of the differential backscatter phase and the specific differential phase. In chapter 5 it is explained how the median volume diameter is estimated and how the results compare with the measurements from a disdrometer. Thereafter, in chapter 6, a conclusion of this master thesis will be given, followed by the bibliography and the appendix.

2

Literature Review

In this chapter, related literature to this research is reviewed and the used simulations for this research are briefly discussed. First, in section 2.1, general information about cloud radars is discussed by first briefly explaining how cloud radars work in subsection 2.1.1, then in subsection 2.1.2 explaining where cloud radars are used for and finally in subsection 2.1.3 explaining what the limitations are of using cloud radars. After this, in section 2.2 it will be discussed what research is done on using cloud radars for rain observations by first focusing on the literature about vertically profiling and then focusing on literature about slantwise profiling in subsections 2.2.1 and 2.2.2, respectively. Finally, in section 2.3, the used simulations in this research will be discussed briefly.

2.1. Cloud Radar

2.1.1. How Cloud Radar Works

This section will explain the basics of how cloud radars work. Cloud radars work very similar as weather radars. The radar emits electromagnetic radiation with a certain frequency and measures the backscatter. A part of the emitted radiation backscatters, because of the interaction with particles in the atmosphere, like precipitation particles or cloud particles. The power and phase of the emitted radiation is known and the power and phase of the backscatter is measured. For weather radars, most scatters will be inside the Rayleigh regime. An advantage of the Rayleigh regime is that the backscattering cross section is well defined and is proportional to the diameter of the particle to the sixth power as can be seen in equation 2.1 [10].

$$\sigma_b = \frac{\pi^5 |K|^2}{\lambda^4} D^6 \tag{2.1}$$

Where K is the Dielectric factor, λ is the wavelength of the radiation in m and D is the diameter of the (spherical) particle in m. For the cloud radar, the scattering is not only in the Rayleigh regime any more. Small particles will lead to Rayleigh scattering, while bigger particles will lead to Mie scattering. Mie scattering doesn't have a backscattering cross section which keeps increasing as a function of diameter, but it will oscillate as the particle diameter increases, as can be seen in Figure 2.1. This means that even when one would know the backscattering cross section without uncertainty, that one cannot tell what diameter the particles has, as there are multiple possibilities. Moreover, with the higher frequencies at the cloud radar compared to the weather radars, power measurements are influenced more by attenuation. Precipitation, but also the gasses in the atmosphere lead to attenuation, which makes it more difficult to interpret power measurements. Furthermore, in the Mie regime, the phase of the radiation shifts differently versus polarization during the backscatter, which leads to the differential backscattering phase.

2.1.2. Where are Cloud Radars Used for?

Cloud radars can be used for multiple purposes. In the U.S., the Atmospheric Radiation Measurement (ARM) user facility uses cloud radars (Ka-W SACR) to investigate for example the cloud life cycle for

climate studies [11]. The radars do not stand still, but scan the atmosphere. Recently, also second-generation radars (Ka-W SACR2) are in use and these use two frequencies and dual polarization. An example of the application of these new radars is determining the liquid water content of clouds [11]. Moreover, this dual polarization is interesting for studying non spherical hydrometeors [11]. Clothiaux et al. states that cloud radars can be used for determining the water vapor path, liquid water content, ice water content, ice water path and cloud particle number density distributions [12]. Liao and Sassen determined empirical relationships for ice water content and liquid water content in clouds [13]. They also found an empirical relationship for the ice water content of precipitating ice crystals. This research is done by using airborne data. Liao and Sassen also state that an advantage of cloud radar is that it can be used to determine cloud boundaries for multiple cloud layers. Marinou et al. combined data from a 35 GHz radar called Mira-35 and the WALES (Water Vapor Lidar Experiment in Space) instrument to classify aerosols and clouds [14]. Moreover, Lhermitte pointed out that the small size of the cloud radars relative to lower frequency radars is convenient, especially for spaceborn operations [15].

2.1.3. Limitations

Some limitations of these radars are that the radar return power is strongly weighted by the larger particles and the relationship between radar reflectively factor and particle size are much more complex for frozen particles [11]. A consequence is that the uncertainty in particle size distribution and water content is high. On the other hand, cloud radars have higher frequencies than normal S-band and X-band weather radars. Because of this, cloud radars are more sensitive to small diameter particles, as the intensity of the echo is dependent on the inverse fourth power of the wavelength when in the Rayleigh regime, as can be seen in Equation 2.1. However, the big disadvantage is that this higher frequency also leads to more attenuation, which means that the maximum range that can be observed is significantly lower during rainfall. An other limitation of cloud radars, as well as all type of radars is that they have a minimum detection range. Take for example the radar Mira-35. Mira-35 is a 35 GHz cloud radar and operates on the Polarstern research boat. It is vertically pointed and has a minimum detection height of 165 meters above sea height [16].

When the sky is clear, one might expect no echos. However, also in clear skies some echos will occur. This can for example be because of insects in the sky. Yang et al. made an automatic identification system which detects clear sky echos [17]. In order to do this, they use a millimeter-wave cloud radar in combination with a laser-ceilometer, an L-band radiosonde and an all sky camera.

2.2. Cloud Radar for Rain Observations

Cloud radar is mostly used for observing clouds. However, a cloud radar can also be used to measure precipitation. When doing this, it is important to understand how the emitted radiation interacts with the precipitating particles. How the radiation interacts strongly depends on the size of the particle. There are three scattering regimes: Rayleigh scattering, Mie scattering and optical scattering. Rayleigh scattering occurs when the particle is much smaller than the wavelength of the radiation. When using S-band or C-band for measuring precipitation, Rayleigh scattering will occur for most of the precipitation. However, for W band and Ka band of the cloud radar, a large part of the precipitation backscattering is inside the Mie scattering regime. This can also be seen when looking at the backscattering cross sections. Figure 2.1 [10] shows that the backscattering cross section is only the same as the Rayleigh scattering particles that are smaller than approximately 1 mm for the 94 GHz frequency band at a temperature of 20°C.

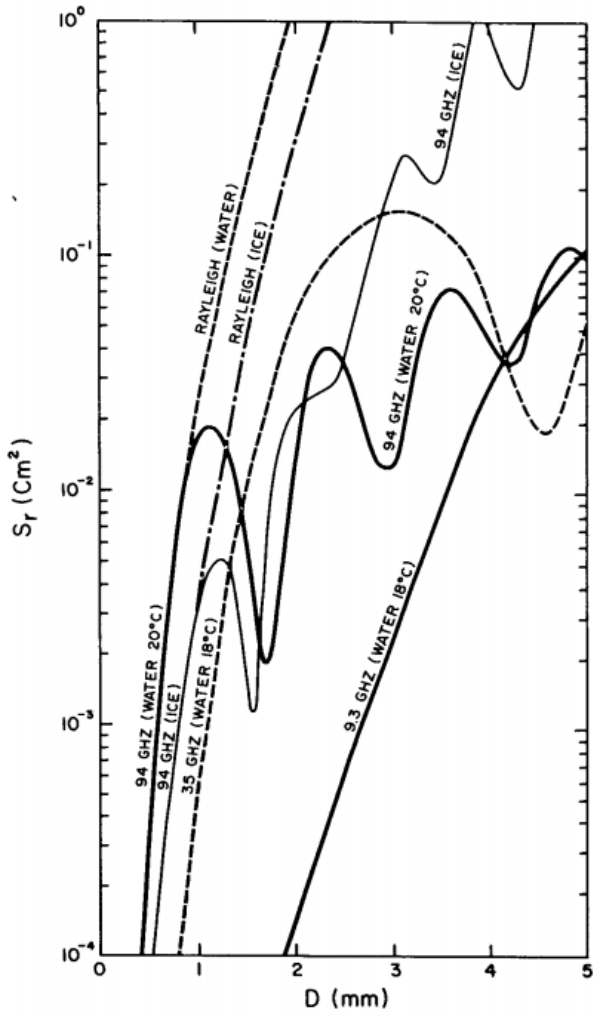

Figure 2.1: Backscattering cross sections of water and ice spheres as a function of their diameter for different radar frequency bands and water temperatures. This figure is taken from [10].

2.2.1. Vertically Profiling

Cloud radars can be used to retrieve the rainfall rate. Matrosov, for example, suggested an attenuation-based approach which could retrieve low-resolution rainfall rate profiles by using a Ka band radar which is vertically oriented [18]. Chandra et al. made an automated algorithm for determining rainfall rates with a Ka band radar [19]. They use a different retrieval method for heavy and light rain. For heavy rain, they use the amount of attenuation to determine the rainfall rate by using an $A - R$ relation, while for light rain, a $Z - R$ or an $A - R$ relationship is used, depending on the Doppler velocity.

Cloud radars can also be used to retrieve the raindrop size distribution. Kollias, for example, showed the potential of a vertically profiling 94 GHz radar for precipitation studies [20]. He retrieves the vertical air motion and the raindrop size distribution. Kollias also demonstrated this in an other article [21] and showed an example Doppler velocity graph which can be used to retrieve the vertical air motion, as can be seen in Figure 2.2 [21].

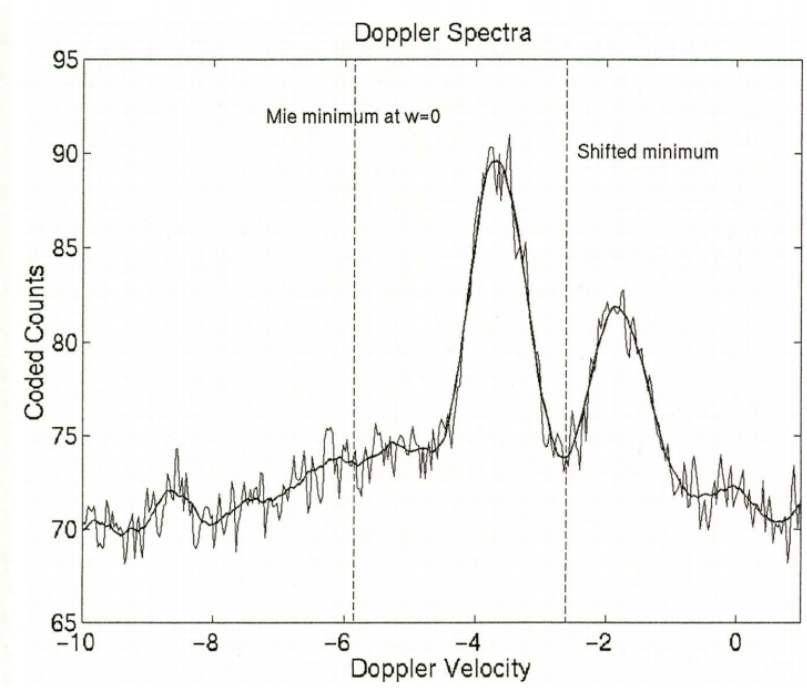

Figure 2.2: An example Doppler sample recording at 94 GHz. The shift in the Mie minimum related to the presence of the vertical wind is shown. This figure is taken from [21].

The Mie minimum is shifted and this shift can be used to estimate the vertical air motion. The estimate is simply the difference between the raindrop terminal fall velocity corresponding to the diameter, D=1.7 mm, and the first resonant minimum in the graph. In this way, the Mie scattering is used as an advantage, while it is often seen as a disadvantage compared to Rayleigh scattering, which is easier to use in terms of analytical mathematics. The big disadvantage of the 94 GHz radar is the severe problems of attenuation. Kollias states that during rainfall rates under 3 mm/h, the retrieval technique can be used from the ground up to the melting layer. At higher rainfall rates (from 10-20 mm/h), due to attenuation, the antenna will only penetrate to a height of 2 km of convective precipitation. Kollias says that together with a lower frequency radar, 94 GHz radars can overcome to a great extent the uncertainties related to the retrievals of vertical air motion and drop size distributions [21]. He also states in an other article that the high resolution measurements can be used for modeling studies of stratiform rain [22]. The latter retrieval technique of Kollias is based on the technique that Lhermitte used in his paper in 1988 [23]. Lhermitte says that his technique is applicable to measurements of downdrafts or microbursts in rainshafts and dropsize distribution in all types of rain.

Tridon uses, still at zenith-looking, beam-matched Ka and W band radar observations from the ARM program in order to disentangle Mie and attenuation effects in rain [24]. Tridon mentions that the dual wavelength ratio is commonly used in dual wavelength retrieval techniques [24]. The dual wavelength ratio is defined as in Equation 2.2.

$$\begin{aligned} \mathrm{DWR}(r) &\equiv Z_{m,\lambda_1}(r) - Z_{m,\lambda_2}(r) \\ &= \underbrace{Z_{e,\lambda_1}(r) - Z_{e,\lambda_2}(r)}_{\text{Mie effect}} + \underbrace{2\int_0^r \left(\alpha_{\lambda_2}(s) - \alpha_{\lambda_1}(s)\right) \mathrm{d}s}_{\text{Attenuation effect}} \end{aligned} \tag{2.2}$$

Tridon explains that it's difficult to distinguish the Mie effect from the attenuation effect. In order to make this distinction, the author proposes the use of Doppler spectral measurements. Small raindrops scatter in the Rayleigh regime and this small raindrop scattering corresponds to a certain Doppler velocity regime. If one can find this Doppler velocity regime for both the 35 GHz and 94 GHz band, one can calculate the part of the dual wavelength ratio that only corresponds to the attenuation of the dual wavelength ratio and not from the Mie effects, as these scatters were inside the Rayleigh plateau, thus

have not been affected by Mie effects. This technique was applied to light stratiform rain between a height of 1 and 3.2 km, but might also be suitable for higher rainfall rates or for drizzling stratocumulus, as long as the signal to noise ratio is high enough.

2 of the 3 authors of the last mentioned article continued research in 2015 and made a Ka-W band technique for simultaneous retrievals of the binned raindrop size distribution and air state parameters like vertical wind [25]. The method is applicable to rain rates that are roughly between 1 and 30 mm/h.

An other article also uses the combination of Ka and W band radar [26]. They retrieve the drop size distribution and the vertical air motion in rain. The vertical air motion is mainly determined by using the W band radar data and the raindrop size distribution is estimated by combining the data of both bands and using an iterative procedure. The results are best for rainfall rates exceeding 1 mm/h.

Matrosov also combined Ka and W band radar observation [27] from an ARM radar. He used it to retrieve the mean mass-weighted drop diameters. His method was insensitive to calibration errors, vertical air motion and attenuation effects. He derived a relation between the mean mass-weighted drop diameters and the drop size distribution from long term measurements. Matrosov states that this method is less susceptible to Doppler spectrum broadening compared to Doppler spectrum–based methods.

2.2.2. Slantwise Profiling

Almost all literature focuses on research performed with a cloud radar aimed at the zenith. Using an elevation angle smaller than 90 deg, does, however, also has advantages. Polarimetric parameters can be used in this case. For example, the differential reflectivity can be used. A small raindrop is in general spherical and the bigger the raindrop gets, the more oblate the raindrop becomes. When looking to the zenith and the raindrop falls exactly vertically, the frontal view will be a circle, even if the raindrop is oblate and this will result in the same differential reflectivity value for all different sized particles. When the elevation angle is lower than 90 deg, for example 30 or 45 deg, the frontal view will be an ellipse. In this case, the differential reflectivity will be higher if the raindrop size increases. However, the downside of a lower elevation angle is that the measured Doppler velocity component in the falling direction is lower and it is not easy to retrieve the vertical wind with this non zenith looking set-up because of the presence of the horizontal wind component.

Myagkov explained that without Mie scattering effects, the differential reflectivity is a good variable to relate to the median volume diameter (D_0) [28]. However, at W band, Mie scattering effects are present and one needs a different parameter to relate to D_0. The differential backscatter phase (δ_{co}) turns out to be an appropriate parameter at X band [29][28], because it is related to D_0 and independent on the intercept parameter (N_w).

To be able to find δ_{co}, propagation and (Mie) backscattering effects need to be disentangled. This can be done by using the Doppler spectra. Myagkov proposes a method to separate propagation and backscattering effects using the fact that small raindrops fall slower than larger raindrops in the absence of strong turbulence [28]. The idea is that the small raindrop Doppler spectra can relate to propagation effect only, while larger raindrop Doppler spectra are also affected by Mie scattering effects. The key concepts of this method are used in this thesis research.

2.3. Simulations

For the raindrop size distribution retrieval, different variables could be useful. Because there is little known about the polarimetric measurements of cloud radars, next to literature studies, simulation work is necessary. This simulation work in development is discussed in an internal report [30]. Simulation results will be used in this master thesis research, where emphasis is given to obtain an extra polarimetric variable for the cloud radar. This variable is the differential backscatter phase, δ_{co}, which shows a good potentiality for estimating D_0.

Citing [30], the numerical values of the backward (S) and forward (F) scattering amplitudes for raindrops are obtained using the Fredholm integral method. T-matrix method could be used as well. The Liebe model for the complex refractive index of water, which depends on frequency and temperature, is implemented. The temperature (T) may vary between 1 and 40 °C and the radar elevation angle can be selected from 0 to 90°. The raindrop size distribution is modeled by the gamma distribution with equi-volume spherical diameters (D) ranging from 0.1 to 8 mm. The raindrops are modeled as oblate spheroids.

3

Data, Error and Preprocessing

This chapter focuses on the data used for this research and the error analysis. First, in section 3.1 the used cloud radar is introduced, then in section 3.2 it will be explained what measurement files are obtained. After that, it will be explained why and how a table is created to select hours of interest for this research in section 3.3. In section 3.4, examples of plots of the measurements will be given and how these can be used to determine if an hour is interesting for this research or not. Then, in section 3.5 it is discussed what disdrometer will be used to compare the retrieved median volume diameter with (in section 5.4). Section 3.6 focuses on how the errors are calculated in this research. At last, in section 3.7 there will be explained how an extra calibration correction will be determined.

3.1. Used Cloud Radar

The used cloud radar in this research is a dual-frequency polarimetric cloud radar, which can be seen in Figure 3.1. It emits (and measures) two frequency bands: 35 GHz (Ka band) and 94 GHz (W band), because these frequencies have a high relative transmission in the Earth's atmosphere. Two large and two small spherical antennas are used to emit and receive the 35 and 94 GHz frequency band radiation, respectively. The radar was oriented with an elevation angle of 45 deg for all measurements that are used in this research. The advantage of this elevation angle is that one can make use at the same time of polarimetric measurements and Doppler spectra related to raindrop fall velocities. The radar is located next to a 213 m high KNMI-mast, which is used for meteorological measurements. It is convenient that also other meteorological instruments are present, because this gives the opportunity to use this as extra data or as comparison. The rainfall rate at the surface, which is used in this research, is measured by a weather station on the cloud radar.

3.2. Measurement Files

The cloud radar provides binary files which are converted into NetCDF files, which are easy to read by programming languages like for instance MATLAB. There are two NetCDF files per hour. One contains the raw measured data of this hour, while the other contains some processed data of this hour. This research mainly uses the raw data, but uses the processed data to check whether the hour is interesting by looking at the rainfall rate, the equivalent reflectivity factor and the copolar correlation coefficient. In section 3.4 it will be explained how these variables are used to check if an hour is interesting for this research. The most important variables that the (raw data) NetCDF files contain are given here with a short explanation:

- A time vector, containing all time bins of the measurements
- A range vector, containing all range bins of the measurements
- A velocity vector containing all Doppler velocity bins of the measurements
- A 3-dimensional matrix containing the Doppler spectrum at horizontal polarization at different range and time bins

- A 3-dimensional matrix containing the Doppler spectrum at vertical polarization at different range and time bins
- A 3-dimensional matrix containing the real part of the cross spectrum at different range and time bins
- A 3-dimensional matrix containing the imaginary part of the cross spectrum at different range and time bins
- A 2-dimensional matrix containing the integrated noise power at horizontal polarization at different range and time bins
- A rainfall rate vector, containing the rainfall rate at the surface corresponding to all time bins measured from a weather station next to the cloud radar

Figure 3.1: The used polarimetric dual-frequency cloud radar located at Cabauw, a small town in the Netherlands.

3.3. Rainfall Event Selection

In this research, not all hours of data that the radar collects is of interest. More specific, this research focuses on hours with rainfall (without hail or fog with it). Furthermore, there should be available data for the 35 and 94 GHz radar, the radar's elevation angle should be 45 deg, the radar's azimuth angle should be 247 deg and there must be a clear melting layer which is not extremely low. The elevation angle has changed some times from 45 deg to 30 deg and back. Since data with different elevation angles are not easily comparable and the majority of the data is with a 45 deg elevation, only data with a 45 deg elevation angle is used. During the research, the radars orientation has also changed to upside down, because some water accumulated on top of the radar and changing the orientation to upside down helped to reduce this effect. As a consequence of this, the 45 deg elevation angle is now detected as an elevation angle of 135 deg (180-45 deg).

To be able to find the hours of interest, it was convenient to write a MATLAB script that loops through all NetCDF files and also through a publicly available file from the KNMI website that contains information about the precipitation type at Cabauw as a function of time and adds this information to a table. This table contains the following information for every hour:

- The date (including the starting hour of the day)
- The elevation angle [deg]
- The azimuth angle [deg]
- The mean rainfall rate of the hour measured at the surface with a weather station [mm/h]
- The maximum rainfall rate of the hour from weather station [mm/h]
- The availability at 35 GHz [0/1]
- The availability at 94 GHz [0/1]
- Rainfall (precipitation type) [0/1]
- Snow (precipitation type) [0/1]
- Thunder (precipitation type) [0/1]
- Ice (precipitation type) [0/1]
- Fog (precipitation type) [0/1]

At the end of the MATLAB script, the table is saved as a '.mat' and '.txt' file. Moreover, it is convenient to import the text file into excel and use it as a table inside excel, as it is very easy to use filters in different columns there. As an example, the following filters are applied to find interesting hours for this research:

- Elevation angle = 45 or 135 [deg]
- Azimuth angle = 247 or 102 [deg]
- Mean rainfall rate > 0.1 [mm/h]
- Available 35 GHz = 1
- Available 94 GHz = 1
- Rainfall = 1
- Snow = 0
- Thunder = 0
- Ice = 0
- Fog = 0

Moreover, the table is sorted from high mean rainfall rates to low mean rainfall rates. This results into Table 3.1.

Table 3.1: Table created for finding hours of interest with filters applied to find interesting hours for this research.

Date + hour	Elevation	Azimuth	Mean rain	Max rain	Available 35	Available 94	Rainfall	Snow	Thunder	Ice	Fog
210406_060002	135	102	5.31	78.2	1	1	1	0	0	0	0
210121_030001	45	247	4.00	184.5	1	1	1	0	0	0	0
210203_120001	45	247	3.92	7.6	1	1	1	0	0	0	0
210406_150000	135	102	3.51	93.7	1	1	1	0	0	0	0
210121_190001	45	247	2.92	7.1	1	1	1	0	0	0	0
210203_130003	45	247	2.18	6.7	1	1	1	0	0	0	0
210203_140001	45	247	1.89	6.4	1	1	1	0	0	0	0
210203_110002	45	247	1.84	4.0	1	1	1	0	0	0	0
210121_230000	45	247	1.27	3.3	1	1	1	0	0	0	0
210121_200000	45	247	1.26	4.1	1	1	1	0	0	0	0
210203_100003	45	247	1.21	3.3	1	1	1	0	0	0	0
210429_020001	135	102	1.17	14.2	1	1	1	0	0	0	0
210121_210002	45	247	1.14	4.8	1	1	1	0	0	0	0
210327_010001	135	102	0.93	19.1	1	1	1	0	0	0	0
210203_030002	45	247	0.91	15.5	1	1	1	0	0	0	0
210121_180002	45	247	0.90	3.3	1	1	1	0	0	0	0
210406_140002	135	102	0.81	20.5	1	1	1	0	0	0	0
210121_220001	45	247	0.78	5.2	1	1	1	0	0	0	0
210126_080001	45	247	0.66	6.4	1	1	1	0	0	0	0
210406_160000	135	102	0.49	28.3	1	1	1	0	0	0	0
210406_080002	135	102	0.49	14.7	1	1	1	0	0	0	0
210429_100001	135	102	0.45	2.1	1	1	1	0	0	0	0
210203_060001	45	247	0.42	5.6	1	1	1	0	0	0	0
210430_100003	135	102	0.32	4.0	1	1	1	0	0	0	0
210406_090001	135	102	0.30	15.9	1	1	1	0	0	0	0
210406_070000	135	102	0.27	7.7	1	1	1	0	0	0	0
210406_230000	135	102	0.27	15.0	1	1	1	0	0	0	0
210121_000001	45	247	0.25	8.1	1	1	1	0	0	0	0
210201_020003	45	247	0.21	1.0	1	1	1	0	0	0	0
210411_030002	135	102	0.20	2.1	1	1	1	0	0	0	0
210126_040000	45	247	0.19	4.4	1	1	1	0	0	0	0
210201_010001	45	247	0.19	1.6	1	1	1	0	0	0	0
210122_000002	45	247	0.17	2.9	1	1	1	0	0	0	0
210429_030002	135	102	0.17	1.3	1	1	1	0	0	0	0
210412_080003	135	102	0.14	4.6	1	1	1	0	0	0	0
210430_110002	135	102	0.12	3.2	1	1	1	0	0	0	0
210408_000002	135	102	0.10	4.3	1	1	1	0	0	0	0

3.4. Plotting Cloud Radar Variables

The previous section explained that a table was made to find interesting hours. This table, however, does not tell how the rainfall rate at the surface is distributed over the hour. Moreover, it does not tell if there is a clear melting layer visible and if so, how high this is. To be able to quickly get this information, one can use the processed NetCDF files. As an example, the third of February 2021 will be used from 10 am to 11 am, which can also be found in the 11^{th} row of Table 3.1. First, the rainfall rate can be plotted versus time. This is done in Figure 3.2. As can be seen, this hour is particularly interesting, because there was a rainfall rate at the surface of more than 0.1 mm/h during almost the whole hour. Thereafter, the equivalent reflectivity factor can be plotted, like is done in Figure 3.3. One can clearly see that precipitation is falling to the surface the whole hour, as the precipitation results in a relatively high equivalent reflectivity factor and this is clearly visible close to the ground. In this research, the focus is on rainfall events and this means that one must find the heights and times where and when there is rainfall. When there is rainfall can be determined by the rainfall rate which is measured by the weather station. Until what height there is rainfall, in other words, at what height is the bottom of the melting layer, can be found by looking at the copolar correlation coefficient. The copolar correlation coefficient can also be found in the processed NetCDF file and this can be plotted versus time and height, as can be seen in Figure 3.4. One can clearly see the melting layer in these plots, as the copolar correlation coefficient is significantly lower in the melting layer than in rain and clouds. The lowest height of the bottom of the melting layer during this hour is approximately at a height of 1080 m.

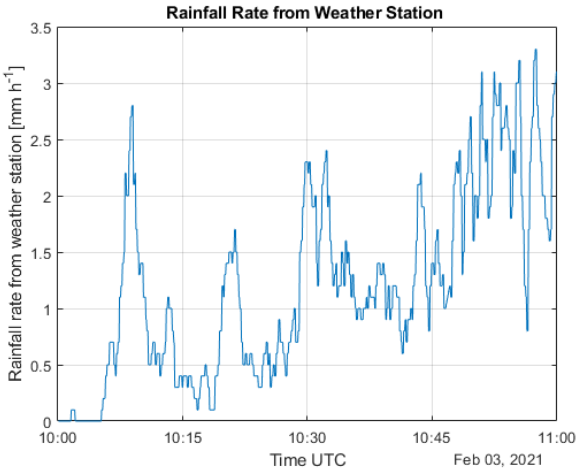

Figure 3.2: Rainfall rate at the third of February 2021 measured from a weather station at Cabauw from a (processed) NetCDF file.

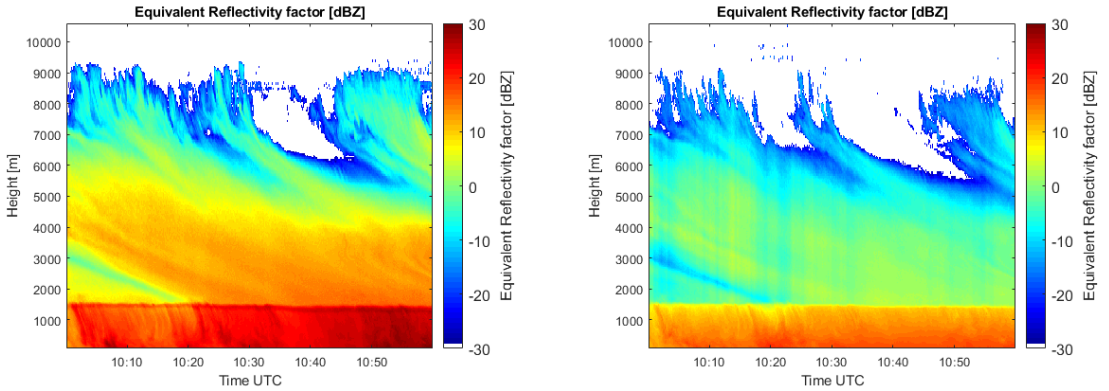

(a) 35 GHz (b) 94 GHz

Figure 3.3: Equivalent reflectivity factor at the third of February 2021 from a processed NetCDF file.

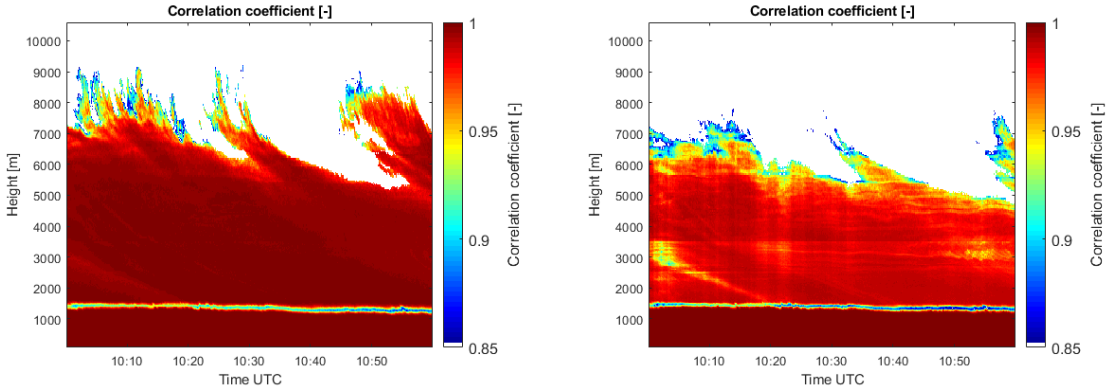

(a) 35 GHz (b) 94 GHz

Figure 3.4: Copolar correlation coefficient at the third of February 2021 from a processed NetCDF file.

3.5. Disdrometer

In section 5.4, the retrieved median volume diameter with the cloud radar will be compared to disdrometer measurements. A Particle Size and Velocity (Parsivel) optical disdrometer is used [31]. This disdrometer is located at the surface at a horizontal distance of about 150 m from the used cloud radar. Further, the cloud radar is not looking in the direction of the disdrometer. A Parsivel disdrometer transmits a laser beam and measures the received voltage of the laser beam which has propagated through air and falling raindrops. When there is a raindrop in the laser beam, the decrease in voltage can be used to estimate the equi-volume spherical diameter of the raindrop. The minimal detectable raindrop size is approximately 0.25 mm. The Parsivel disdrometrer uses 22 diameter classes when observing raindrops where the smallest used class is [0.25, 0.375] mm and the highest class is [6,7] mm. The measurements of the disdrometer are used to retrieve the mass-weighted mean diameter (D_m) and this D_m will be compared to the D_0 retrieved with the cloud radar.

3.6. Error Calculation

It is important to select a methodology for assessing the quality of results. In this research, this will , among other things, be done by using error/uncertainty calculations using statistical methods. In most one dimensional graphs in this thesis (95%) confidence intervals will be given in the form of error bars. During this thesis, confidence intervals will be calculated for differential reflectivity corrections, differential (propagation) phase corrections and for the differential backscatter phase. The next subsection will explain how confidence intervals of a mean can be calculated, which is applicable for the confidence intervals of the differential reflectivity corrections and the differential (propagation) phase corrections. The section after that will explain how the confidence interval of the difference of two dependent variables can be estimated, which is applicable for the confidence interval of the differential backscatter phase. Moreover, this section will explain why the re-sampling method bootstrapping will be used.

3.6.1. Confidence Interval of the Mean

To calculate the confidence interval of a mean when only the sample mean and sample standard deviation are known, one can assume that the sample mean follows a t-distribution and has a standard deviation of $s_x/\sqrt{n}$ if the population is normally distributed [32][33]. When there are more than 30 samples, one can also use the t-distribution when the population is not normally distributed. For the differential reflectivity corrections and differential (propagation) phase polarimetric corrections (see section 3.7), there are more than 30 samples at every height, as can be seen in Figure 3.6. This means that it is not necessary to check if these variables are normally distributed. The confidence interval can consequently be calculated in the following way:

$$CI = \bar{x} \pm t^* \cdot \frac{s_x}{\sqrt{n}} \tag{3.1}$$

where CI is the confidence interval, $\bar{x}$ is the sample mean, n is the amount of samples, t^* is a confidence multiplier that is a function of the amount of degrees of freedom (which is in this case equal to $n-1$) and the confidence level that one chooses (in this case 95%). The value of t^* can be found in a t distribution table. At last, s_x is the sample standard deviation, which can be calculated in the following way:

$$s_x = \sqrt{\frac{\sum(x_i - \bar{x})^2}{n-1}} \tag{3.2}$$

where x_i is a single sample, $\bar{x}$ is the sample mean and n is again the amount of samples. The term in Equation 3.1 starting with the $\pm$ sign is also called the margin of error.

3.6.2. Confidence Interval of the Difference of Two Dependent Variables

In the case of the differential backscatter phase, things get more complex. δ_{co} is calculated by taking the difference of two variables which are not independent, namely the differential phase and the differential propagation phase. Moreover, the differential phase is not calculated by directly estimating a mean. However, one can still make a rough estimation of the 95% confidence interval by making some assumptions. First, one can find the confidence interval of the differential propagation phase, by using

the re-sampling method bootstrapping. An advantage of bootstrapping is that one does not have to assume that the differential propagation phase is normally distributed. Moreover, it is a relatively simplistic method to get the confidence interval. The MATLAB function 'bootci' wil be used to calculate the 95% confidence interval using bootstrapping with a number of bootstrapping samples of 1000. Finally getting the confidence interval of the differential backscatter phase is not trivial. In this research, it will be assumed that the margin of error of the differential backscatter phase is about equal to the margin of error of the differential propagation phase. The underlying assumption of this is that the random error of the differential phase is much smaller than the random error of the differential propagation phase, which seems like a reasonable assumption, as the differential phase is calculated by including a lot more measurements than the differential propagation phase. Note that this assumption may lead to an underestimation of the margin of error of the differential backscatter phase.

3.7. Polarimetric Calibration Correction

While investigating the polarimetric variables, in particular the differential phase, this phase did not show the expected trend of the simulation and exhibited significant discrepancies in values comparing both frequency bands. Therefore, it became necessary to enter in contact with the senior scientist of the RPG company (manufacturer of the dual-frequency cloud radar).

A part of the provided data will need an extra calibration correction before the data can be used for research. In particular, the differential reflectivity and the differential phase. This section will explain how the corrections are made and will show plots of the corrections. In section 4.4, the impact of the calibration results will be shown by comparing plots of the spectral differential reflectivity, spectral differential phase, differential backscatter phase and specific differential phase with and without using the extra calibration corrections.

3.7.1. Principle

To be able to find a calibration correction, one must have a measurement and a reference to compare with. In practise, sometimes other calibrated instruments are used to compare with. In this case, there is another possibility proposed by Dr. A. Myagkov via mail communication. One can make use of the fact that one knows the theoretical values of the differential reflectivity and the differential phase in drizzle. The differential reflectivity is namely 1 (linear) or 0 dB and the differential phase is equal to 0 deg in drizzle. This can be explained by the fact that the raindrops are small in drizzle and in rain there is a size shape relation which tells us that small raindrops will be close to spherical. This spherical symmetry of the raindrops will lead to these theoretical differential reflectivity and the differential phase values of 1 (linear) and 0 deg, respectively. Consequently, one can assume that if one would apply a calibration correction, the resulting differential reflectivity should be 1 and the resulting differential phase should be 0 deg. Using Equation 3.3 in the case of drizzle, this will result in Equation 3.5. Likewise, using equation 3.4 in the case of drizzle will lead to Equation 3.6. In conclusion, one needs to use observations of drizzle to find a correction for z_{dr} and ϕ_{dp}.

$$z_{dr,corrected} = z_{dr,uncorrected} + z_{dr,correction} \tag{3.3}$$

$$\phi_{dp,corrected} = \phi_{dp,uncorrected} + \phi_{dp,correction} \tag{3.4}$$

$$z_{dr,correction} = 1 - z_{dr,uncorrected,drizzle} \tag{3.5}$$

$$\phi_{dp,correction} = -\phi_{dp,uncorrected,drizzle} \tag{3.6}$$

3.7.2. Drizzle File Selection

To determine these corrections, first drizzle measurements need to be chosen. The created table in section 3.3 can be used for this. There are some criteria for these drizzle measurements. First of all, the rainfall rate must be very low, otherwise, it is not drizzle. A maximum rainfall rate of 0.3 mm/h is used,

but most of the time, the rainfall rate was lower than 0.1 mm/h, which means that no rain was detected by the weather station. However, when looking at the equivalent reflectivity factor and at the copolar correlation coefficient, one can still be certain that it was raining. When the reflectivity factor is above 0 dBZ and the copolar correlation coefficient is close to 1, one can be certain that one is observing rain. The reflectivity factor namely shows that one is observing liquid or solid objects in the sky and the only objects below the melting layer that can be observed in the sky with a reflectivity factor close to 1 is rain. The base of the melting layer can easily be found with the copolar correlation coefficient, because the copolar correlation coefficient is lower in the melting layer than in rain. The copolar correlation coefficient in the melting layer is often between 0.85 and 0.95. All values mentioned in this paragraph are valid for both the 35 GHz band as the 94 GHz band. An extra check is applied to be certain that one is observing rain. A publicly available file from the KNMI website that contains information about the precipitation type at Cabauw as a function of time is used to check if there was indeed rain during these hours. This resulted into the following parts of hours that are used for the calibration correction:

- 2021 February 1st 00:00-0:52
- 2021 February 3rd 18:32-18:59
- 2021 February 3rd 19:22-19:59

The melting layer heights during these periods are estimated separately for the 35 GHz and 94 GHz frequency bands. For the 35 GHz frequency band, this leads to the heights 900 m, 950 m and 1000 m, respectively and for the 94 GHz frequency band, this leads to 940 m, 950 m and 1000 m, respectively. Note that the height of the melting layer is not a function of the frequency. The different melting layer height estimation results for both frequencies at the first used (part of) hour show that the method is not exact. Therefore, an extra 100 m margin is taken, so the measurements are certainly not from inside the melting layer.

3.7.3. Requirement in SNR

To get a reliable correction, one needs to use measurements with a good signal-to-noise ratio (SNR), however, one also needs enough used measurements for getting reliable averages. Alexander Myagkov advised to only use measurements with a signal to noise ratio of 30 dB or higher. However, this correction is especially important close to the boundaries of the first chirp, so at approximately 100 meters height and 850 meters height. At about 850 meters height, this 30 dB threshold seemed to filter out so many measurements, that I chose to change the threshold into 25 dB in order to keep enough measurements to average over. When the signal to noise ratio for the reflectivity with horizontal polarization z_{hh} or with vertical horizontal z_{vv} is larger than 25 dB, the corresponding z_{dr} and ϕ_{dp} values are saved into a vector. Then the mean z_{dr} value is taken and Equation 3.5 is used to calculate the correction of the differential reflectivity. The method explained in section 3.6 is used to get the 95% confidence interval and they are plotted as error bars.

3.7.4. Polarimetric Calibration Corrections

The resulting differential reflectivity correction can be seen in Figure 3.5(a) and (b) for 35 and 94 GHz, respectively. Moreover, the values of the calibration corrections and margins of errors can be found in in Appendix B in Table B.1. One can see that the correction for the 35 GHz is between 0.03 and 0.04 for most heights and between -0.025 and -0.1 for most heights at 94 GHz. When one looks at the error bars, which represent the 95% confidence interval, as explained in section 3.6, one can see that these drizzle measurements result in consistent calibration values. Remember that this calibration correction is based on data of two different days. It is plausible that this correction still shows a consistent correction. It is also important to check if enough samples where used to determine these correction values. The amount of samples that were used for the differential reflectivity and differential phase can be seen in Figure 3.6 for both 35 and 94 GHz. This figure shows that more observations could be used at lower altitudes than at higher altitudes, because the signal-to-noise ratio at higher altitudes was often less than 25 dB. The differential phase correction is plotted in Figure 3.5 (c) and (d) for 35 and 94 GHz, respectively. The values of these corrections show the importance of the correction. The 94

GHz band was better calibrated polarimetrically than the 35 GHz band. In this research, the differential phase is used to calculate the specific differential phase, which is the range derivative of the differential phase. The 35 GHz correction is so different per height/range, that this extra calibration correction is extremely essential to be able to use the specific differential phase. What is also notable, is that the differential phase corrections are very different at the second chirp than at the first chirp of the frequency modulated continuous wave radar. The second chirp starts at a height of 864.4 m. This means that this extra calibration is extra important at these locations. Moreover, one needs to be careful with drawing conclusions at this transitioning region between different chirps. Results of the differential reflectivity, the differential propagation phase, the specific differential phase and the differential backscatter phase with and without these calibration corrections will be compared in section 4.4.

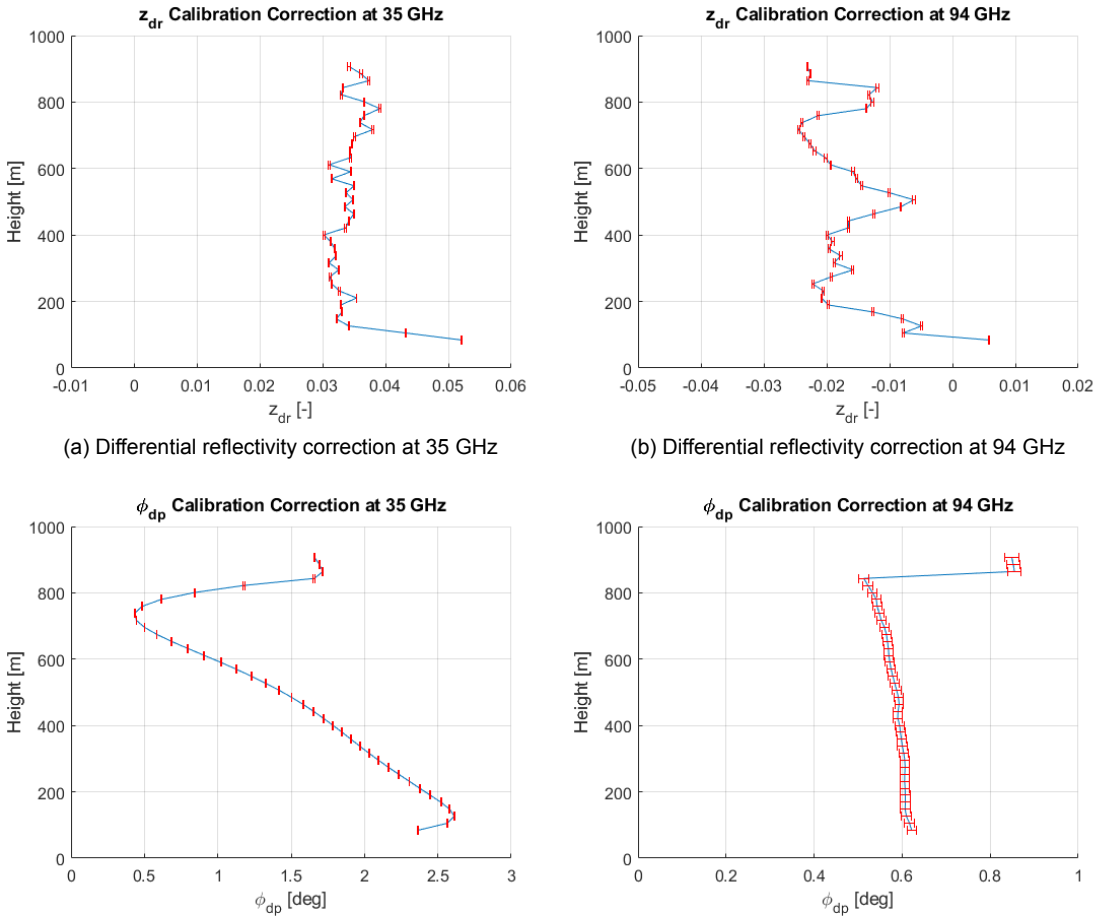

(a) Differential reflectivity correction at 35 GHz

(b) Differential reflectivity correction at 94 GHz

(c) Differential phase correction at 35 GHz

(d) Differential phase correction at 94 GHz

Figure 3.5: Differential reflectivity correction and differential phase correction at 35 GHz and 94 GHz. The error bars represent a 95% confidence interval, which are calculated as explained in section 3.6. The plotted values can also be found in Appendix B in Table B.1.

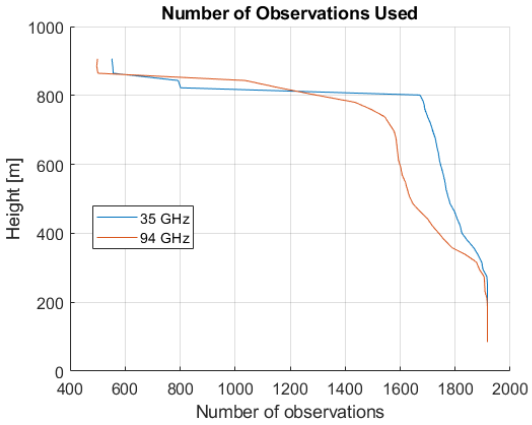

Figure 3.6: The number of observation used to calculate the correction values for the differential reflectivity (z_{dr}) and the differential phase (ϕ_{dp}) at 35 GHz (in blue) and 94 GHz (in red).

4

Estimating δ_{co} and K_{dp} after Disentangling Propagation and Backscattering

In this chapter, the focus is given to separate in the Doppler spectra, what belongs to backscattering and propagation. For this purpose, an algorithm is developed, namely the Rayleigh plateau detection algorithm. This algorithm is explained in section 4.1. This algorithm allows to make a first estimation of the differential backscatter phase (δ_{co}) as is done in section 4.2 and the specific differential phase (K_{dp}) as is done in section 4.3. In section 4.4, the impact of the polarimetric calibration on these variables will be investigated in section 4.4. At last, in section 4.5, this chapter will be summarized.

4.1. Rayleigh Plateau Detection

The specific differential phase (K_{dp}) and the differential backscatter phase (δ_{co}) are both potentially useful parameters for a raindrop size distribution retrieval. The cloud radar measures these parameters, however, not directly. The cloud radar measures the differential phase (Ψ_{dp}), which is the sum of the two-way differential propagation phase (Φ_{dp}) and the differential backscatter phase, as can be seen in Equation 4.1. The specific differential phase can be calculated from the differential propagation phase by using Equation 4.2.

$$\Psi_{dp}(r) = \Phi_{dp}(r) + \delta_{co}(r) \tag{4.1}$$

where Ψ_{dp} is the differential phase in deg, Φ_{dp} is the two-way differential propagation phase in deg and δ_{co} is the differential backscatter phase in deg.

$$K_{dp} = \frac{1}{2}\frac{d\Phi_{dp}}{dr} \approx \frac{1}{2}\frac{\Phi_{dp}(r_2) - \Phi_{dp}(r_1)}{r_2 - r_1} \tag{4.2}$$

where K_{dp} is the specific differential phase in deg/km and r is the range in km. The factor a half originates from the fact that the electromagnetic radiation travels back and forth before the radar measures the backscatter. This makes K_{dp} a one-way contribution at the range r to the differential propagation phase. To be able to disentangle the propagation and scattering effect, one can make use of the spectral differential reflectivity and spectral differential phase measurements [28]. Figure 4.1 shows an example of spectral reflectivity (sz_{hh}) measurements (a), spectral differential reflectivity (sz_{dr}) measurements (b) and spectral differential phase ($s\Psi_{dp}$) measurements (c) all at the same moment in time and at three different heights.

Small raindrops scatter in the Rayleigh regime and thus, have δ_{co} equals 0 deg. This property can help to estimate Φ_{dp} and consequently K_{dp}, because Ψ_{dp} is simply equal to Φ_{dp} when δ_{co} equals 0 deg, as can be seen in Equation 4.1. The goal is to find a Doppler velocity range, which corresponds only to scatters of small raindrops so that property holds. In that case, ψ_{dp} and then δ_{co} and K_{dp}, can

be estimated. An important insight is that the electromagnetic wave that scatters from small droplets at the range r has propagated through raindrops with all sizes in the range $[0, r-\Delta r]$, and that, depending on the radar wavelength, leads to the increase or decrease of the differential propagation phase. Φ_{dp} is thus a cumulative variable of which K_{dp} is the range derivative.

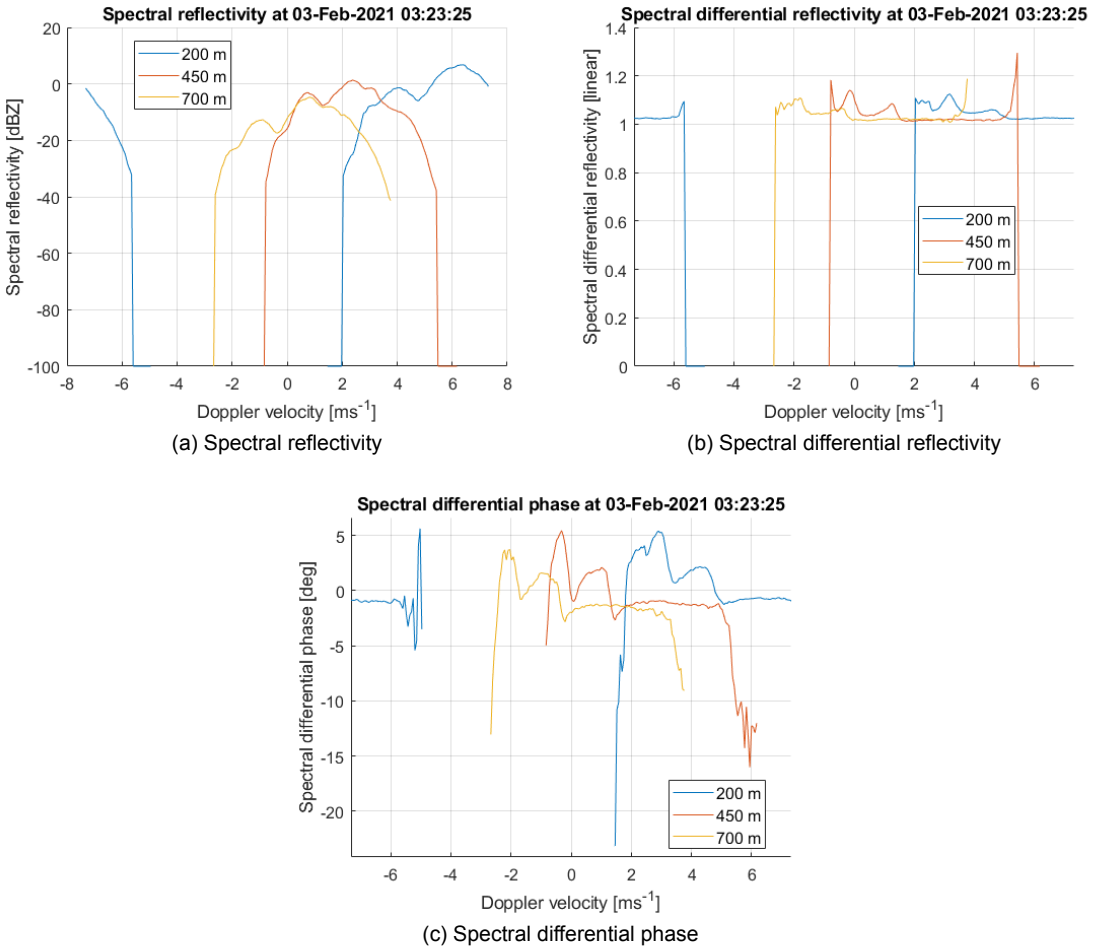

(a) Spectral reflectivity

(b) Spectral differential reflectivity

(c) Spectral differential phase

Figure 4.1: Spectral measurements from a 94 GHz cloud radar at Cabauw at heights 200 m, 450 m and 700 m on the third of February 2021 at 03:23:25.

At this moment, one needs to find this Doppler velocity range. The terminal velocity of small raindrops is in general smaller than the terminal velocity of bigger raindrops, if there is no strong turbulence [28]. In practise, however, wind and aliasing complicates the situation, and this property will not be sufficient to find the Doppler velocity range. Fortunately, more properties can be used to find the Doppler velocity range. The first property is that the spectral differential reflectivity is close to 1 (or 0 dB) for spherical raindrops. Small raindrops are in general very close to spherical and in general bigger raindrops are more oblate spheroids [34]. Moreover, the spectral differential reflectivity will be relatively constant during this Doppler velocity range relative to the rest of the Doppler spectrum of the differential reflectivity. The spectral differential phase is also relatively constant during this Doppler velocity range. Because of this relatively constant behaviour of the scattering of the small raindrops and the fact that this part of the Doppler spectrum is inside the Rayleigh regime, this Doppler velocity range will be referred to as the Rayleigh plateau.

By eye, the approximate Rayleigh plateau can be found reasonably easy. In Figure 4.1 for example, the Rayleigh plateau at 450 m (the red line) is approximately from 1.9 m/s until 4.8 m/s. There are, however, a lot of measurements done per hour of data, so an automated detection algorithm is

required. The rest of this section explains step-wise and in detail how this automated detection algorithm works and how one can validate if the results are desirable. These steps are also visualized in Figure 4.2. Keep in mind that during this research, in order to get consistent and reliable results, only rain is studied with a rainfall rate above 0.1 mm/h.

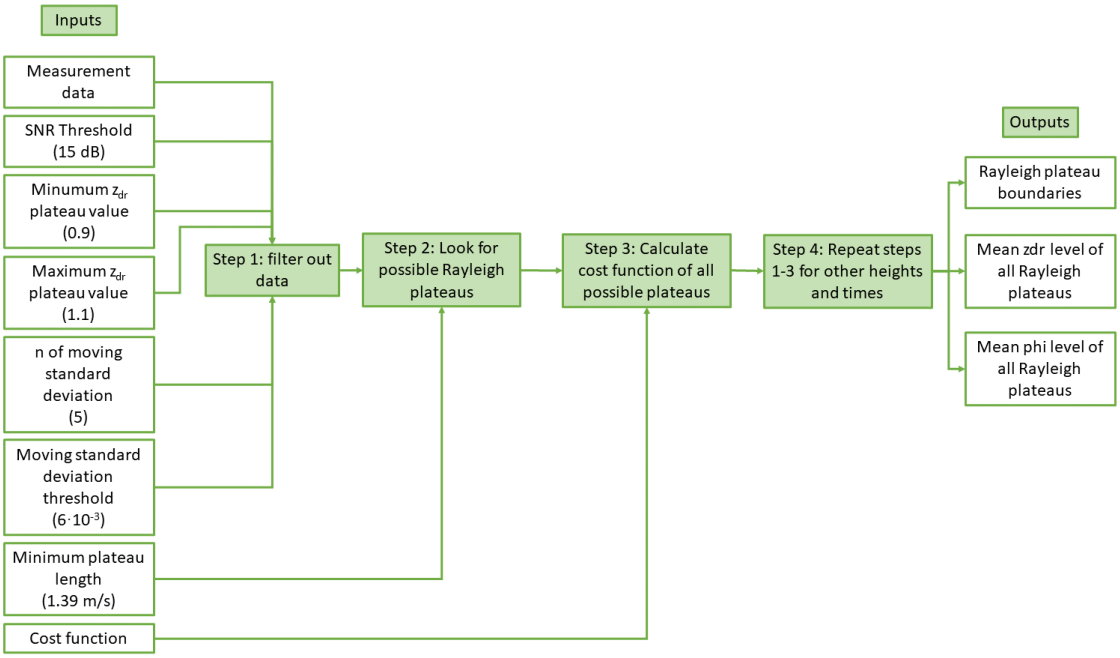

Figure 4.2: Diagram showing the inputs, the 4 steps and the output of the Rayleigh plateau detection algorithm.

4.1.1. Step 1: Filtering out Data

At one moment in time and one height, one has the spectral differential reflectivity and the spectral differential phase, like for example in Figure 4.1. As some parts are noisy, parts with signal to noise ratios below 15 dB are filtered out (turned into NaN values). To find the Rayleigh plateau, first, more data is filtered out which is clearly not inside the Rayleigh plateau. A spectral differential reflectivity value of about 1 (linear) is expected at the Rayleigh plateau, as small raindrops are about spherical and because of this values above 1.1 and below 0.9 are filtered out. This implies a correct polarimetric calibration.

Moreover, as the Rayleigh plateau is relatively constant, the moving standard deviation of the spectral differential reflectivity as a function of Doppler velocity should be low at the Rayleigh plateau. When determining the moving standard deviation, one must note that aliasing is taking place. This means that it is also possible that the Rayleigh plateau is for example starting at -15 m/s, goes to the left, is then aliased, thus jumps from -19.74 m/s to +19.74 m/s and then continues to the left until +15 m/s. 19.74 m/s is hereby the Nyquist Doppler velocity (at 35 GHz). To also consider possible Rayleigh plateaus that are aliased, a trick is applied before calculating the moving standard deviation. This trick is visualized in Figure 4.3. A copy of the second half of the data is placed in front of the first half of the data and a copy of the first half of the data is placed after the second half of the data. In this case, data refers to a spectral differential reflectivity vector. This vector contains the spectral differential reflectivity values that correspond to Doppler velocities that can be found in a Doppler velocity vector. The idea of this trick is that this new vector, with twice the length as the original data, can be processed and in the end, the copied parts of the vector will be removed again. The first part of this processing is calculating the moving standard deviation of the spectral differential reflectivity. For calculating this moving standard deviation, a k value of 5 is used, which means that the local standard deviation is cal-

culated by considering the current value, the 2 values before the current value and the 2 values after the current value. Now, Doppler velocities where the moving standard deviation with $k = 5$ is higher than $6 \cdot 10^{-3}$ are filtered out to remove the Doppler velocities that are not inside the Rayleigh plateau, because the spectral differential reflectivity is not constant enough there. All chosen numbers, like the spectral differential reflectivity thresholds of 0.9 and 1.1 and the moving standard deviation threshold of $6 \cdot 10^{-3}$ with $k = 5$, are chosen empirically, which means that different numbers are tried until the result seemed to be optimal.

Figure 4.3: Aliasing trick. A copy of the second half of the data is placed in front of the first half of the data and a copy of the first half of the data is placed after the second half of the data.

4.1.2. Step 2: Look for Possible Rayleigh Plateaus

At this moment, a vector is obtained with values of the moving standard deviation of the spectral differential reflectivity and NaN values in it, because a part was already filtered out. The corresponding Doppler velocities are also known. In principle, the Rayleigh plateau can be the corresponding Doppler velocities of any adjacent series of non-NaN values in this obtained vector. An estimation of the Rayleigh plateau Doppler velocities can be found by looking at all possible Rayleigh plateaus and by calculating a cost function for all these possibilities. The possible Rayleigh plateau with the highest value of the cost function is then an estimation of the Rayleigh plateau. There are, however, still some challenges to overcome. Firstly, the amount of possible Rayleigh plateaus can be extremely high, as will be demonstrated later, so first some more possibilities need to be filtered out. Secondly, this cost function still needs to be defined.

To demonstrate the large amount of possibilities that might still be present, a simple example will be used. Assume that the standard deviation vector has 70 adjacent non-NaN values and all other values are NaN values. How many possibilities will there be in this case? Let's first determine the amount of possibilities with short series of adjacent non-NaN values to be able to formulate a general formula that's also applicable in the case of 70 adjacent non-NaN values. As can be seen in Figure 4.4, 2 adjacent non-NaN values lead to 1 possibility, 3 adjacent non-NaN values lead to 1+2=3 possibilities and 3 adjacent non-NaN values lead to 1+2+3=6 possibilities. One can conclude that the amount of possible series with a length of at least 2 can be calculated like in Equation 4.3.

$$m = \frac{n(n-1)}{2} \tag{4.3}$$

where m is the amount of adjacent series with a minimum length of 2 and n is the amount of adjacent non-NaN values. This corresponds to the binomial coefficient that is shown in Equation 4.4, where 2 items are selected from a collection of n items such that the order of selection does not matter. This means that in the case of 70 adjacent non-NaN values, there are $m = 70 * (70-1)/2 = 2415$ possibilities. These are still a lot of possibilities, keeping in mind that the cost function needs to be calculated for all these possibilities and this will only result in the Rayleigh plateau in one moment in time at one height. To reduce the amount of possibilities, possibilities with a Rayleigh plateau length smaller than 10 values, which is a Doppler velocity spectrum width of 1.54 m/s for the 35 GHz band and 0.57 m/s for the 94 GHz band, are filtered out. At this moment, the script can still be slow and because of this, more possibilities must be filtered out. All possibilities are filtered out that do not start at the first non-NaN value and do not end at the last non-NaN value. An example of this is shown in Figure 4.5. In this example, only 1 value is filtered out, but when n gets bigger than 4, a lot of values will be filtered out because of this. This improves the speed drastically, but will exclude Rayleigh plateau possibilities that might be good estimates of the Rayleigh plateau. However, the Rayleigh plateau detection algorithm still gives good results.

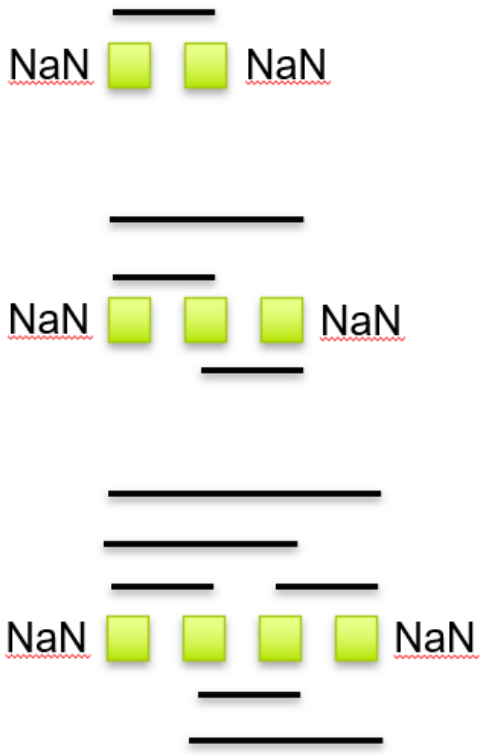

Figure 4.4: An example of the amount of possible adjacent series when there are 2,3 or 4 adjacent non-NaN values. The green squares represent the non-NaN values and the black lines represent the possible series (with a length of 2 or more).

$$\binom{n}{2} = \frac{n!}{2!(n-2)!} \tag{4.4}$$

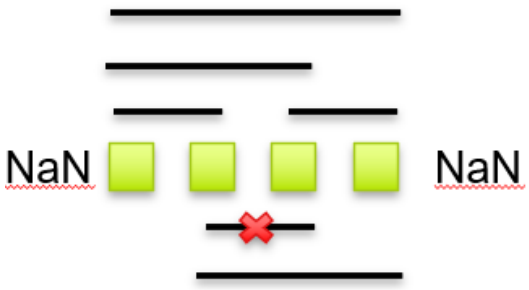

Figure 4.5: An example of the amount of possible adjacent series when there are 4 adjacent non-NaN values. The green squares represent the non-NaN values and the black lines represent the possible series (with a length of 2 or more). The red cross represents the value that is filtered out because it does not start at the first value and does not end at the last value.

4.1.3. Step 3: Calculate Cost Function of all Possible Plateaus

At this moment, there are often still lots of possible plateaus. To find the best estimate of the Rayleigh plateau, an own made cost function is used. The cost function is given in Equation 4.5.

$$CF = \frac{l}{l_{max}} - 0.5\frac{sz_{dr,std}}{sz_{dr,std,max}} - 0.5\frac{s\phi_{dp,std}}{s\phi_{dp,std,max}} \tag{4.5}$$

where CF stands for cost function, where a higher value means a better Rayleigh plateau candidate. l stands for the length of the plateau in m/s and l_{max} is the highest l value of all possibilities in m/s. A broader plateau is generally better, as this will lead to a more reliable average of the spectral differential

reflectivity and spectral differential phase and because of this, the first term has a positive sign. $z_{dr,std}$ is the standard deviation of all the spectral differential reflectivity values inside the Rayleigh plateau possibility [linear] and $z_{dr,std,max}$ is the highest $z_{dr,std}$ value of all possibilities (linear). The lower the standard deviation, the better the candidate is, because the Rayleigh plateau is relatively constant and therefore, this second term has a negative sign. $\phi_{dp,std}$ is the standard deviation of all the spectral differential phase values inside the Rayleigh plateau possibility in deg and $\phi_{dp,std,max}$ is the highest $\phi_{dp,std}$ value of all possibilities in deg. As this third term is very similar to the second term, again the following holds, the lower the standard deviation, the better the candidate is, because the Rayleigh plateau is relatively constant and therefore, also the third term has a negative sign. The constants before the three different terms can be tuned so the performance of the algorithm works best. The +1, -0.5 and -0.5 seem to give good results.

As mentioned before, the Rayleigh plateau possibility with the highest cost function is the resulting estimate of the Rayleigh plateau. Now the Rayleigh plateau Doppler velocity range is known, useful information can be used for the estimation of δ_{co} and K_{dp}, namely the mean spectral differential reflectivity, the Rayleigh plateau width and the mean spectral differential phase of the Rayleigh plateau, the latter being the differential propagation phase, ϕ_{dp}.

4.1.4. Step 4: Repeat Steps 1-3 for other Heights and Times

Step 1-3 explain how to find the Rayleigh plateau Doppler velocity range at one moment in time and at one height using one frequency band. The cloud radar at Cabauw meausures 993 times per hour and has 344 range bins. For this research, however, only the range bins below the melting layer are used, which are typically 30-40 range bins during January, February and March. The cloud radar is a dual band radar, so this method can be applied for both frequency bands. This means that for one hour of study data, steps 1-3 needs to be applied for approximately $993 \cdot 35 \cdot 2 = 69,510$ times. Note that, these 69,510 computations can in principle be done simultaneously, because the computations are independent of each other. At the moment, for loops are used to do steps 1-3 for all height bins and time bins. In MATLAB, the parfor function could be used in the future, to increase the computation speed. This, however, requires changes to the script and starting and closing a parpool also takes a considerable amount of time. An other possibility to improve the computation speed would be to vectorize the whole script, although this might result in memory issues. Table 4.1 shows an example of the computation time of the Rayleigh plateau detection algorithm. As can be seen, the 94 GHz band takes considerably more time than the 35 GHz. The reason for this is the higher spectral resolution of the 94 GHz, as this higher resolution leads to more possible plateaus that will be found and it takes more time, because the cost function needs to be calculated for more possible plateaus.

Table 4.1: Table showing an example of the computation time of the Rayleigh plateau detection algorithm.

Date	3-feb-21
Hour	10:00-11:00
Rainfall rate above threshold of 0.5 mm/h (% of time)	73%
Laptop processor	Intel i7 8th Gen
Laptop RAM Memory	16 GB
Laptop cores	6
Computation time for 35 GHz	28 seconds
Computation time for 94 GHz	69 seconds

4.1.5. Check Performance

At this stage, the automatic Rayleigh plateau detection algorithm is complete and working, but there is not yet a good way way to verify if the performance is good. To be able to do this, it's good to create plots and check if the found Rayleigh plateau corresponds to the Rayleigh plateau that one would find by eye. As only one hour of data can already lead to 69,510 Rayleigh plateaus, checking all Rayleigh plateaus is simply not an option. Therefore, I made a small script that creates plots of the spectral reflectivity, spectral differential reflectivity and spectral differential phase, together with the found Rayleigh plateau Doppler velocity boundaries at one moment in time at all height bins and puts these plots in three videos, one for every type of spectral measurement. The results are three videos with for example 35 frames

that are all shown for 1.67 seconds. The time needs to be chosen and every height bin leads to a frame in the video. There is one video for the spectral reflectivity, one video for the spectral differential reflectivity and at last, one video for the spectral differential phase. In this way, one can quickly check the quality of the detection algorithm. This is also useful when one finds unexpected results and one want to check if the detection algorithm is not the cause of this. Figure 4.6 shows an example of a spectral reflectivity frame (a), a spectral differential reflectivity frame (b) and a spectral differential phase frame (c) for the 35 GHz band. One can see that the detected Rayleigh plateau looks relatively constant for the spectral differential reflectivity and the spectral differential phase, as the Rayleigh plateau should be. Moreover, the spectral differential reflectivity is close to 1 (linear), as expected for the Rayleigh plateau.

Figure 4.7 shows the same example as Figure 4.6, but now for the 94 GHz band. Figure 4.7 (a) is a good example where one can see a side lobe that is caused by Mie scattering. One can see that the detection algorithm finds a Rayleigh plateau which does not include this side lobe. This is exactly what one would expect, as Mie scattering should not be present inside the Rayleigh regime. Figure 4.7 (b) shows that the spectral differential reflectivity is almost constant at the Rayleigh plateau. Figure 4.7 (c) shows that the spectral differential phase is varying more at the Rayleigh plateau than the spectral differential reflectivity does.

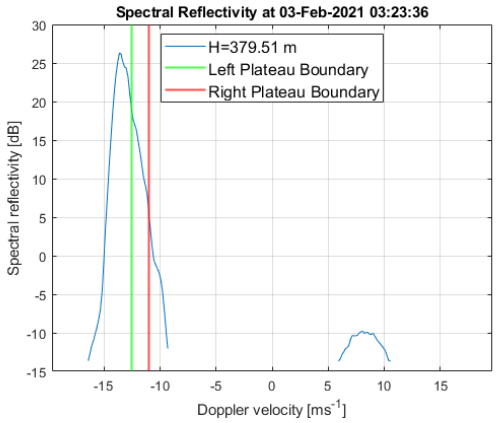

(a) Spectral reflectivity (sz_{hh})

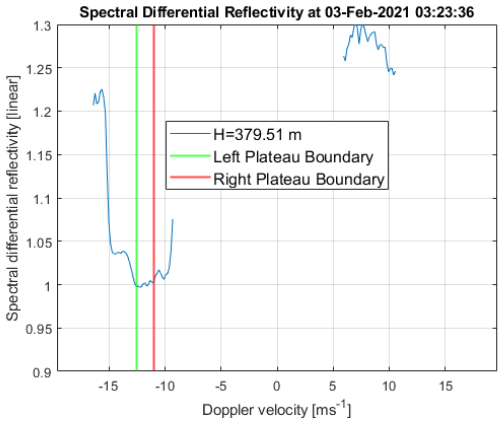

(b) Spectral differential reflectivity

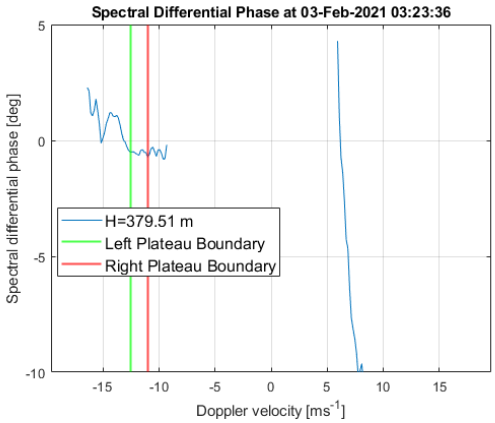

(c) Spectral differential phase

Figure 4.6: Spectral measurements from a 35 GHz cloud radar at Cabauw at a height of 379.51 m on the third of February 2021 at 03:23:36. The boundaries of the detected Rayleigh plateau are also shown. An extra polarimetric calibration correction was applied.

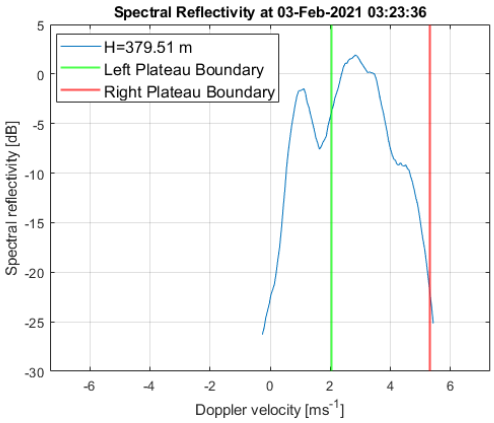

(a) Spectral reflectivity (z_{hh})

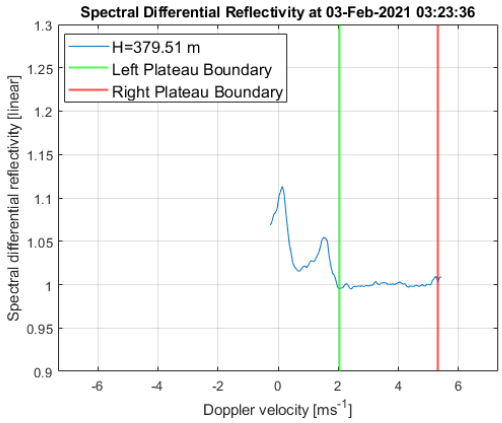

(b) Spectral differential reflectivity

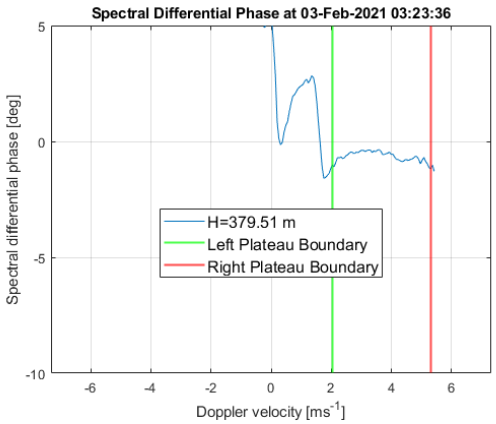

(c) Spectral differential phase

Figure 4.7: Spectral measurements from a 94 GHz cloud radar at Cabauw at a height of 379.51 m on the third of February 2021 at 03:23:36. The boundaries of the detected Rayleigh plateau are also shown. An extra polarimetric calibration correction was applied.

Some examples of Rayleigh plateau detection have been shown in section 4.1. To be able to check the performance of the Rayleigh plateau detection algorithm for more heights, a table has been made for both the 35 GHz band, Table 4.2, and the 94 GHz band, Table 4.3, including the most important details of the detected plateaus. The Doppler width is defined as the difference in Doppler velocities between the left and right Rayleigh plateau boundary. As can bee seen in Table 4.2, at 379.5 m, 400.6 m and 421.7 m, the Doppler width is equal to 1.54 m/s. This is equal to the minimum Doppler width threshold of 10 indices for the 35 GHz band. When lowering this threshold to 9 indices, which is equal to 1.39 m/s for the 35 GHz, the Doppler width from the 379.5 m changes to 1.39 m/s and the Doppler width at 400.6 m and 421.7 m stay at 1.54 m/s. This illustrates that this threshold prevents that the detected Rayleigh plateau gets too small. The downside is, however, that sometimes no Rayleigh plateau can be detected, because the only possible plateaus left after step 1 of the Rayleigh plateau detection algorithm have a length that is lower than in this case 1.54 m/s. This is what happens at 695.8 m. Only after lowering the minimum Doppler width threshold at least all the way down to 6 indices, there is found a Rayleigh plateau. This solution is shown in Figure 4.8. The Rayleigh plateau found seems to be to narrow. More specific, the right boundary should be shifted to the right to about -12.7 m/s, which is the location where the spectral differential reflectivity starts with a sudden increase. One can see that the plateau was difficult to find for the algorithm because of the unusually high spread in the spectral differential reflectivity at the Rayleigh plateau. Moreover, the spectral reflectivity shows an unusual shape. One can see two small side lobes at a Doppler velocity of about -14.3 m/s and at -12.9 m/s. Side lobes can be caused by Mie scattering effects. However, this should not be present inside the Rayleigh plateau, as this plateau is in the Rayleigh scattering regime. This unusual shape

in the spectral reflectivity, however, does not lead to a different detection, as it is not used, excepted for the SNR threshold. In conclusion, the detection algorithm works well in most cases, but can have difficulties to find a plateau when the spectral differential reflectivity versus Doppler velocity is atypical. Nonetheless, these atypical cases should be discarded for a first estimation of δ_{co} and K_{dp}.

The detected Rayleigh plateau Doppler velocity width of the 94 GHz band is in this case a bit broader than for the 35 GHz band, as can be seen when comparing Table 4.2 and Table 4.3. This is what one would expect, as the spectral resolution is higher for the 94 GHz band and this makes it possible to find a Rayleigh plateau boundary that is closer to the 'real' Rayleigh plateau boundary. However, with the spectral resolution of the 35 GHz band and the 94 GHz band that are 0.15 m/s and 0.06 m/s, respectively, one cannot explain that the Doppler width is so much broader at 94 GHz than at 35 GHz when comparing Table 4.2 and Table 4.3. When also looking at other times than the time used in the given tables, this mentioned change in Doppler width between the 35 GHz and 94 GHz frequency bands seemed to be coincidental.

The third column of the shown tables show the mean spectral differential reflectivity of the detected Rayleigh plateaus. For both the 35 GHz and 94 GHz band, one can clearly see a descending trend over height. This is probably due to differential attenuation.

The fourth column of the tables show the mean spectral differential phase shift of the detected Rayleigh plateaus. One can clearly see an increasing trend in the mean spectral differential phase shift over height for the 35 GHz band and a decreasing trend for the 94 GHz band. This is due to the differential propagation phase. This will be discussed in more detail in section 4.3.

The fifth column shows the standard deviation of the spectral differential reflectivity of the detected Rayleigh plateaus. This column is especially interesting, because a (maximum) threshold of $6 \cdot 10^{-3}$ is used for the detection method. This threshold was chosen empirically and one can see that this $6 \cdot 10^{-3}$ is only a bit bigger than some of the numbers in the fifth columns of Table 4.2 and Table 4.3, but only 1 time, no detection could be found because of this threshold, which is at 695.8 m at the 35 GHz band. Moreover, this number is used in the cost function, because a lower standard deviation means a flatter plateau and a flat Rayleigh plateau is what one would expect theoretically.

The sixth and last column shows the standard deviation of the spectral differential phase shift of the detected Rayleigh plateaus. This number is used in the cost function, because also this standard deviation is expected to be low for the Rayleigh plateau.

4.1.6. Summary of Rayleigh Plateau Detection Method

To be able to estimate two potentially useful parameters for retrieving the raindrop size distribution, the specific differential phase and the differential backscatter phase, one has to disentangle propagation and scattering effects. To do this, one has to find a part of the spectral domain that only scatters in the Rayleigh regime, because this part of the spectral domain is not influenced by Mie scattering. Without Mie scattering, the propagation effects are isolated and the propagation parameter the specific differential phase can be calculated. The differential backscatter phase can consequently be calculated, because the propagation effect is now disentangled from the scattering effects and the sum of the propagation and scattering effects is measured. The part of the spectral domain that only scatters in the Rayleigh regime is referred to as the Rayleigh plateau in this research. It is detected by an own made algorithm which uses 4 steps. In step 1, parts of the spectral domain are filtered out that have properties that do not match with the Rayleigh plateau. In step 2, the plateaus that are still possible are gathered. In step 3, a cost function is used to find the one plateau with the properties that look the most like what one would expect for the Rayleigh plateau. Finally, in step 4, one repeats steps 1-3 for other heights and other moments in time. The results seem to be good in general, however, sometimes no plateau can be detected, as the shape of the spectral differential reflectivity is not always exactly as one would expect. After detecting the Rayleigh plateaus, one can estimate the differential backscatter phase and the specific differential phase, which is demonstrated in section 4.2 and section 4.3, respectively. The differential backscatter phase will finally help to estimate the median volume diameter, as will be shown in chapter 5.

Table 4.2: Rayleigh plateau detections from a calibration corrected 35 GHz cloud radar at Cabauw on the third of February 2021 at 03:23:36.

Height [m]	Doppler Width [m/s]	mean(szdr)	mean(sphidp) [deg]	std(szdr)	std(sphidp) [deg]
84.3	2.31	1.011	-0.79	0.0018	0.10
105.4	2.78	1.008	-0.74	0.0020	0.08
126.5	2.62	1.007	-0.75	0.0017	0.13
147.6	2.62	1.009	-0.76	0.0016	0.11
168.7	2.47	1.005	-0.76	0.0013	0.07
189.8	2.62	1.006	-0.77	0.0020	0.10
210.8	2.62	1.006	-0.80	0.0025	0.09
231.9	2.00	1.004	-0.80	0.0012	0.12
253.0	2.47	1.002	-0.74	0.0012	0.13
274.1	2.47	1.004	-0.76	0.0027	0.11
295.2	2.31	1.005	-0.76	0.0015	0.11
316.3	2.31	1.005	-0.66	0.0028	0.09
337.3	2.47	1.002	-0.71	0.0035	0.13
358.4	2.47	1.001	-0.68	0.0044	0.12
379.5	1.54	1.000	-0.53	0.0026	0.09
400.6	1.54	0.995	-0.56	0.0019	0.10
421.7	1.54	0.995	-0.54	0.0012	0.07
442.8	1.70	0.996	-0.45	0.0010	0.05
463.8	1.70	0.991	-0.47	0.0016	0.12
484.9	2.00	0.991	-0.45	0.0022	0.11
506.0	2.31	0.994	-0.40	0.0024	0.12
527.1	2.47	0.991	-0.45	0.0028	0.15
548.2	2.16	0.990	-0.34	0.0017	0.12
569.3	1.85	0.990	-0.36	0.0019	0.13
590.3	1.85	0.991	-0.30	0.0029	0.08
611.4	2.16	0.982	-0.23	0.0023	0.09
632.5	2.16	0.986	-0.34	0.0019	0.08
653.6	2.47	0.987	-0.47	0.0038	0.13
674.7	2.31	0.984	-0.40	0.0044	0.09
695.8	NaN	NaN	NaN	NaN	NaN
716.8	2.31	0.987	-0.47	0.0037	0.15
737.9	2.16	0.983	-0.47	0.0040	0.14
759.0	2.16	0.982	-0.50	0.0049	0.15
780.1	2.16	0.984	-0.43	0.0019	0.15
801.2	2.47	0.982	-0.47	0.0026	0.20
822.3	2.62	0.979	-0.39	0.0027	0.18
843.4	2.47	0.977	-0.25	0.0017	0.18

Table 4.3: Rayleigh plateau detections from a calibration corrected 94 GHz cloud radar at Cabauw on the third of February 2021 at 03:23:36.

Height [m]	Doppler Width [m/s]	mean(szdr)	mean(sphidp) [deg]	std(szdr)	std(sphidp) [deg]
84.3	3.21	1.010	-0.08	0.0020	0.13
105.4	3.62	1.009	-0.16	0.0025	0.15
126.5	3.56	1.005	-0.18	0.0020	0.14
147.6	3.96	1.006	-0.19	0.0023	0.16
168.7	3.56	1.001	-0.25	0.0018	0.12
189.8	3.50	1.004	-0.37	0.0018	0.19
210.8	3.44	1.004	-0.38	0.0015	0.16
231.9	3.73	1.008	-0.41	0.0020	0.16
253.0	3.16	1.004	-0.43	0.0015	0.15
274.1	3.90	1.004	-0.43	0.0021	0.15
295.2	3.50	1.007	-0.49	0.0019	0.18
316.3	3.21	1.003	-0.51	0.0018	0.17
337.3	3.16	1.000	-0.54	0.0018	0.17
358.4	3.44	1.002	-0.61	0.0022	0.19
379.5	3.27	1.000	-0.65	0.0027	0.21
400.6	3.21	1.001	-0.66	0.0021	0.20
421.7	2.76	1.002	-0.67	0.0018	0.21
442.8	3.10	1.000	-0.67	0.0022	0.20
463.8	3.33	1.000	-0.71	0.0021	0.20
484.9	3.21	1.001	-0.78	0.0024	0.22
506.0	3.04	1.000	-0.80	0.0025	0.21
527.1	3.04	0.998	-0.82	0.0021	0.20
548.2	3.04	0.996	-0.88	0.0030	0.21
569.3	3.39	0.997	-0.89	0.0024	0.18
590.3	2.98	0.998	-0.90	0.0025	0.18
611.4	2.87	0.998	-0.91	0.0024	0.20
632.5	3.21	0.997	-1.00	0.0027	0.21
653.6	2.81	0.996	-0.98	0.0022	0.19
674.7	2.58	0.995	-0.91	0.0019	0.16
695.8	2.87	0.995	-0.94	0.0026	0.19
716.8	2.53	0.997	-0.96	0.0025	0.15
737.9	2.87	0.995	-0.98	0.0026	0.13
759.0	2.81	1.000	-1.02	0.0032	0.19
780.1	2.47	0.998	-0.96	0.0025	0.19
801.2	2.30	0.995	-0.96	0.0024	0.17
822.3	2.35	0.998	-0.98	0.0027	0.15
843.4	2.53	0.994	-1.00	0.0028	0.15

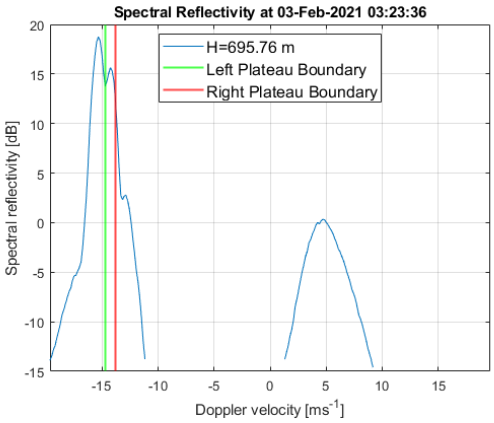

(a) Spectral reflectivity (z_{hh})

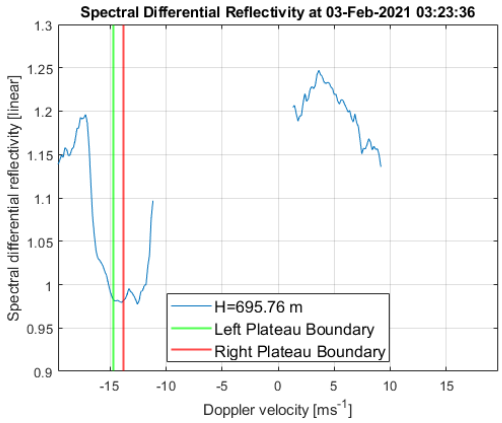

(b) Spectral differential reflectivity

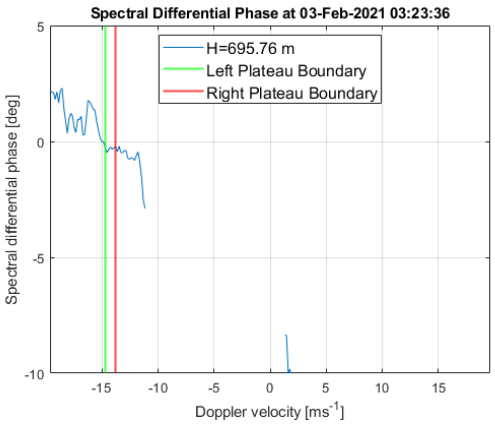

(c) Spectral differential phase

Figure 4.8: Spectral measurements from a 35 GHz cloud radar at Cabauw at a height of 695.8 m on the third of February 2021 at 03:23:36. The boundaries of the detected Rayleigh plateau are also shown. The minimum Doppler width threshold in the detection algorithm is lowered to 6 in order to get a (narrow) solution for the Rayleigh plateau. An extra polarimetric calibration correction was applied.

4.2. Estimating the Differential Backscatter Phase

The differential backscatter phase can be calculated easily, because the Rayleigh plateaus are already detected. The spectral differential phase at the Rayleigh plateau is only a consequence of propagation effects, because the differential backscattering phase is equal to 0 deg there, as the raindrops are small and thus spherical at the Rayleigh plateau. Although the backscattering is in the Rayleigh regime at the range bin r, the propagation term (forward scattering) accounts for all the sizes of raindrops (whole raindrop size distribution) present in the range bins before r. The differential propagation phase can consequently be calculated like in the following equation:

$$\Phi_{dp}(r) = \frac{1}{n_D} \sum_{1}^{n_D} s\Phi_{dp}(r, v) \tag{4.6}$$

where n_D is the number of Doppler bins in the Rayleigh plateau. Note that this equation is simply calculating the average spectral differential phase value at the Rayleigh plateau. When considering the full Doppler spectrum, one can calculate the differential phase (Ψ_{dp}) in deg at one moment in time with the following equation:

$$\Psi_{dp}(r) = \arctan\left(\frac{\sum_{v=v_{min}}^{v_{max}} -\Im(VH_{Spec}(r, v))}{\sum_{v=v_{min}}^{v_{max}} \Re(VH_{Spec}(r, v))}\right) \tag{4.7}$$

where $VH_{Spec(r,v)}$ is the cross spectrum (the conjugate of the Doppler spectrum at horizontal polarization multiplied by the Doppler spectrum at vertical polarization). The summations are over the whole Doppler range. Note that there is a weighting by the modulus of VH_{Spec} in the summation, which is a standard procedure for the moment calculations from Doppler spectra. The differential backscatter phase can subsequently be calculated by using Equation 4.1.

where $\Psi_{dp}(r)$ is the differential phase in deg, $\Phi_{dp}(r)$ is the two-way differential propagation phase in deg and $\delta_{co}(r)$ is the differential backscatter phase in deg. The calibration correction for the differential phase will be applied for both $\Psi_{dp}(r)$ and $\Phi_{dp}(r)$ and because of this, $\delta_{co}(r)$ will not be affected by the calibration correction, as these two equal corrections cancel each other out. This is a strong property of the differential backscatter phase, as the calibration of a frequency modulated continuous wave radar is not easy and brings uncertainties with it. The uncertainty of the differential backscatter phase can be estimated by using the uncertainty estimates of the differential propagation phase and the differential phase. The uncertainty of the differential propagation phase is estimated by calculating the standard deviation of the differential propagation phase at the Rayleigh plateau. The uncertainty of the differential phase is, however, more difficult to estimate. Because of physical processes, one does not expect this to be constant over all Doppler velocities. Calculating the standard deviation is therefore not a good way to estimate the uncertainty of the measurement, as one is not looking at variation because of only noise, but also because of physical phenomena, such as Mie oscillations. To be able to still get an estimate of the uncertainty of the differential phase and consequently, obtaining the uncertainty of the differential backscatter phase, the following hypothesis is suggested: the uncertainty of the differential phase is much smaller than the uncertainty of the differential propagation phase. The margin of error of the differential backscatter phase is in this case equal to the margin of error of the differential propagation phase. This was discussed in more detail in subsection 3.6.2.

An example of a differential backscatter phase profile is given in Figure 4.9 together with the corresponding differential phase and differential propagation phase profiles. One can see that the differential backscatter phase is varying a bit over height, which could be because of changes in the raindrop size distribution, but could also be because of the noise in the measurements. Further, the differential propagation phase shows a slight increase versus height at 35 GHz and a slight decrease at 94 GHz, which is in accordance with simulations (Figure 4.13).

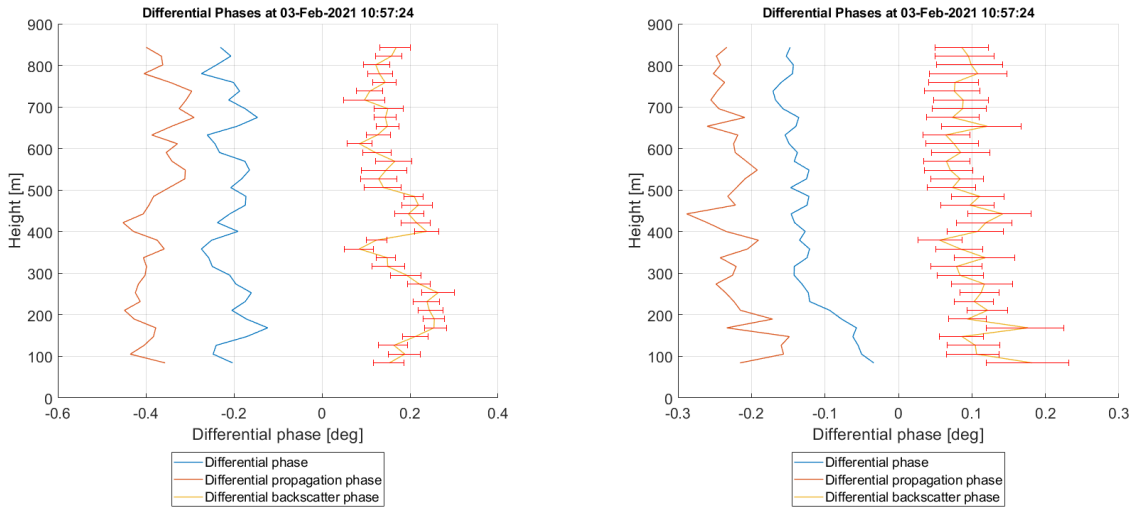

(a) Differential phases at 35 GHz

(b) Differential phases at 94 GHz

Figure 4.9: Differential phase, differential propagation phase and differential backscatter phase with applied polarimetric calibration at 35 GHz and 94 GHz on the third of February 2021 at 10:57:24. The error bars represent a 95% confidence interval, which are estimated as explained in section 3.6

A two-dimensional example of the resulting differential backscatter phase is given in Figure 4.10. One can see that there are some white parts inside the plot. This is because the differential backscatter phase is only calculated when the rainfall rate was above 0.1 mm/h. When comparing Figure 4.10 (a) and (b), so both used frequency bands, one can see that both plots show a similar shape, both relatively high values between 10:50 and 11:00 compared to the rest of the hour. When looking at the rainfall rate during this hour again in Figure 3.2, one can see that these last 10 minutes have a higher rainfall rate. If the rainfall rate increased, because the median volume diameter D_0 increased in the raindrop size distribution, then this observed increasing differential backscatter is expected. Notable is that the 35 GHz also shows values below 0 deg, which is not expected to be possible by simulations (Figure 4.11). This could be a result of the uncertainty of the estimation. Moreover, the lowest 100 m seem to give odd results, for the 35 GHz there are most of the negative differential backscatter phase values and for the 94 GHz there seem to be higher differential backscatter phase values than just above this. A possible reason for this could be that the far-field approximation for polarimetric measurements or the polarimetric calibration is not valid at these heights. For the raindrop size distribution retrieval, only heights above 150 m will be considered.

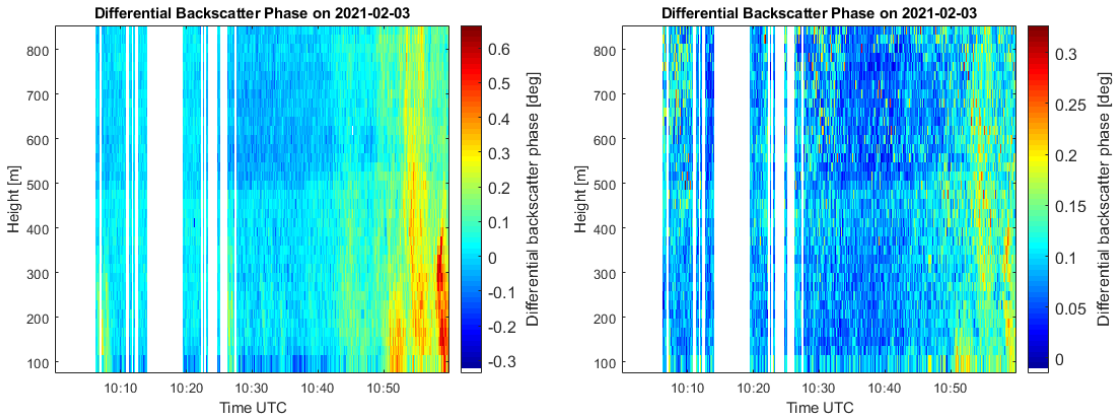

(a) Differential backscatter phase at 35 GHz (b) Differential backscatter phase at 94 GHz

Figure 4.10: Differential backscatter phase with an extra calibration correction applied at 35 GHz and 94 GHz on the third of February 2021 from 10:00 to 11:00.

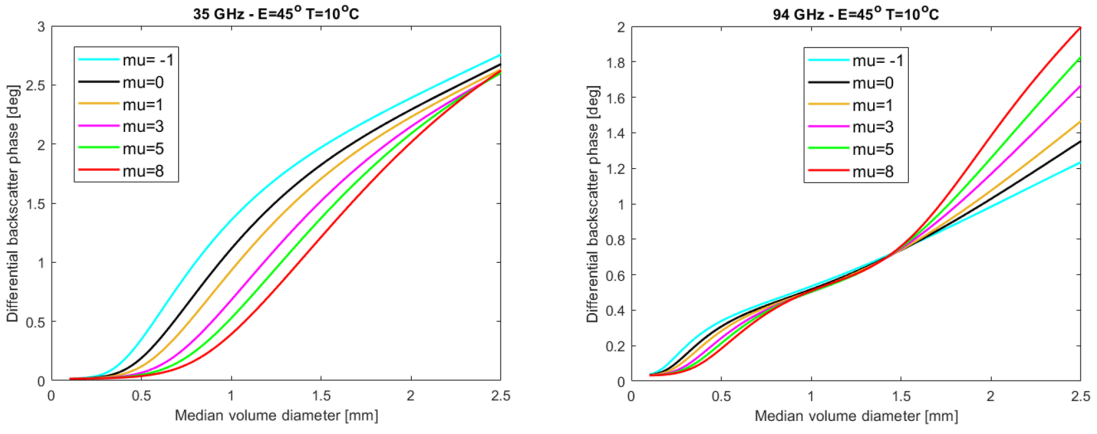

(a) 35 GHz (b) 94 GHz

Figure 4.11: Simulated differential backscatter phase as a function of the the median volume diameter (D_0) for different values of the shape parameter (μ) for the 35 GHz and 94 GHz band. The simulations were provided by C.M.H. Unal [30].

4.3. Estimating the Specific Differential Phase

Just like with the differential backscatter phase, the most difficult part has already been done in the Rayleigh plateau detection algorithm in section 4.1 to calculate the specific differential phase. This algorithm already gives the differential propagation phase. The specific differential phase can be calculated from this by applying Equation 4.2. The derivative in this equation is approximated by dividing the difference in differential propagation phase between two range bins by the difference in range between two range bins. This will result in a specific differential phase value between between two consecutive range bins. The resulting profiles for the 35 GHz and 94 GHz can be seen in Figure 4.12.

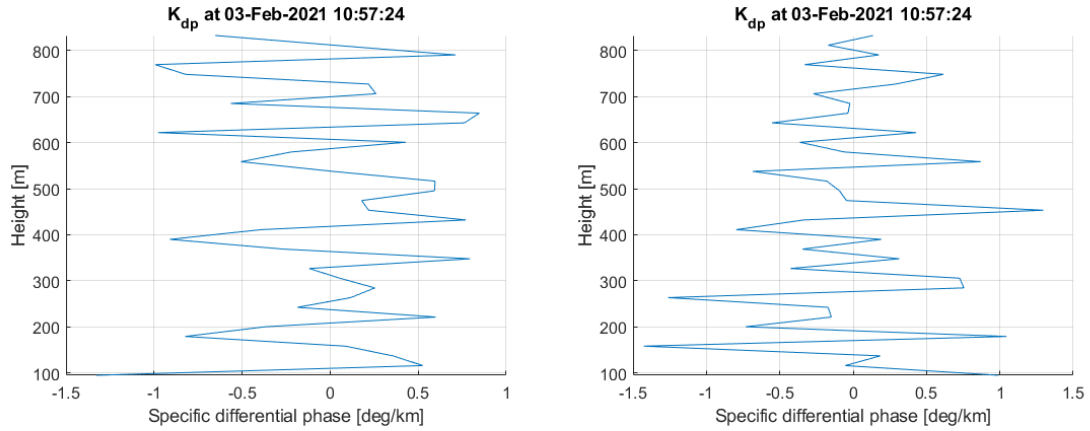

(a) Specific differential phase at 35 GHz

(b) Specific differential phase at 94 GHz

Figure 4.12: Specific differential phase with an extra calibration correction applied at 35 GHz and 94 GHz on the third of February 2021 at 10:57:24.

Unfortunately, it looks like noise is dominating the specific differential phase, because there is a lot of variation in the specific differential phase over height, while this is not expected in the signal, as the raindrop size distribution is usually fairly constant over height. This means that the noise level of the specific differential phase is probably too high and therefore, the specific differential phase cannot be used for a raindrop size distribution retrieval, or at least not directly. Possibly, smoothing the differential propagation phase over height and/or over time would help to reduce the noise level. Because of the noise, it is difficult to say what the real specific differential phase is. However, it seems like the average of these profiles are close to 0 deg/km, which means that the specific differential phase might also not be sensitive enough for small values of D_0. To check if K_{dp} can indeed be close to 0 mm/km during a rainfall event, one can look at a simulation plot for K_{dp} in Figure 4.13. One can indeed see that the 1-way specific differential phase is close to 0 deg/km at 35 and 94 GHz when D_0 is smaller than 0.7 deg. This means that specific differential phase will only be useful for rain drop size distribution retrievals when D_0 (and N_w) are sufficiently large. In this research, the focus was given to find D_0 with δ_{co} and K_{dp} was not used for the rain drop size distribution retrieval.

4.4. Polarimetric Calibration Results

This section will look back at the extra polarimetric calibration corrections that are explained in section 3.7. This time, one can compare the results of the following variables with and without this extra calibration correction applied: Spectral differential reflectivity, spectral differential phase, differential backscatter phase, differential propagation phase and specific differential phase.

4.4.1. Spectral Differential Reflectivity and Spectral Differential Phase

The Rayleigh plateaus have been detected in section 4.1. To check the performance of these detections, plots were made of the spectral reflectivity, spectral differential reflectivity and spectral differential phase. The same spectral differential reflectivity and spectral differential phase plots are shown in Fig-

ure 4.14 and Figure 4.15, but this time, the same results are also shown when one decides not to apply the extra calibration correction.

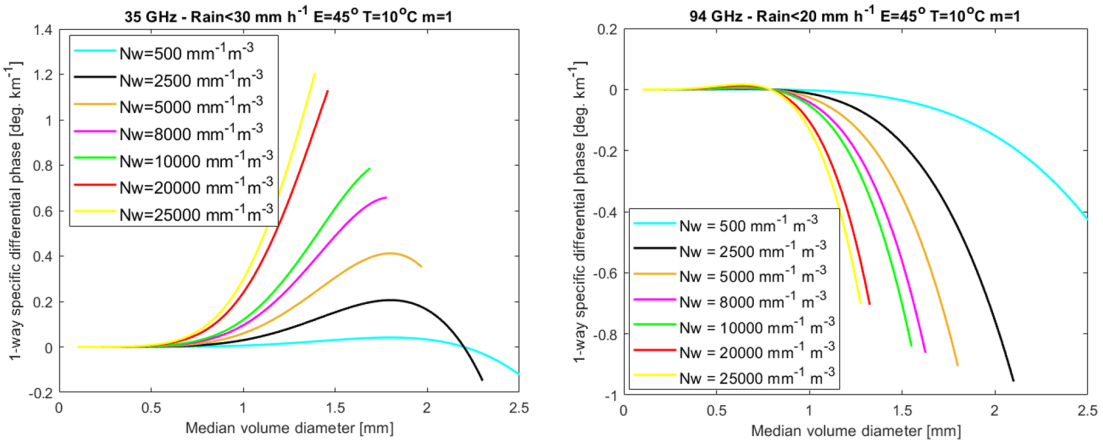

(a) 35 GHz (b) 94 GHz

Figure 4.13: Simulated specific differential phase as a function of the the median volume diameter (D_0) for different values of the intercept parameter (N_w) with the shape parameter (μ) equal to 1, the temperature equal to 10°C, the elevation angle equal to 45 deg and the rainfall rate lower than 30 mm/h for the 35 GHz band and the rainfall rate lower than 20 mm/h for the 94 GHz band. The simulations were provided by C.M.H. Unal [30].

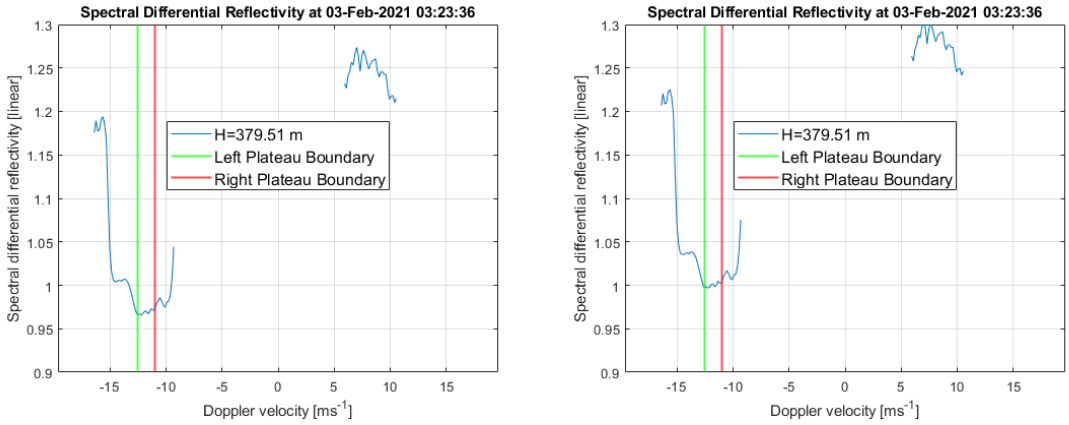

(a) Uncorrected spectral differential reflectivity at 35 GHz (b) Corrected spectral differential reflectivity at 35 GHz

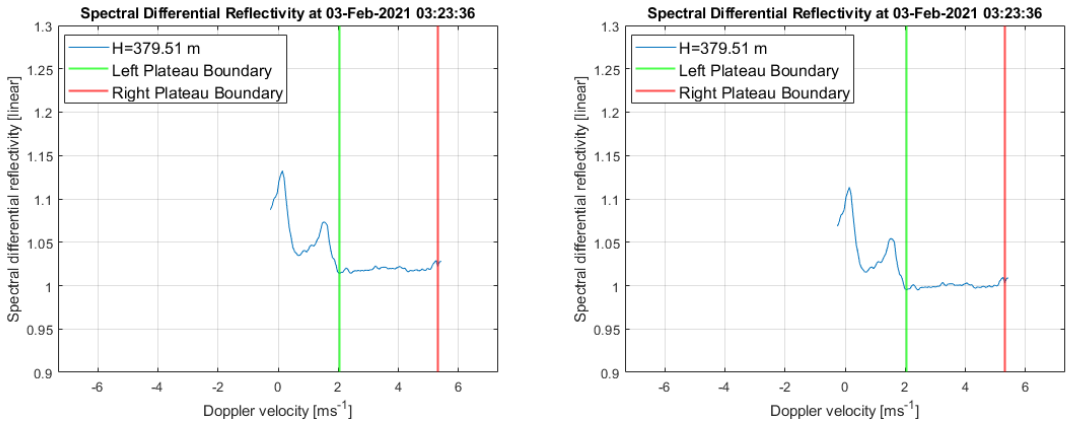

(c) Uncorrected spectral differential reflectivity at 94 GHz (d) Corrected spectral differential reflectivity at 94 GHz

Figure 4.14: Spectral differential reflectivity from a 35 GHz and 94 GHz cloud radar at Cabauw at a height of 379.51 m on the third of February 2021 at 03:23:36. The boundaries of the detected Rayleigh plateau are also shown.

When comparing Figure 4.14 (a) and (b), and Figure 4.14 (c) and (d), it is interesting that the Rayleigh plateau boundaries are not influenced by the corrections. The extra calibration corrections are the same for all Doppler velocities and because the Rayleigh plateau detection method is mostly based on the (moving) standard deviation, which are not influenced if one adds the same correction value to the spectral differential reflectivity and spectral differential phase at all Doppler velocities. Note that it is possible that a different plateau is detected by the detection method, as for example spectral differential reflectivity values below 0.9 (linear) and above 1.1 (linear) are filtered out (not considered as a possibility of the Rayleigh plateau). What is also notable, is that the average spectral differential reflectivity at the Rayleigh plateau clearly gets closer to the value 1 (linear). The value 1 (linear) is the expected value for the Rayleigh plateau when there would be no differential attenuation. Given the fact that the rainfall rate is quite high, namely 15 mm/h, one might expect some differential attenuation effect to be visible. Differential attenuation is, however, a propagation effect and Figure 4.14 shows the plots for a height of just 379.5 m, which explains why no clear differential attenuation is visible at both the 35 GHz and 94 GHz.

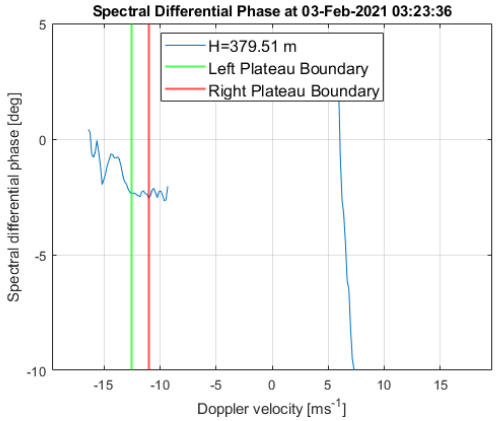

(a) Uncorrected spectral differential phase at 35 GHz

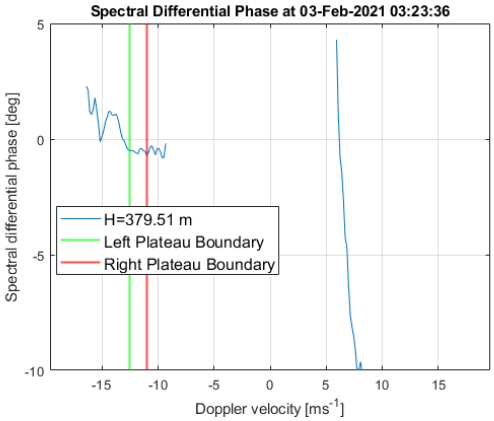

(b) Corrected spectral differential phase at 35 GHz

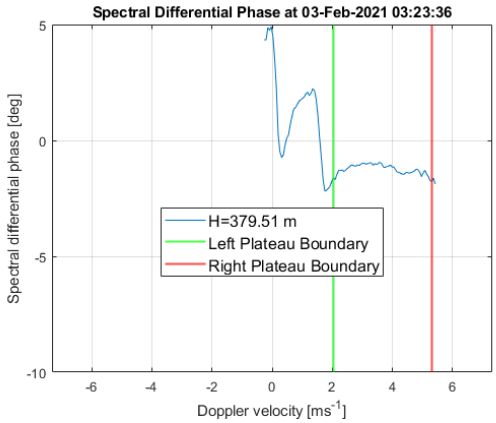

(c) Uncorrected spectral differential phase at 94 GHz

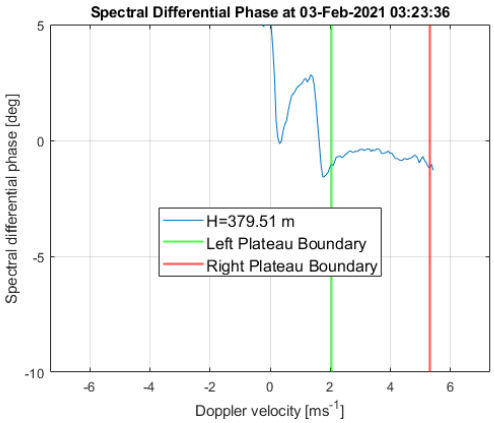

(d) Corrected spectral differential phase at 94 GHz

Figure 4.15: Spectral differential phase from a 35 GHz and 94 GHz cloud radar at Cabauw at a height of 379.51 m on the third of February 2021 at 03:23:36. The boundaries of the detected Rayleigh plateau are also shown.

Comparing Figure 4.15 (a) and (b) and Figure 4.15 (c) and (d), one can see that the Rayleigh plateau boundaries are of course again the same with and without the extra corrections, as these plots correspond to the same Rayleigh plateau detections as Figure 4.14. The average value of the spectral differential phase at the Rayleigh plateau gets closer to the value 0 deg because of the extra calibration correction. The value of 0 deg is expected if there are only spherical and thus small raindrops in the Rayleigh plateau at low heights before propagation effect shows off. As the rainfall rate is equal to 15 mm/h, it is not unexpected that there are also bigger raindrops which lead to a deviation to the value

of 0 deg.

4.4.2. Differential Backscatter Phase

Because the same differential phase correction is added to the differential phase and the differential propagation phase and the differential backscatter phase is the difference between the differential phase and the differential propagation phase, these corrections cancel each other out. This would mean that the differential backscatter phase is independent on the calibration correction. This is, however, not entirely true, as the calibration correction can in principle also lead to different Rayleigh plateau detection boundaries. In practise, however, this turns out to be hardly ever the case. The differential backscatter phase is really almost independent of the extra calibration correction. This is pleasant, as this means that the extra applied calibration correction will not add extra uncertainty to the differential backscatter phase.

4.4.3. Specific Differential Phase and Differential Propagation Phase

When comparing Figure 4.16 (a) and (b), one can see that the influence of the calibration correction is very large. Especially at the very bottom of the first chirp (first range bins) and the top of the first chirp (last range bins) of the frequency modulated continuous wave radar, the influence is very large. The correction seems to do a good job, as these unexpected extreme values of the specific differential phase are not present any more with the correction. In Figure 4.16 (c) and (d), one can see that correction did not have a large influence on the specific differential phase. This is because the differential phase correction was about the same for all height bins at the first chirp. The correction, unfortunately, does not solve the fact that the specific differential phase is noisy.

It is also interesting to plot the differential propagation phase for the calibration corrected and uncorrected data as a function of height and time. The result can be seen in Figure 4.17. It is clearly visible in Figure 4.17 (a) and (b) that the extra applied calibration correction has a large influence on the differential propagation phase at 35 GHz. One can clearly see that plot (b) is much more uniform over height, which means that the specific differential phase will be closer to 0. In Figure 4.17 (c) and (d), one can see that the calibration correction has a smaller influence than at 35 GHz. Because the extra calibration correction is about the same for every height, the shape of Figure 4.17 (c) and (d) are very similar. The specific differential phase can be seen in Figure 4.18. The extra calibration correction changes the specific differential phase a lot at the 35 GHz band, while the 94 GHz almost does not change. One can also see that the specific differential phase still has extreme values of for example -4 [deg/km], which are not expected when looking at simulations. This indicates the high uncertainty and more processing needs to be done if one wishes to use the specific differential phase.

4.5. Summary

This goal of this chapter was to estimate the differential backscatter phase and the specific differential phase. To achieve this, first, the Doppler bins must be found that only correspond to propagation effects and not to backscatter effects. These consecutive Doppler bins are called the Rayleigh Plateau. The Rayleigh Plateau is found by using an algorithm that first filters out Doppler bins that are certainly not in the Rayleigh plateau, then the best remaining plateau option is determined by comparing the remaining plateau options by using a cost function. This procedure is being executed for all combinations of height and time bins. Now the Rayleigh Plateau is found, the differential propagation phase can be calculated and this makes it also possible to calculate the differential backscatter phase by applying Equation 4.1. Moreover, the specific differential phase can be calculated by using Equation 4.2. The differential backscatter phase seems to give realistic results at the height bins above 150 m. The first estimation of the specific differential phase turns out to be too noisy to use for a raindrop size distribution retrieval. The differential backscatter phase turns out to be almost fully independent on the applied polarimetric calibration correction, which is a strong property, since no extra error will be introduced by the polarimetric calibration correction. The specific differential phase is, however, is highly dependent on the polarimetric calibration correction.

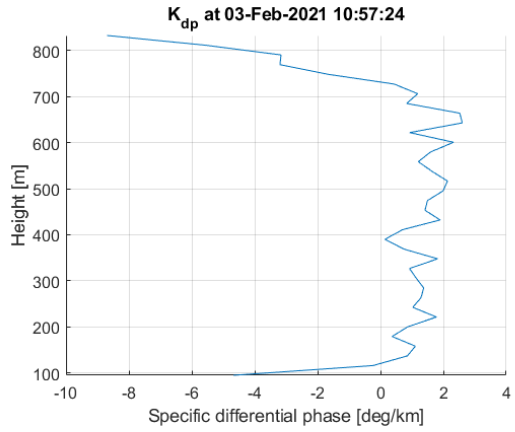

(a) Specific differential phase at 35 GHz without correction

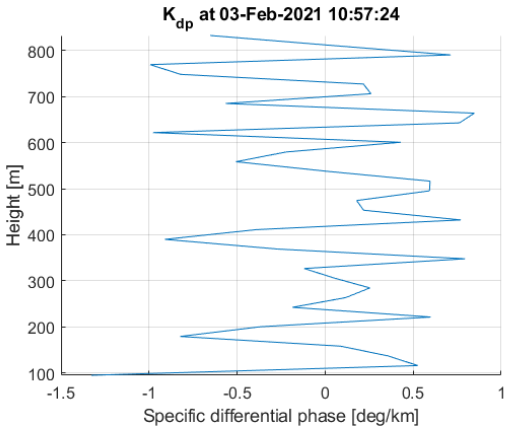

(b) Specific differential phase at 35 GHz with correction

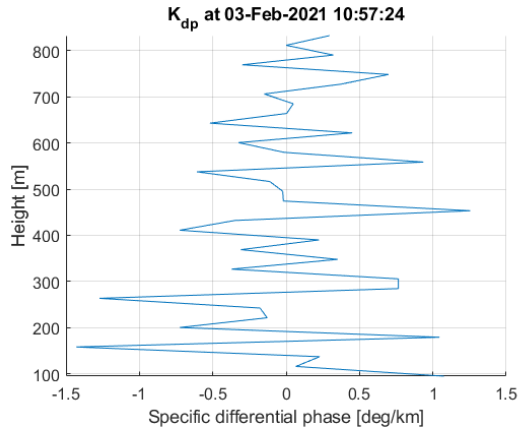

(c) Specific differential phase at 94 GHz without correction

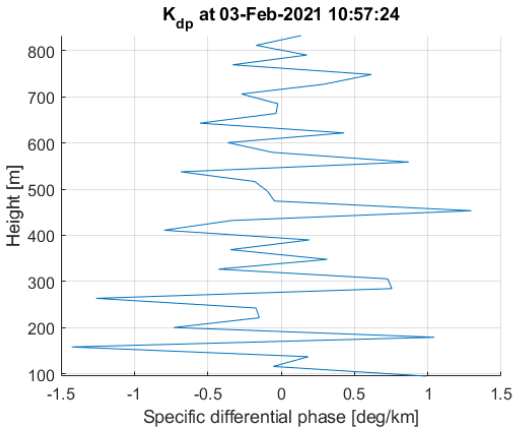

(d) Specific differential phase at 94 GHz with correction

Figure 4.16: Specific differential phase with and without an extra polarimetric calibration correction applied at 35 GHz and 94 GHz on the third of February 2021 at 10:57:24.

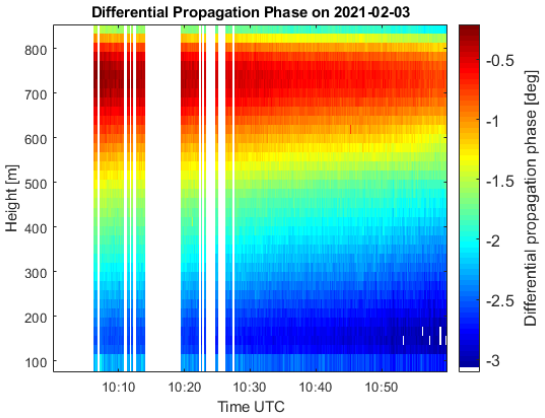

(a) Differential propagation phase at 35 GHz without correction

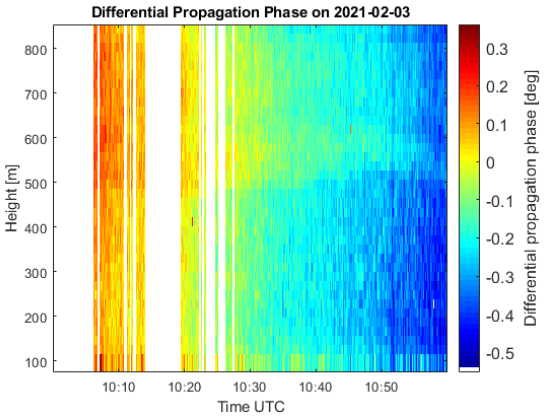

(b) Differential propagation phase at 35 GHz with correction

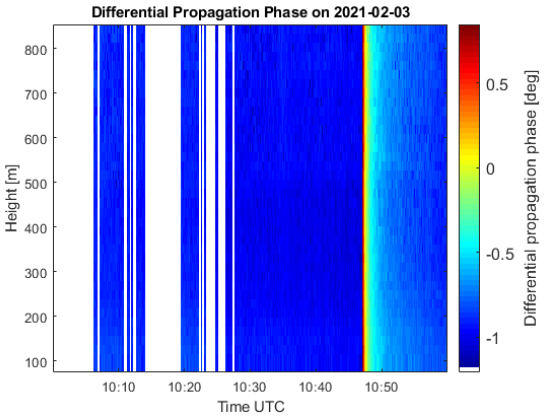

(c) Differential propagation phase at 94 GHz without correction

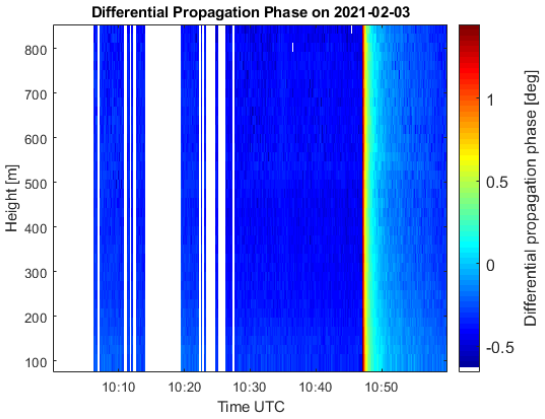

(d) Differential propagation phase at 94 GHz with correction

Figure 4.17: Differential propagation phase with and without an extra applied polarimetric calibration correction at 35 GHz and 94 GHz on the third of February 2021 from 10:00 to 11:00.

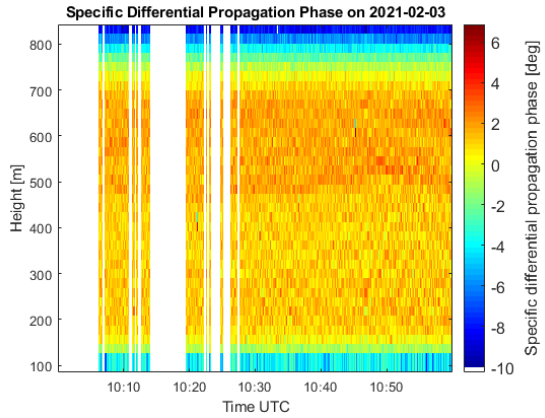

(a) Specific differential phase at 35 GHz without correction

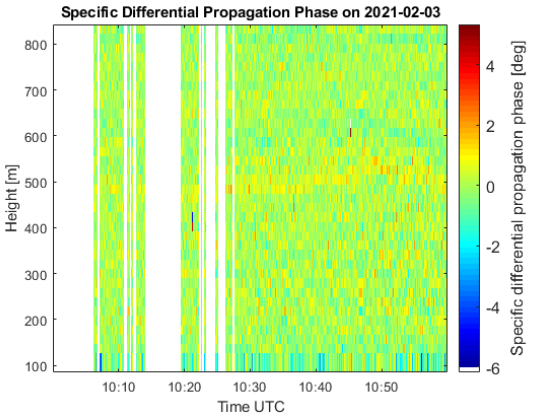

(b) Specific differential phase at 35 GHz with correction

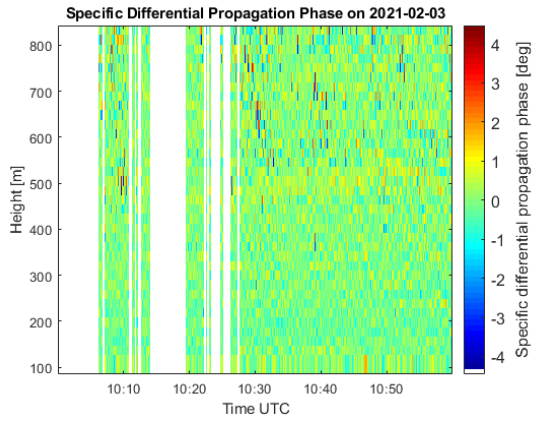

(c) Specific differential phase at 94 GHz without correction

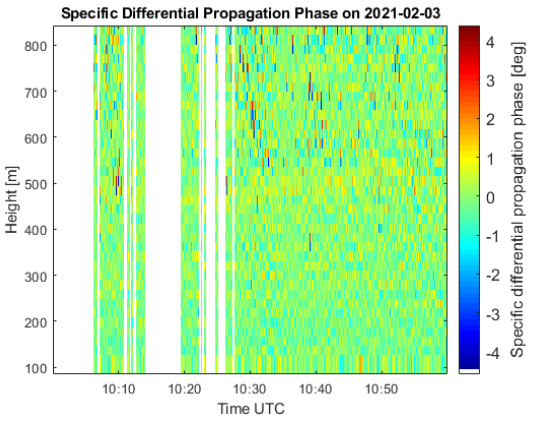

(d) Specific differential phase at 94 GHz with correction

Figure 4.18: Specific differential phase with and without an extra applied polarimetric calibration correction at 35 GHz and 94 GHz on the third of February 2021 from 10:00 to 11:00.

5

Retrieving the Median Volume Diameter

This chapter focuses on the final goal of this research, which is retrieving the raindrop size distribution. Because the raindrop size distribution is assumed to follow a gamma distribution, only 3 parameters needs to be estimated, which are the median diameter D_0, the shape parameter μ and the intercept parameter N_w. Due to the limited time of a Master Thesis Project, the focus in this research was given to estimating D_0 and the remaining parameters μ and N_w were therefore not estimated. However, a parameter was found that might be of use to retrieve N_w, D_0, μ or the rainfall rate. This parameter can be found in Appendix C. The differential backscatter phase (δ_{co}) will be used to estimate D_0. Therefore, first the consistency of δ_{co} will be checked in section 5.1. After this, D_0 will be retrieved by using the estimation of δ_{co} in section 5.2. Thereafter, in section 5.3 the consistency of D_0 will be checked. Finally, in section 5.4 the estimated D_0 will be compared with measurements from a disdrometer.

5.1. Consistency of the δ_{co} Estimation

In section 4.2, there was discussed how δ_{co} is estimated. What, however, is not checked yet, is how consistent this estimation of δ_{co} is. To verify this, some example plots will be given. As the real δ_{co} is not known, one has to check for expected and unexpected properties of these plots. For example, one can expect that δ_{co} does not vary a lot over small heights differences or small time differences. The first plot to verify the consistency of δ_{co} is shown in Figure 5.1. The first notable thing when looking at the 35 GHz plot is that the size of the differential backscatter phase is sometimes lower than 0 deg, which is not expected to be possible by simulations (Figure 4.11). Even the mean δ_{co} over height is often approximately equal to zero. To check if these negative values of δ_{co} are mainly present because of the uncertainty of the measurement, the same plots are made again, but this time highest value of the confidence interval of the differential backscatter phase is plotted, which is equal to the differential backscatter phase plus the margin of error of the differential backscatter phase. These plots can be seen in Figure 5.2. As can be seen, the mean is now always well above 0 deg. There are however, still height bins that show negative values at certain times. A possible explanation could be that the real δ_{co} value is indeed very close to 0 and that the uncertainty of δ_{co} leads to the negative values. An other possibility is that there is a bias in δ_{co} for an unknown reason. When looking at Figure 5.1 again, one can see that the spread in δ_{co} over height is significant, but the mean shows a clear upward trend during between 10:45 and 11:00 for the 35 and 94 GHz band. This means that the raindrop size distribution changes during this last quarter, which is confirmed by the increase in rainfall rate in Figure 3.2, and that both frequency bands give consistent results.

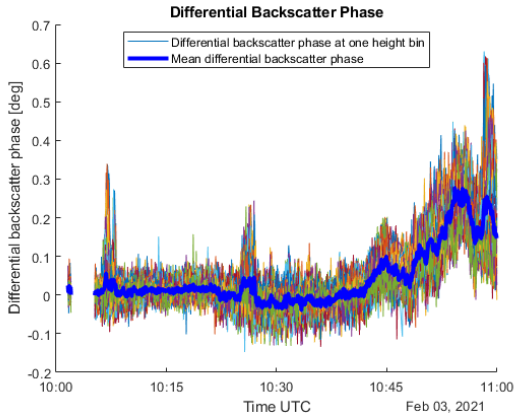

(a) 35 GHz

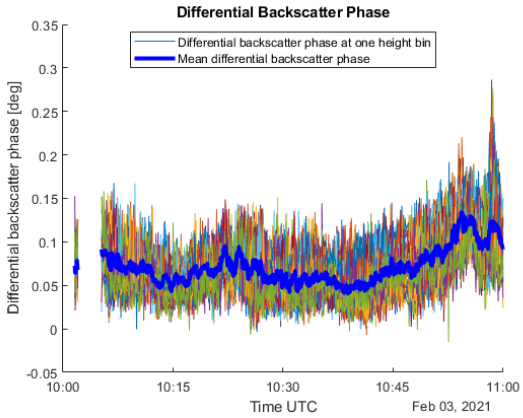

(b) 94 GHz

Figure 5.1: The differential backscatter phase as a function of time for the 35 GHz band and 94 GHz band. Every height bin is represented with a different colored graph. The bold blue line represents the mean of δ_{co} of all height bins as a function over time.

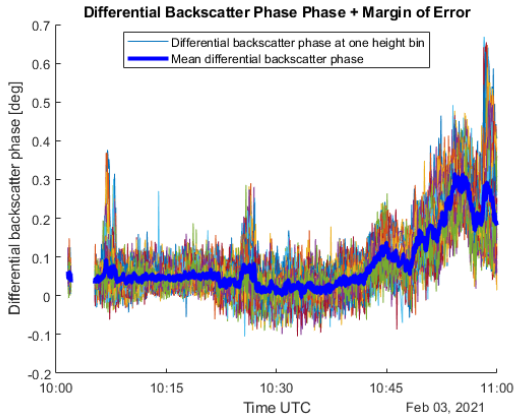

(a) 35 GHz

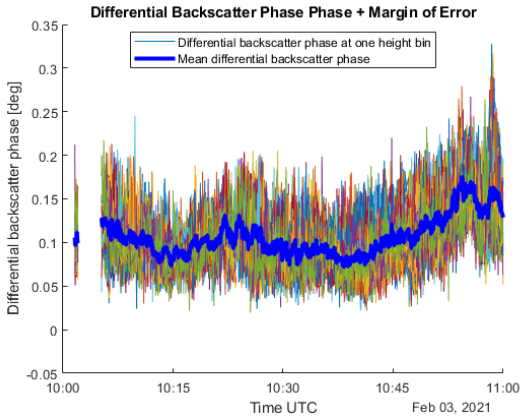

(b) 94 GHz

Figure 5.2: The differential backscatter phase plus the margin of error of the differential backscatter phase as a function of time for the 35 GHz band and 94 GHz band. Every height bin is represented with a different colored graph. The bold blue line represents the mean of δ_{co} plus the margin of error of δ_{co} of all height bins as a function over time.

Another way to verify the consistency of δ_{co} is to create similar plots like in Figures 5.1-5.2, but this time, take the mean over time and plot δ_{co} as a function of height. One can see the result in Figure 5.3. Again, at 35 GHz, one can see a lot of cases where δ_{co} is negative. Again, to test if this is possibly a result of the uncertainty of δ_{co}, the same plot is made again, but this time the upper boundary of the confidence interval of δ_{co} is plotted instead of just δ_{co}, as can be seen in Figure 5.4. Again, still negative δ_{co} values are present and this could be because of the same reasons as mentioned before. When comparing the mean δ_{co} over time as a function over height (bold blue lines) of Figure 5.3 (a) and (b), one can see a similar shape: the means are about constant up to the height 450 m, then the means decrease and become nearly constant from the height 520 m. These very similar trends of the two different used frequency bands show that the estimates of δ_{co} at 35 and 94 GHz seem to be consistent.

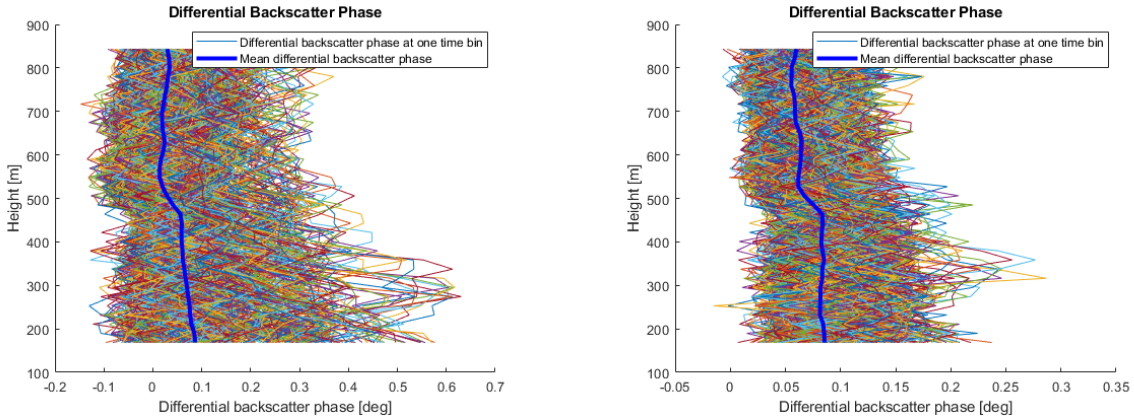

(a) 35 GHz (b) 94 GHz

Figure 5.3: The differential backscatter phase as a function of height for the 35 GHz band and 94 GHz band. Every time bin is represented with a different colored graph. The bold blue line represents the mean of δ_{co} of all time bins as a function over height.

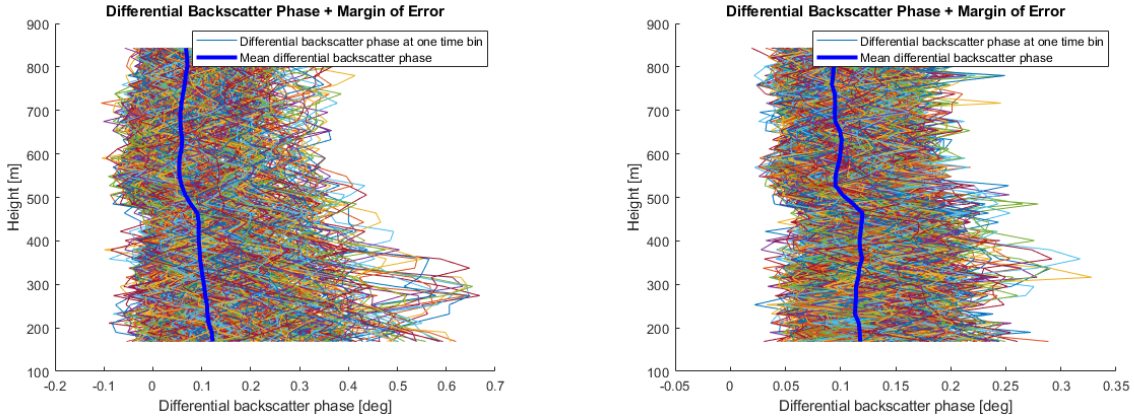

(a) 35 GHz (b) 94 GHz

Figure 5.4: The differential backscatter phase plus the margin of error of the differential backscatter phase as a function of height for the 35 GHz band and 94 GHz band. Every time bin is represented with a different colored graph. The bold blue line represents the mean of δ_{co} plus the margin of error of δ_{co} of all time bins as a function over height.

5.2. Estimating D_0

Having the differential backscatter phase, which has been estimated at 35 and 94 GHz, consistent in time and height, the median diameter (D_0), which is one of the three parameters of the gamma-modeled raindrop size distribution, can be retrieved. To go from δ_{co} to D_0, simulations need to be used to know how they are related at 35 GHz and 94 GHz. The simulations shown in Figure 5.5 from [30] will be used. It will be assumed that D_0 has a value between 0.1 and 2.5 mm and that μ has a value between -2 and 8. These limits are based on a research in Australia, where the rain drop size distribution parameters are estimated with a disdrometer during almost a full season of rainfall and are plotted in a histrogram, as can be seen in Figure 5.6 [9]. The lower limit of D_0 is chosen smaller than 0.5, even though these values cannot be found in the Figure 5.6 (a), because commercial disdrometers generally fail to measure small raindrops [4] and because of the difference between the Australian and Dutch climate. The upper limit of D_0 is chosen to be equal to 2.5 mm, based on the very small tail above 2.5 mm in the histogram of D_0. The lower limit for μ is chosen to be -2, as the histogram shows nearly no occurrence of μ lower than -2. The upper limit is chosen to be 8, based on the histrogram, but also because Bringi mentions in his book [9] that the long tail end ($\mu > 8$) is caused by an artifact. Moreover, on page 538 of the book, simulations made for polarimetric weather radars with the following ranges: D_0 from 0.5 to 2.5 mm and

μ from -1 to 5. These ranges are narrower than the ranges used in this thesis research. However, using a too narrow range in this thesis research may lead to the inability of finding the correct raindrop size distributions for some cases.

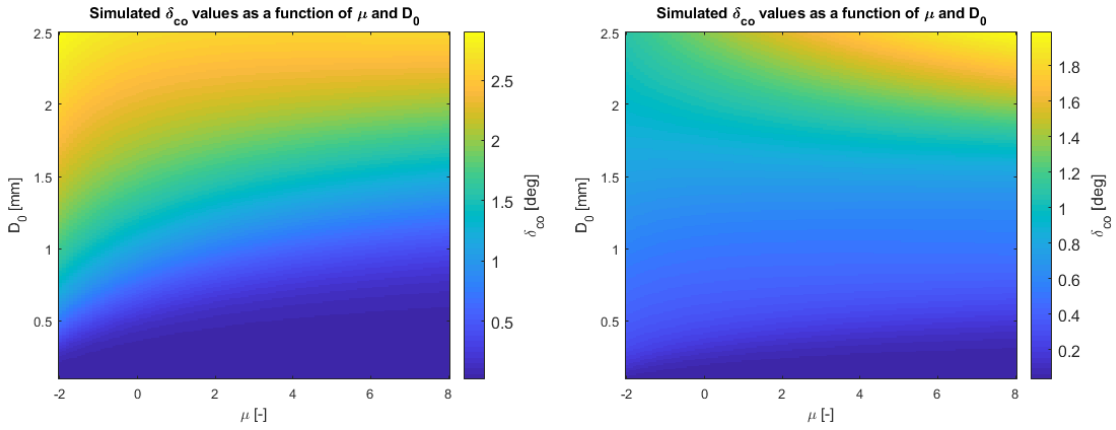

(a) 35 GHz (b) 94 GHz

Figure 5.5: Simulated differential backscatter phase as a function of the the median diameter D_0 and the shape parameter μ for the 35 GHz and 94 GHz. The simulation data were provided by C.M.H. Unal [30]

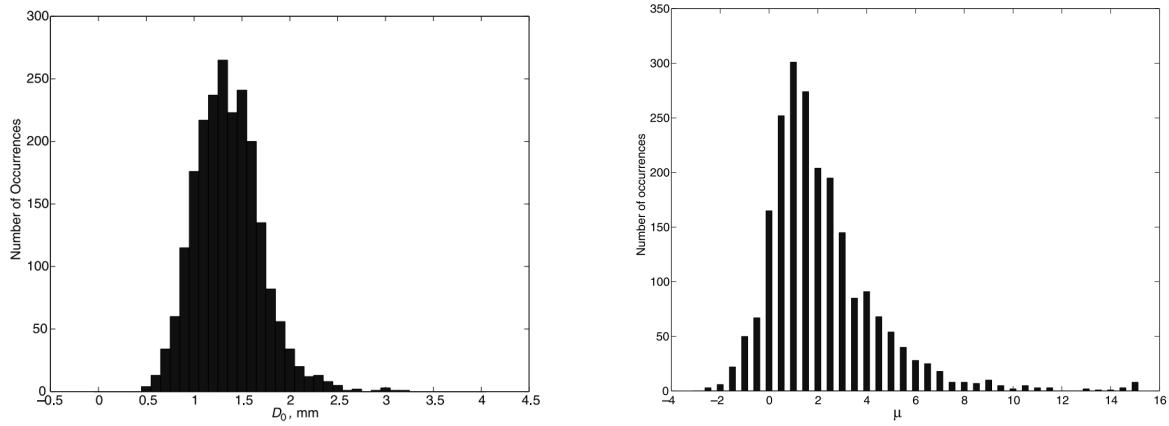

(a) D_0 (b) μ

Figure 5.6: A histogram of D_0 and μ made by using a disdrometer in Australia during almost a full season of rainfall. These figures were taken from page 413 and 414 from [9].

To get an estimate of D_0, the confidence interval of δ_{co} will be used. How the simulation can help to get an estimate of D_0 will be explained by using a simple example. Assume that the confidence interval of δ_{co} is equal to 0.6°-0.8° at 35 GHz. The simulations from Unal (Figure 5.5(a)) can be used to get the possible corresponding values of D_0 and μ when δ_{co} is 0.6°-0.8°. A visualization of this can be seen in Figure 5.7(a). As can be seen, δ_{co} leads to restrictions for D_0, only values of D_0 between 0.46 and 1.26 mm are possible. The sensitivity of μ is clearly lower, as all considered values of μ are still possible. Exactly the same strategy can be applied to the 94 GHz. This results into Figure 5.7(b) when the confidence interval of δ_{co} is again 0.6°-0.8°. Note that this is just an example and the confidence intervals of δ_{co} at 35 and 94 GHz are usually not equal when observing the same volume. At 94 GHz, the plot shows that again, D_0 gets restricted because of the confidence interval of δ_{co}. This time, possible values of D_0 are 1.09-1.62 mm and again, μ is not restricted by the confidence interval of δ_{co}. Note that it is important that the resolution of the simulations is high enough to exclude the possibility that no solution will be found. This can be the case if the resolution of the simulations is low and the confidence

interval of δ_{co} is narrow. In for example, the very extreme case when the confidence interval of δ_{co} at 94 GHz would be 0.60005-0.60006, then no solution is found, while there would certainly be a solution when the resolution of the simulations is extremely high. The resolution of the simulations is 0.01 mm for D_0 and 0.1 for μ for both the 35 and 94 GHz band and this turns out to be high enough so these artifacts will not occur.

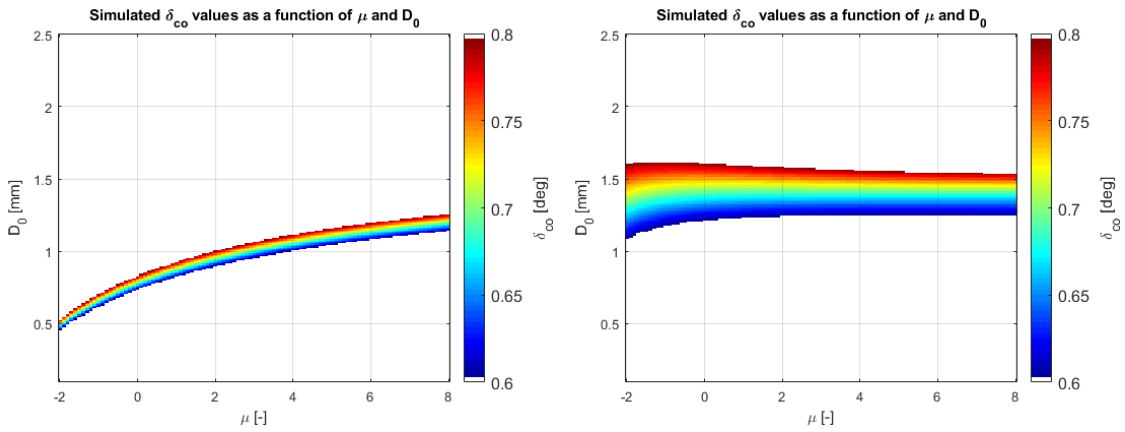

(a) 35 GHz (b) 94 GHz

Figure 5.7: Simulated differential backscatter phase as a function of the the median diameter D_0 and the shape parameter μ for the 35 GHz and 94 GHz. Only values of δ_{co} between 0.6 and 0.8 are shown due to the choice of the color bar. The simulations were provided by C.M.H. Unal [30].

Summarizing, δ_{co} shows a good potentiality to determine an interval for D_0.

At this moment, possible combinations of D_0 and μ can be found by using the confidence interval of δ_{co} at 35 GHz and 94 GHz. This method will now be applied again, but this time on a real case. This example case is on the 3th of February 2021 at 10:59:58 at a height of 169 m. The result can be seen in Figure 5.8. Figure 5.8(a) shows the 35 GHz possibilities of D_0 and μ, Figure 5.8(b) shows the 94 GHz possibilities and Figure 5.8(c) shows the overlap between Figure 5.8(a) and Figure 5.8(b).

As can be seen, unfortunately, in this case, there is no overlap between the two frequency results, while they observe (largely) the same volume. That is the worst-case scenario indicating that the confidence interval may be too narrow or there is an error in the estimation of δ_{co} for one frequency band. This of course means that at least not both frequencies give the correct result. In a perfect scenario, the 35 GHz and 94 GHz solution do overlap and this can even give restrictions for μ. This can for example be seen in Figure 5.9. Unfortunately, this turns out to be a rare scenario. Generally, when there is overlapping of the solutions, a $D0$ interval can be found but the μ interval stays too large due to the lack of sensitivity of δ_{co} for changes in μ, especially at 94 GHz for intermediate values of D_0 (see Figure 5.10).

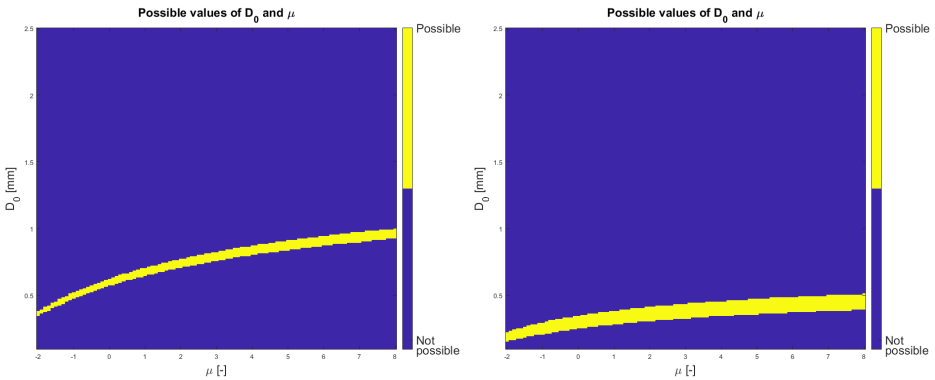

(a) 35 GHz (b) 94 GHz

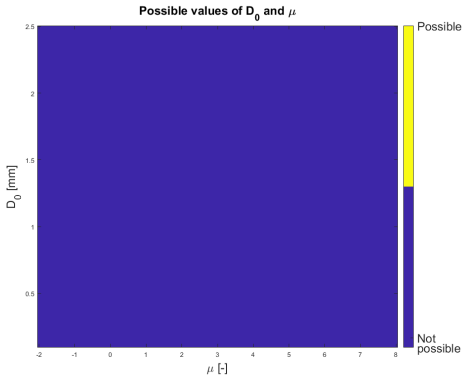

(c) Combined 35 and 94 GHz

Figure 5.8: Possible D_0 and μ values found by using an estimate of δ_{co} and combining this with simulations at 35 GHz, 94 GHz and the combined possibilities (overlap). This example case is on the 3th of February 2021 at 10:59:58 at a height of 169 m.

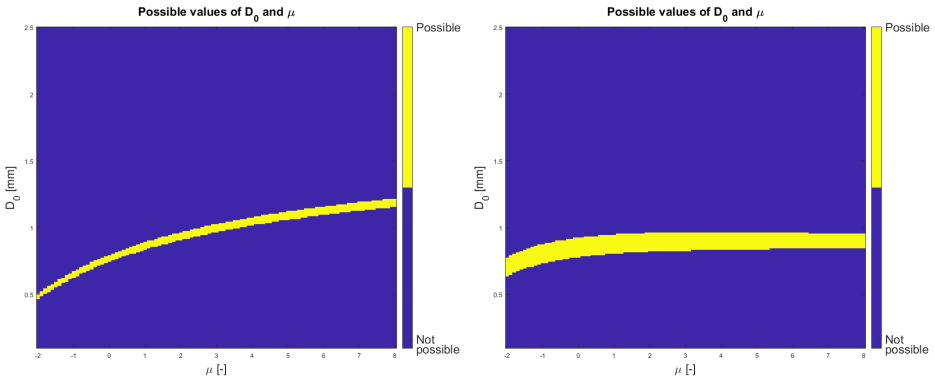

(a) 35 GHz (b) 94 GHz

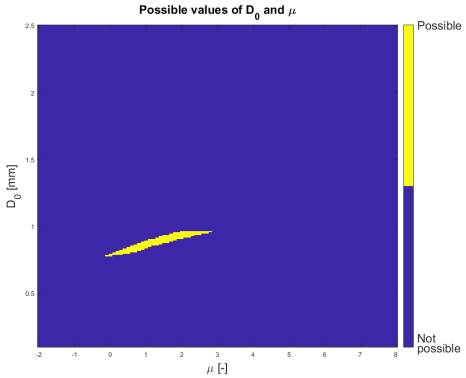

(c) Combined 35 and 94 GHz

Figure 5.9: Possible D_0 and μ values found by using an estimate of δ_{co} and combining this with simulations at 35 GHz, 94 GHz and the combined possibilities (overlap). This example case is on the 21st of January 2021 at 03:13:07 at a height of 169 m.

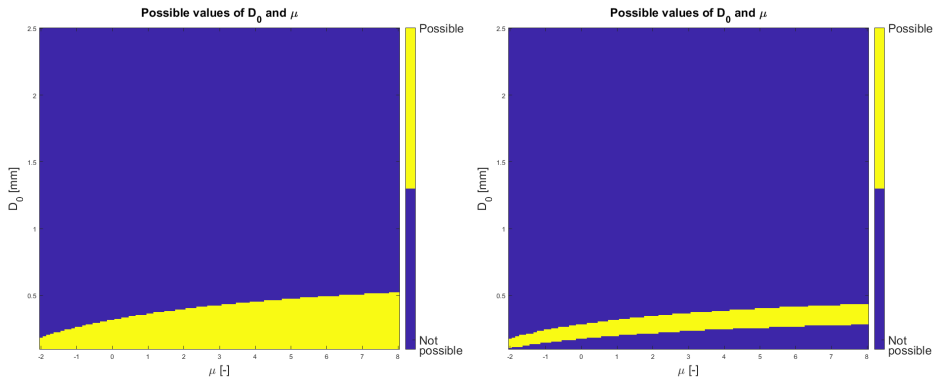

(a) 35 GHz

(b) 94 GHz

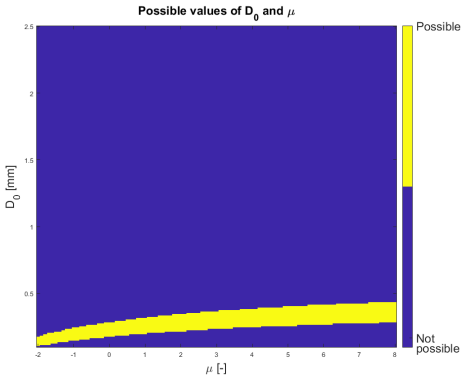

(c) Combined 35 and 94 GHz

Figure 5.10: Possible D_0 and μ values found by using an estimate of δ_{co} and combining this with simulations at 35 GHz, 94 GHz and the combined possibilities (overlap). This example case is on the 3th of February 2021 at 10:23:55 at a height of 169 m.

5.3. Consistency of the D_0 Estimation

In the previous section, it was explained how D_0 is estimated in three different ways, one way by using the confidence interval of δ_{co} at 35 GHz, one way by doing the same at 94 GHz and one way where both methods are combined. In this section, the focus will be on verifying whether the results of δ_{co} of these three methods show consistent results. To check the average results of these methods, some plots will be made. First, the mean of the minimum and maximum found possible D_0 values over all height bins is obtained to get a plot of the mean confidence interval for the retrieval of D_0 as a function of time. Note that D_0 is not necessarily constant over height, but this plot will be made to verify whether the right trends can be seen. The results are shown in Figure 5.11. As can be seen, the maximums of the 35 and 94 GHz show a similar upward trend during the last quarter of the hour, just like the rainfall rate during this hour (Figure 3.2). This means that it is likely that the rainfall rate increased in this last quarter, because of an increase of D_0, possibly in combination with a change of μ and N_w. When comparing the values of the average maximums, one can see that the 35 GHz also finds solutions with higher D_0 values than the 94 GHz. The minimums of both frequencies are often close to the minimum considered one of 0.1 mm.

These 3 different methods do not always find a possible solution. First of all, the methods are only applied if the rainfall rate is above 0 mm/h. Secondly, if can be that the Rayleigh plateau cannot be found and thirdly, no D_0 solution can be found that corresponds to the found confidence interval of δ_{co}. At last, the combined method of 35 and 94 GHz can also lead to no solution when no overlap is found between the D_0/μ solutions, like in Figure 5.8. For this hour under study, there was no solution for the 35 GHz band in 18.1% of the cases when the rainfall rate was higher than 0 mm/h. For the 94 GHz band, this percentage was only 0.1% and for the combined method, it reached 44.3%. This means that the 94 GHz method is the most consistent in finding results. It was not unexpected that the 35 GHz

method would have more problems with finding a solution, as there are clearly cases where the full confidence interval of δ_{co} is estimated to be below 0 deg in Figure 5.2(a), while simulations show that this should not be possible (Figure 5.5).

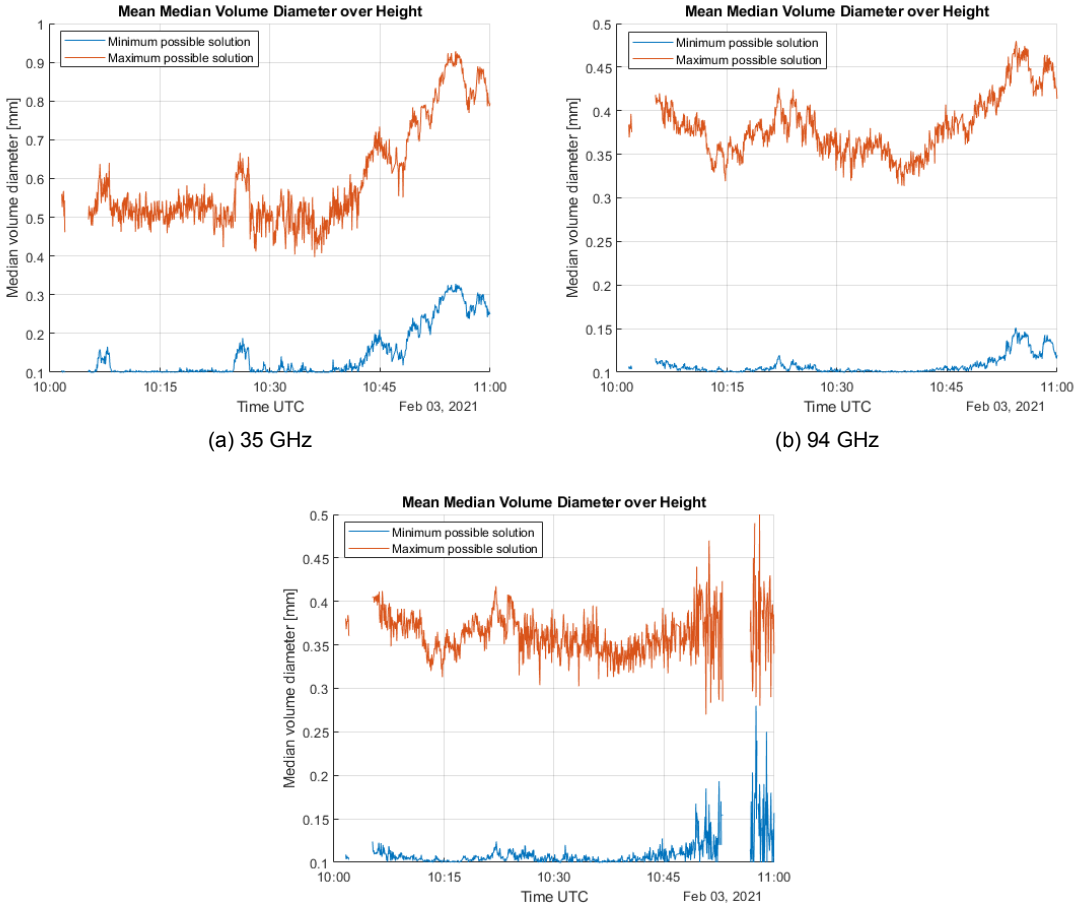

(a) 35 GHz

(b) 94 GHz

(c) Combined 35 and 94 GHz

Figure 5.11: Mean possible D_0 minimum and maximum solution over height as a function of time found by using an estimate of δ_{co} and combining this with simulations at 35 GHz, 94 GHz and the combined possibilities (overlap).

It is also interesting to check the mean behaviour of D_0 over height. To do this, the mean minimum and maximum D_0 values are taken over time and are plotted as a function of height, as can be seen in Figure 5.12. One can see that there is a similar trend for the maximum possible solution for all 3 methods. Especially the downward trend around 500 m is clearly present at all 3 methods.

Summarizing, both frequency results show consistent trends. To be able to further analyze these confidence intervals for the D_0 retrieval, ground truth using disdrometer measurements is considered next.

5.4. Comparing D_0 Estimates with Disdrometer Measurements

In the last section, the consistency was checked for the 3 estimation methods of D_0. In this section, the estimates of D_0 will be compared with the measurements of a disdrometer. The disdrometer, which was introduced in section 3.5, is located on the surface, 150 m away from the cloud radar. Because the cloud radar does not observe the surface, only relatively low height bins will be considered for this comparison. More specifically, the average of the 5th until the 7th height bin will be used. This is from 169 m to 211 m. This average was taken of 3 height bins to decrease the effects of random errors. It was assumed that the rain drop size distribution is constant during these 3 height bins. The lowest

4 height bins are not used, as the lowest height bins show unreliable estimates of δ_{co} as mentioned before in section 4.2. The retrieved mass-weighted mean diameter (D_m) as a function of time from the disdrometer was provided by Christos Gatidis using the methodology of [31].

5.4.1. Comparing D_0 with D_m

Fortunately, the mass-weighted mean diameter, which is obtained with the disdrometer, is closely related to the median volume diameter. Bringi gave equations in his book to calculate both parameters in the case of a gamma distribution [9]:

$$\lambda D_m = 4 + \mu \tag{5.1}$$

$$\lambda D_0 = 3.67 + \mu \tag{5.2}$$

where λ is the slope parameter [-]. Dividing Equation 5.1 by Equation 5.2 leads to the relation between D_m and D_0:

$$\frac{D_m}{D_0} = \frac{4 + \mu}{3.67 + \mu} \tag{5.3}$$

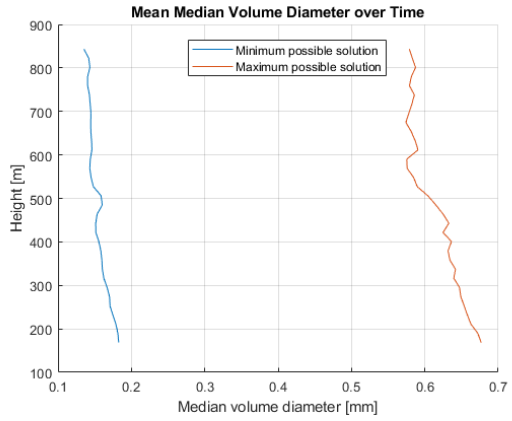

(a) 35 GHz

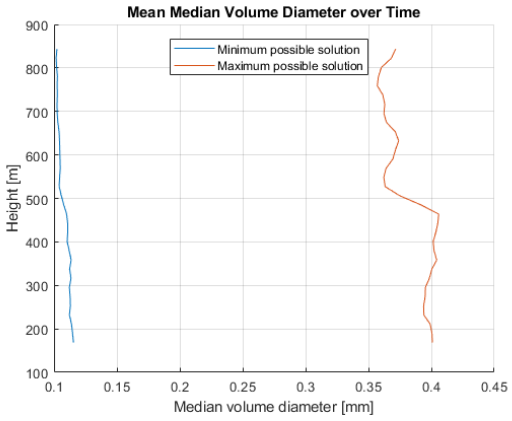

(b) 94 GHz

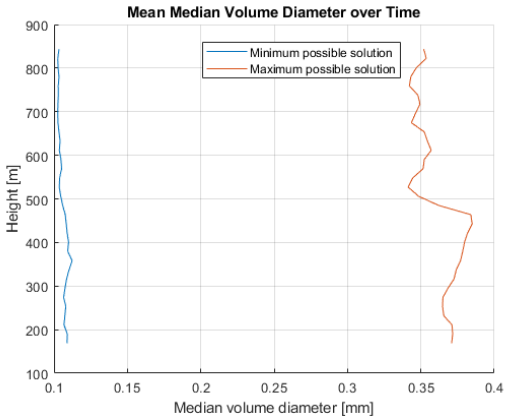

(c) Combined 35 and 94 GHz

Figure 5.12: Mean possible D_0 minimum and maximum solution over time as a function of height found by using an estimate of δ_{co} and combining this with simulations at 35 GHz, 94 GHz and the combined possibilities (overlap). The used data is from February 03 2021, from 10:00-11:00.

Unfortunately, the shape parameter of the raindrop size distribution (μ) is not known. However, to see how much D_m and D_0 can differ for different values of μ, a plot of the ratio of D_m and D_0 is made as a function of μ in Figure 5.13. In this research the assumption was made that μ is always between -2 and 8. This implies that the highest difference between D_m and D_0 is when μ is equal to -2 and D_m is then 20% larger than D_0. Note that also for all other values for μ, D_m is bigger than D_0. This means that when comparing D_m found by the disdrometer with D_0 found with the cloud radar, it is expected that D_m from the disdrometer is always bigger. For completeness, two estimates of μ using the disdrometer data and different estimation models, are given in Figure 5.14. As can be seen in these estimates, μ seems to vary a lot in time. Moreover, the two different models show significant different results. Because of the uncertainty of the estimates in μ, these estimates will not be used to convert the estimate of D_m of the disdrometer to D_0. This means that the estimate of D_m of the disdrometer will be compared with the D_0 estimates of the cloud radar, knowing that D_m is expected to be between 3% and 20% higher than D_0.

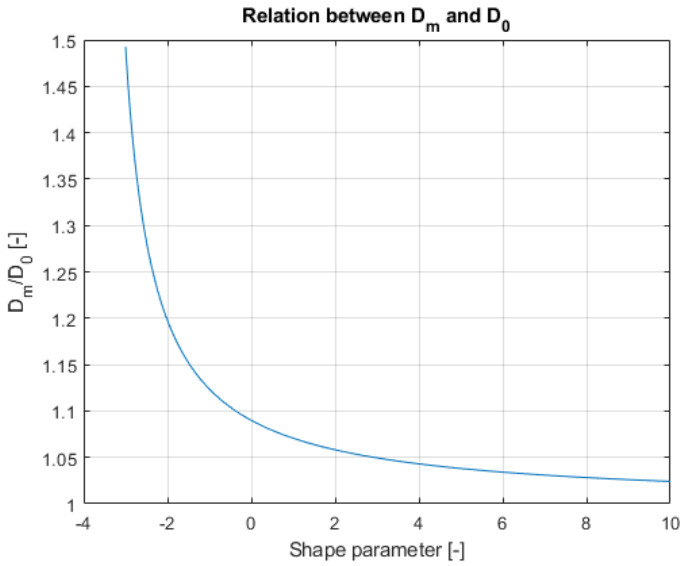

Figure 5.13: The relation between D_m and D_0 as a function of μ when assuming a gamma distribution.

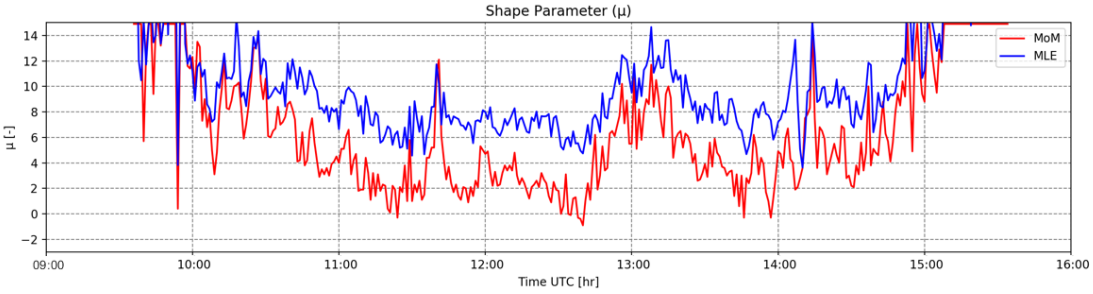

Figure 5.14: Retrieval of the shape parameter of the gamma distribution obtained from the disdrometer data using two different estimation techniques. These results are provided by Christos Gatidis based on [31]

5.4.2. Time Lag Correction

The result for the 35 GHz, 94 GHz and combined estimate of D_0 can be seen in Figure 5.15. Figure 5.15(a) shows that the 35 GHz D_0 estimate and the disdrometer D_m estimate show the same trends during most of the time. Especially between 13:45 and 14:45 one can see that the radar and disdrometer show peaks at about the same moments. A time lag correction is applied of 2 minutes to the retrieved D_0 with the cloud radar. This is done, because the peaks of the radar were slightly earlier than the ones of the disdrometer. First, it will be explained how this time lag is determined and

after that, it will be explained why it is expected that such a time lag correction is needed. The time lag correction was determined by finding the time lag with the maximum cross correlation between the mean possible D_0 and D_m found by the disdrometer. To calculate this, first, the time resolution of the retrieved D_0 was lowered to 1 minute by using the retime function of MATLAB, to match the time resolution of D_m found by the disdrometer. This method is applied by using the mean D_0 at 35 GHz and 94 GHz and both resulted in a time lag of 2 minutes. To illustrate that this time lag indeed improves the matching of the retrieved D_0 with D_m of the disdrometer, Figure 5.16 shows again Figure 5.15(b), but without the applied time lag correction of 2 minutes. It is clearly visible when comparing these two figures that local peaks of D_0 from the cloud radar and D_m from the disdrometer are matching better with the applied time lag correction of 2 minutes.

But why was the need for this time lag correction expected? It was expected, as the raindrops are first measured by the radar at heights from 169 m to 211 m and these rain drops then still need to fall to the surface, which will create a small time difference. To get a sense of what time lag to expect, a simple fall velocity model will be used to calculate how much time it approximately takes for a drop to fall from 190 m to the surface. The following exponential fall velocity model is given in Bringi [9]:

$$v(D) = \alpha D^{\beta} \tag{5.4}$$

where v is the fall velocity in m/s, α is a coefficient often taken as 3.78, D is the drop size in mm and β is a coefficient often taken as 0.67. Applying this equation results in fall velocities of 2.38 m/s, 3.78 m/s and 4.96 m/s for raindrop diameters of 0.5 mm ,1.0 mm and 1.5 mm, respectively. This corresponds to time lags of 80 s, 50 s and 38 s when the drops fall vertically from 190 m to the surface, respectively. In practise, these time lags can be different for multiple reasons, like non vertical rainfall due to horizontal wind and the uncertainty of the fall velocity model. Moreover, the time resolution for the disdrometer is one minute, while the time resolution of the cloud radar is 3.6 seconds. This can also lead to an earlier peak of D_0 of the cloud radar.

This effect may be amplified with the distance between the cloud radar and disdrometer, and the looking direction of the cloud radar at 45° elevation at an azimuth not in the direction of the disdrometer. In conclusion, the time lag correction of 2 minutes is in line with what one could expect.

5.4.3. Cross Correlation Between D_0 and D_m

Figure 5.15(b) shows the result of the found D_0 for the cloud radar at 94 GHz. One can clearly see that the minimum and maximum possible D_0 that was found with the cloud radar is highly correlated with the estimated D_m of the disdrometer. More specific, the normalized cross correlation between the mean D_0 and D_m was 0.845 at 94 GHz and also 0.845 at 35 GHz. Almost during the full 5 hour dataset, even small peaks of D_m of the disdrometer correspond to small peaks of D_0 of the cloud radar. The peaks of D_0 of the cloud radar looks to be a bit sharper than the peaks of D_m of the disdrometer. This can be due to the different time resolution of the two devices. If, for example, D_0 and D_m would suddenly increase for 20 seconds and then suddenly decrease to the old D_0 value again, the cloud radar will be able to show this easily, because the time resolution is 3.6 seconds. The disdrometer will also show a peak, because the mean D_m of this minute will be higher due to these 20 seconds with a higher value of D_m, however, the peak will be lower, because these 20 seconds will be averaged together with 40 seconds where D_m is lower.

5.4.4. Observed Bias

What is also noticeable, is that D_m of the disdrometer is (almost) always bigger than the maximum possible D_0 found with the cloud radar. As discussed before, it is expected that D_m is 2 to 20% larger than D_0, but the differences are clearly larger in Figure 5.15(b). This means that there is a bias related to the estimation. Does it come from the cloud radar retrieval and/or disdrometer data? To show that the total bias between D_0 of the cloud radar and D_m of the disdrometer is fairly constant at 94 GHz, the mean difference between the mean possible D_0 from the cloud radar and D_m from the disdrometer (0.79 mm) is added to the minimum and maximum possible D_0 from the cloud radar and this is shown

in Figure 5.17. One can see that adding a constant value already leads to a good agreement between the cloud radar and the disdrometer. The goal of this plot was to show that there is a fairly constant bias in this time series and it must be emphasized that this is not a proof that this is generally the case. Furthermore, this offset of 0.79 mm is overestimated because D_m should be larger than D_0.

To verify whether the bias is systematically present, it is advised to investigate more time series. A possible reason for a bias is that the disdrometer is not able to measure small raindrops, which results in an overestimation of D_m. To check this, Figure 5.18 will be analyzed. It shows a plot where one can see the amount of drops that were measured with a certain drop size versus time. One can see that no drops can be measured lower than 0.25 mm. Moreover, when closely watching at the lowest drop diameter bin, it seems to be underestimated as this bin shows really low values, while only one bin above it also shows really high values. Thus, no drops smaller than 0.25 mm are measured and the number of raindrops with diameters between 0.25 and 0.375 mm is underestimated. Another possible reason for the bias could be the influence of the chosen axis ratio size model for the simulations. One could check whether the bias is still present when a different model is used.

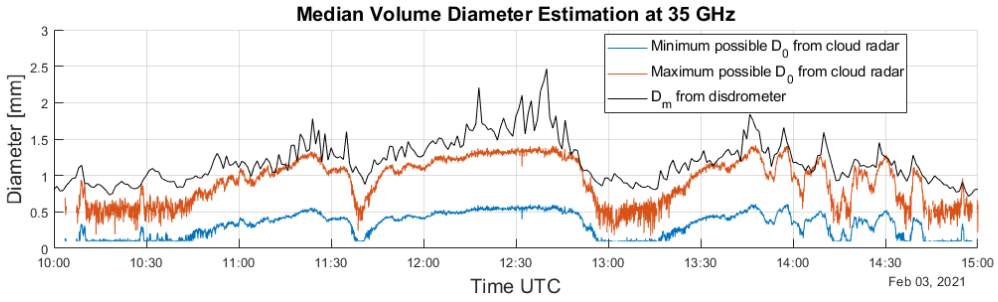

(a) 35 GHz

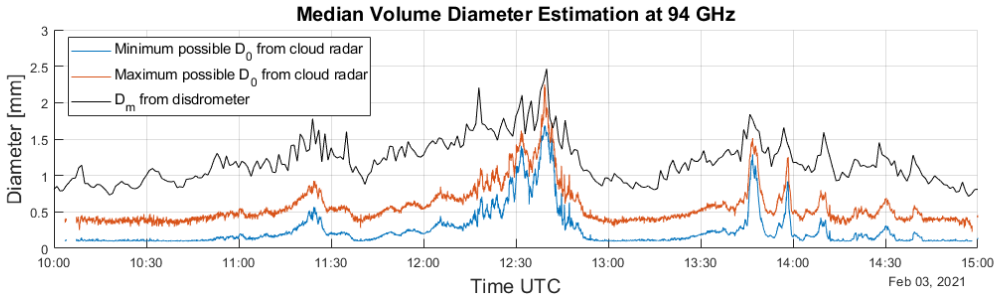

(b) 94 GHz

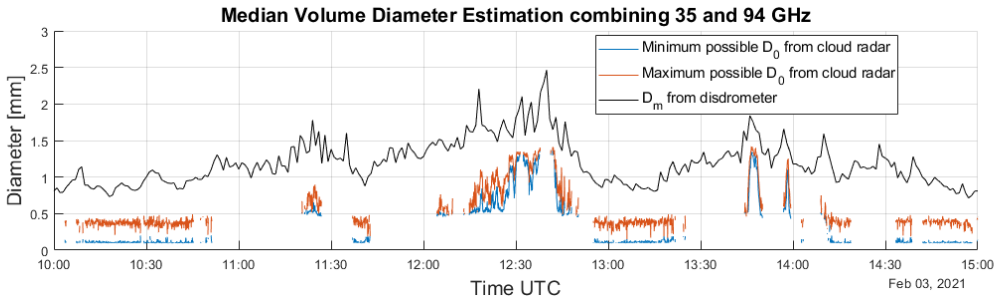

(c) Combined 35 and 94 GHz

Figure 5.15: Estimates of the minimum and maximum possible median diameter from cloud radar measurements from a height of 169 m until 211 m with an applied time lag correction of 2 minutes and the estimated mass-weighted mean diameter from disdrometer measurements on the surface located 150 m away from the cloud radar. D_m found by the disdrometer (black line) was provided Christos Gatidis based on [31].

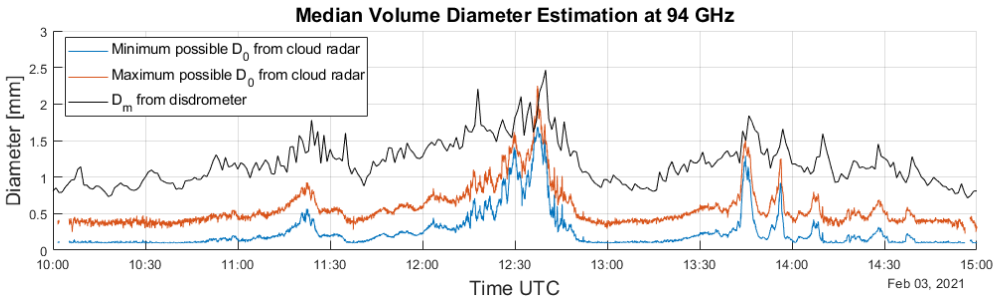

(a) 94 GHz

Figure 5.16: Estimate of the minimum and maximum possible median diameter from cloud radar measurements at 94 GHz from a height of 169 m until 211 m and the estimated mass-weighted mean diameter from disdrometer measurements on the surface located 150 m away from the cloud radar. D_m obtained from the disdrometer data (black line) was provided by Christos Gatidis [31].

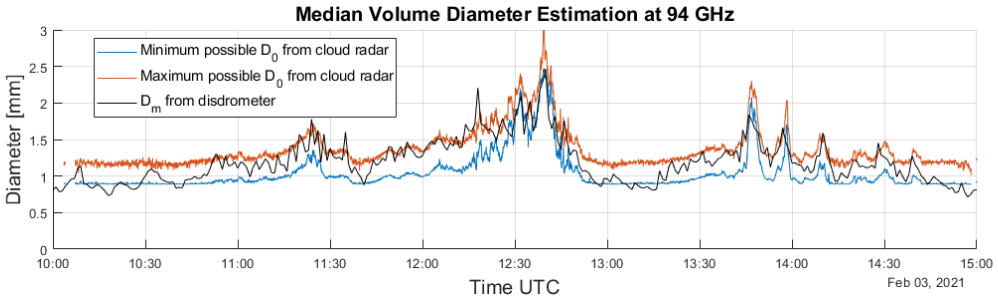

Figure 5.17: Estimates of the minimum and maximum possible median diameter from cloud radar measurements from a height of 169 m until 211 m with an applied time lag correction of 2 minutes and with an added bias on top of it of 0.79 mm and the estimated mass-weighted mean diameter from disdrometer measurements on the surface located 150 m away from the cloud radar. D_m obtained from the disdrometer data (black line) was provided by Christos Gatidis [31].

5.4.5. Recommendations

Are the D0 values retrieved from the 94 GHz frequency underestimated? To investigate this, a few recommendations are provided:

- Check whether a bias of D_0 is also present during other time series
- Check whether the bias of D_0 is caused by the choice of the axis ratio-size model in the simulation
- Investigate if one can find an estimate of the bias on D_m given by the disdrometer knowing that the raindrops having a size below 0.375 mm cannot be well measured.
- For the cloud radar, the simulation should provide δ_{co} versus D_m and μ.
- Considering the time resolution, the cloud radar data/retrievals could be averaged to have the same time resolution as the disdrometer one. However, this procedure will increase the cloud radar resolution volume with maybe a detrimental effect in the comparison cloud radar-disdrometer.

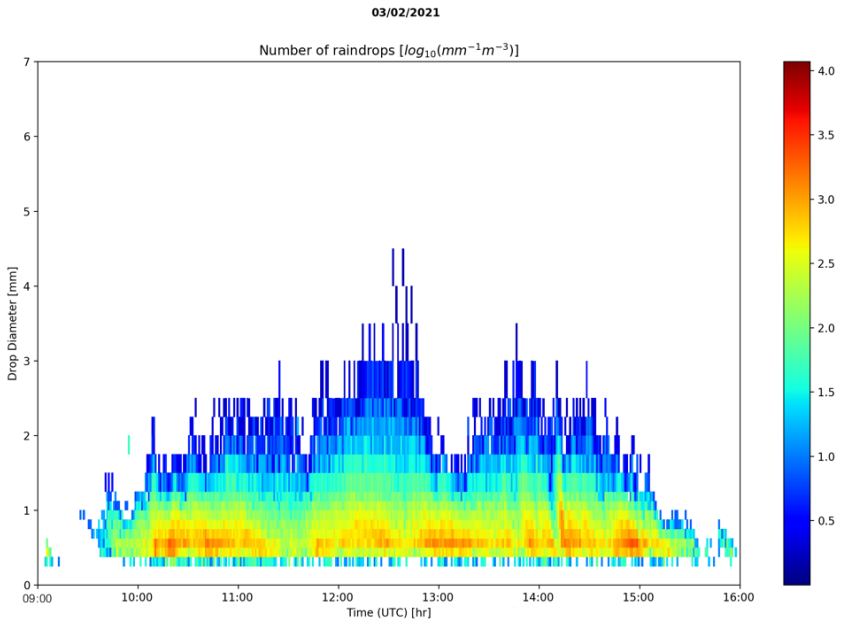

Figure 5.18: Raindrop sizes measured by a disdrometer at Cabauw. This plot is provided by Christos Gatidis based on [31].

5.4.6. Width of the Confidence Interval at 94 GHz

What is also notable is that the difference between the minimum and maximum found D_0 solution with the cloud radar at 94 GHz seems to decrease when D_0 increases. This means that the method to find D_0 with the cloud radar at 94 GHz shows the most potential for estimating D_0 when D_0 is large. To investigate this further, a scatter plot is made in Figure 5.19 to find the mean D_0 value where the method will give the most narrow solution. It is important to emphasize that the plot is only based on one time series of 5 hours of data. One can see in the plot that, in the considered time series, when the mean D_0 solution was between 1.3 and 1.65 mm, a narrower interval solution is found compared to the one with a mean D_0 higher or lower. However, also narrow interval solutions are found when the mean D_0 is very small. That can be explained by the fact that the minimum found solution cannot be lower than 0.1 mm, since this is the lower bound for D_0 in this retrieval technique. Of course, also if smaller D_0 possibilities would be taken into account, the minimum solution would be always limited by the fundamental minimum of 0 mm. In the considered time series, the maximum found solution is never limited by the maximum considered possible D_0 value of 2.5 mm. If this would be the case, then it is advised to increase this limit of 2.5 mm.

5.4.7. Combined Method

Finally, Figure 5.15(c) shows the result of the D_0 estimation of the strategy where both 35 and 94 GHz frequency bands are used. Unfortunately, this technique has not found a solution for a large amount of time bins. However, when there is a found solution, then this solution is close to the 94 GHz one but with a narrower interval. This combined method should be further investigated. It reveals the issue to be explored: why can't we match these two results (35 and 94 GHz) most of the time? This also shows the importance to use a dual-frequency system to get more understanding in the measurements, the retrieval technique and the simulation.

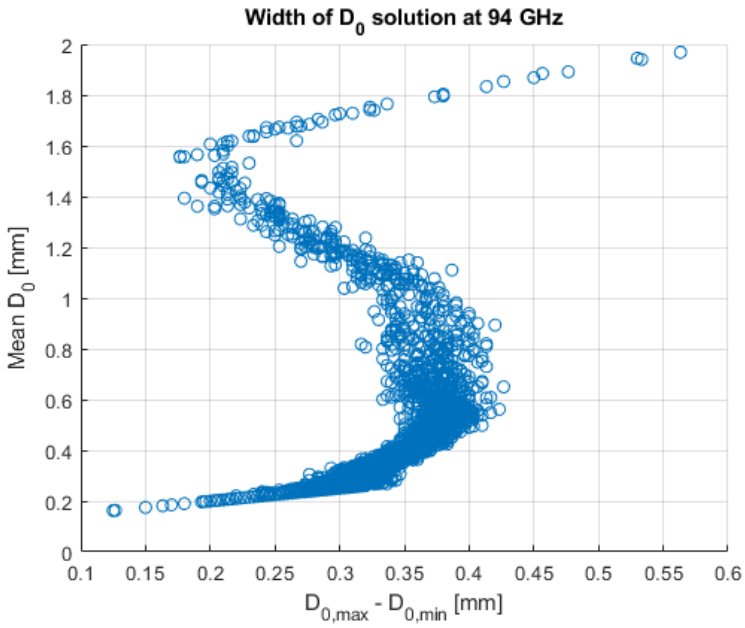

Figure 5.19: The width of the solution of D_0 of the cloud radar at 94 GHz (difference between the maximum and minimum found cloud radar) versus the mean solution of D_0 of the cloud radar at 94 GHz. The considered solutions are the solutions from the time series of Figure 5.15(b).

6

Conclusions and Recommendations

Conclusions about this research will be drawn by first answering the 6 research sub-questions and finally answering the main research question. After this, some recommendations will be given.

6.1. Answers to the Research Sub-questions

6.1.1. Are the polarimetric measurements well calibrated?

While investigating the polarimetric variables, in particular the differential phase, this phase did not show the expected trend of the simulation and exhibited significant discrepancies in values comparing both frequency bands. Therefore, it became necessary to enter in contact with the senior scientist of the RPG company (manufacturer of the dual-frequency cloud radar). A. Myagkov explained that an extra polarimetric calibration was necessary. Drizzle measurements were used to calculate polarimetric calibration correction values since the expected differential phase and differential reflectivity are known and equal to 0 deg and 1, respectively. The 94 GHz polarimetric calibration correction is relatively small, while the correction of the 35 GHz measurements is fairly large. This means that the 94 GHz was already calibrated well polarimetrically, while the extra polarimetric calibration correction was essential at 35 GHz.

6.1.2. How to disentangle propagation and backscattering effects?

The Doppler spectra are used to disentangle propagation and backscattering effects. Smaller raindrops fall slower than larger raindrops and this results in a difference in Doppler velocities between relatively small and larger raindrops. The presence of wind, turbulence and Doppler aliasing complicates the situation. However, as small raindrops fall with different velocities than larger drops, they can still be found in a different part of the Doppler spectrum. Small raindrops scatter in the Rayleigh regime and because of this, the spectral differential backscatter phase is equal to 0 deg. Therefore, the spectral differential phase measurements are only caused by propagation. The specific Doppler velocities which correspond to Rayleigh scattering can be found by the proposed Rayleigh plateau detection algorithm in this thesis. This algorithm first filters out Doppler velocities with properties differing from expectations, like a spectral differential reflectivity higher than 1.1. Another important property that is used to find the Rayleigh plateau is the little variation of the spectral differential reflectivity and spectral differential phase over Doppler velocity at the Rayleigh plateau. Using these properties, a cost function is defined to find the best Rayleigh plateau option. This algorithm is applied on all height and time bins. In conclusion, this algorithm extracts propagation only effects in the spectral differential phase.

6.1.3. How can the differential backscatter phase be estimated?

The differential backscatter phase is equal to the differential phase minus the differential propagation phase. The differential phase is measured by the cloud radar. The differential propagation phase can be calculated by using the detected Rayleigh plateau. This is simply done by taking the mean spectral differential phase value at the Rayleigh plateau. A strong property is the independence of polarimetric calibrations.

6.1.4. How can the error of the differential backscatter phase be evaluated?

The differential backscatter phase is calculated as the difference of the differential phase and the differential propagation phase. In this research, the random error of the differential backscatter phase is assumed to be equal to the error of the differential propagation phase. This assumption is considered because the random error of the differential phase is much smaller than the random error of the differential propagation phase, as the differential phase is calculated by including a lot more measurements than the differential propagation phase. The random error of the differential propagation phase is estimated by using the re-sampling method bootstrapping. This is done as the differential propagation phase can be calculated as the mean of less than 30 measurements and moreover, one does not have to assume that the differential propagation phase is normally distributed when using bootstrapping. Bootstrapping leads to the (95%) confidence interval of δ_{co}.

6.1.5. How can the median volume diameter be retrieved from the estimate of the differential backscatter phase?

Simulations show what value of δ_{co} corresponds to combinations of possible values of D_0 and μ. δ_{co} is independent of N_w. It is assumed in this research that D_0 is between 0.1 and 2.5 mm and μ is between -2 and 8. It is checked which combinations of D_0 and μ correspond to values inside the confidence interval of δ_{co}. In this way, possible combinations of D_0 and μ are found for all time and height bins. This method is applied for both the 35 and 94 GHz frequency band of the cloud radar. Moreover, the overlap of the possible D_0/μ combinations of 35 and 94 GHz is estimated, which narrows down the possible solutions. However, no overlap is found in 44.3% of the cases for a time series of one hour, which indicates that more research needs to be done to find the reason for this. The combinations of D_0/μ for the 35 GHz, 94 GHz and the overlap of them contain all possible values of μ in most cases, which means that μ is not restricted by the confidence interval of δ_{co}. D_0 is however, always restricted by the confidence interval of δ_{co}. The 94 GHz frequency band restricts D_0 more than the 35 GHz frequency band. The overlap between the possible D_0/μ values at 35 and 94 GHz restricts D_0 even more and in rare occasions even restricts μ.

6.1.6. How does the retrieved median volume diameter compare with disdrometer measurements?

The confidence interval of D_0 obtained with the 35 GHz frequency band, 94 GHz frequency band and the overlap of the two frequency bands were all compared to the mass-weighted mean diameter (D_m) found by a disdrometer which is located on the surface 150 m away from the cloud radar. This comparison is done for 5 consecutive hours of rain. The median volume diameter retrieved with the 35 and 94 GHz frequency bands shows a normalized cross correlation coefficient of 0.845 with the measured D_m of the disdrometer. D_m is expected to be between 2 and 20% larger than D_0. However, D_m found by the disdrometer is on average 0.79 mm higher than D_0 estimated at 94 GHz, which is more than this 20%. This can partially be explained by the fact that the disdrometer overestimates D_m, as it is not able to measure raindrops smaller than 0.25 mm and seems to underestimate the amount of raindrops with a diameter between 0.25 and 0.375 mm. However, because D_0 values retrieved from 35 GHz data are also higher than the ones at 94 GHz, further research, which can use all the methodologies proposed in this master thesis work, is needed to examine the quantitative values of the median volume diameter retrieval.

6.2. Answer to the Main Research Question

"How can the median volume diameter be retrieved using a polarimetric cloud radar?"

The gamma model parameterized by (D_0, μ, N_w) is assumed for the raindrop size distribution. For the retrieval of the median volume diameter (D_0), radar variables independent of N_w, should be considered. There are two candidates, the differential reflectivity (Z_{dr}) and the differential backscatter phase (δ_{co}). Z_{dr} values are very small at 94 GHz, and depend on polarimetric calibration (two disadvantages). Therefore, the choice goes to δ_{co}. However, to obtain δ_{co}, first propagation and backscattering effects need to be disentangled. This is done by finding the Rayleigh plateau, which is a part of the Doppler spectrum that corresponds to small raindrops and consequently to propagation effects only, as δ_{co} is zero for Rayleigh scattering. An algorithm, which automatically detects the Rayleigh plateau is proposed. This results in the estimation of the differential propagation phase. With the calculated differential propagation phase and the measured differential phase, the differential backscatter phase can be estimated. The uncertainty of the retrieved differential backscatter phase is obtained by using the re-sampling method bootstrapping, which provides the 95% confidence interval of δ_{co}. Simulations show what value of δ_{co} corresponds to combinations of possible values of D_0 and μ. The confidence interval of δ_{co} of both frequency bands restrict the value of D_0, while μ is often not restricted. The overlap between the possible combinations of D_0 and μ at 35 and 94 GHz can restrict D_0 even more and can even restrict μ in some cases. However, often, no overlap is found. The median volume diameter retrieved with only 35 and 94 GHz frequency bands shows a good correlation with the measured D_m of the disdrometer. Therefore, the cloud radar seems to have the capability to provide the detailed variations of the raindrops mean/median diameter like a local disdrometer, but at different heights. However, the D_m of the disdrometer is significantly larger than D_0. Partial explanations are: by definition, D_m is slightly larger than D_0 and the disdrometer overestimates D_m, as it cannot measure well the small raindrops. Consequently, the next research questions should address the quantitative values of the D_0 retrieval and the non-overlapping between the solutions at 94 and 35 GHz. At last, by investigating other cloud radar variables, similar approaches could be followed to retrieve the other two variables of the gamma-modeled raindrop size distribution: μ and N_w.

6.3. Recommendations

Since the used polarimetric cloud radar was a new cloud radar and since there is no literature available where the rain drop size distribution is retrieved with a polarimetric cloud radar, this was a challenging research. This section will give suggestions for what is recommended to do in further research in this topic:

- Investigate why the retrieved D_0 at 35 and 94 GHz are significantly lower than D_m calculated with disdrometer measurements. To do this, one can use the recommendations listed in subsection 5.4.5.
- Use simulations of δ_{co} versus D_m and μ to provide D_m instead of D_0 to be able to compare the results better with disdrometer measurements.
- Investigate how accurate the estimated error of δ_{co} and D_0 is and find a more accurate way of estimating the errors if needed.
- Improve the estimation of the specific differential phase, as the specific different phase might be useful for a raindrop size distribution retrieval. Using the extra polarimetric calibration correction is highly recommended.
- Explore more variables which might be effective to retrieve μ or N_w. For power measurements, the differential attenuation might help to retrieve N_w, especially when D_0 is already retrieved.

Bibliography

[1] K. A. Teague and N. Gallicchio, “The evolution of meteorology: A look into the past, present, and future of weather forecasting,” 2017.

[2] S. Abel and I. Boutle, “An improved representation of the raindrop size distribution for single-moment microphysics schemes,” *Quarterly Journal of the Royal Meteorological Society*, vol. 138, no. 669, pp. 2151–2162, 2012.

[3] A. Tokay, W. A. Petersen, P. Gatlin, and M. Wingo, “Comparison of raindrop size distribution measurements by collocated disdrometers,” *Journal of Atmospheric and Oceanic Technology*, vol. 30, no. 8, pp. 1672–1690, 2013.

[4] M. Thurai, V. Bringi, P. N. Gatlin, W. A. Petersen, and M. T. Wingo, “Measurements and modeling of the full rain drop size distribution,” *Atmosphere*, vol. 10, no. 1, p. 39, 2019.

[5] E. Gorgucci, V. Chandrasekar, V. Bringi, and G. Scarchilli, “Estimation of raindrop size distribution parameters from polarimetric radar measurements,” *Journal of the Atmospheric Sciences*, vol. 59, no. 15, pp. 2373–2384, 2002.

[6] G. Zhang, J. Vivekanandan, and E. Brandes, “A method for estimating rain rate and drop size distribution from polarimetric radar measurements,” *IEEE Transactions on Geoscience and Remote Sensing*, vol. 39, no. 4, pp. 830–841, 2001.

[7] M. Hall, S. Cherry, J. Goddard, and G. Kennedy, “Rain drop sizes and rainfall rate measured by dual-polarization radar,” *Nature*, vol. 285, no. 5762, pp. 195–198, 1980.

[8] A. Illingworth and I. Caylor, “Polarization radar estimates of raindrop size spectra and rainfall rates,” *Journal of Atmospheric and Oceanic Technology*, vol. 6, no. 6, pp. 939–949, 1989.

[9] V. N. Bringi and V. Chandrasekar, *Polarimetric Doppler weather radar: principles and applications*. Cambridge university press 2004, 2001.

[10] R. Lhermitte, “A 94-ghz doppler radar for cloud observations,” *Journal of Atmospheric and Oceanic Technology*, vol. 4, no. 1, pp. 36–48, 1987.

[11] P. Kollias, N. Bharadwaj, E. Clothiaux, K. Lamer, M. Oue, J. Hardin, B. Isom, I. Lindenmaier, A. Matthews, E. Luke, *et al.*, “The arm radar network: At the leading edge of cloud and precipitation observations,” *Bulletin of the American Meteorological Society*, vol. 101, no. 5, E588–E607, 2020.

[12] E. E. Clothiaux, T. P. Ackerman, and D. M. Babb, “Ground-based remote sensing of cloud properties using millimeter-wave radar,” in *Radiation and Water in the Climate System*, Springer, 1996, pp. 323–366.

[13] L. Liao and K. Sassen, “Investigation of relationships between ka-band radar reflectivity and ice and liquid water contents,” *Atmospheric research*, vol. 34, no. 1-4, pp. 231–248, 1994.

[14] E. Marinou, F. Ewald, S. Gross, M. Wirth, A. Schaefler, Q. Cazenave, and J. Delanoë, “Aerosol-cloud target classification in halo lidar/radar collocated measurements,” in *EPJ Web of Conferences*, EDP Sciences, vol. 237, 2020, p. 08 002.

[15] R. Lhermitte, “Attenuation and scattering of millimeter wavelength radiation by clouds and precipitation,” *Journal of Atmospheric and Oceanic Technology*, vol. 7, no. 3, pp. 464–479, 1990.

[16] H. J. Griesche, P. Seifert, A. Ansmann, H. Baars, C. B. Velasco, J. Bühl, R. Engelmann, M. Radenz, and Y. Zhenping, “Application of the shipborne remote sensing supersite oceanet for profiling of arctic aerosols and clouds during polarstern cruise ps106,”

[17] L. Yang, Y. Wang, Z. Wang, Q. Yang, X. Fan, F. Tao, X. Zhen, and Z. Yang, “Automatic identification of clear-air echoes based on millimeter-wave cloud radar measurements,” *Advances in Atmospheric Sciences*, vol. 37, no. 8, pp. 912–924, 2020.

[18] S. Y. Matrosov, “Attenuation-based estimates of rainfall rates aloft with vertically pointing ka-band radars,” *Journal of Atmospheric and Oceanic Technology*, vol. 22, no. 1, pp. 43–54, 2005.

[19] A. Chandra, C. Zhang, P. Kollias, S. Matrosov, and W. Szyrmer, “Automated rain rate estimates using the ka-band arm zenith radar (kazr),” *Atmospheric Measurement Techniques*, vol. 8, no. 9, pp. 3685–3699, 2015.

[20] P. Kollias, B. Albrecht, and F. Marks Jr, “Cloud radar observations of vertical drafts and microphysics in convective rain,” *Journal of Geophysical Research: Atmospheres*, vol. 108, no. D2, 2003.

[21] P. Kollias, B. Albrecht, and F. Marks Jr, “Why mie? accurate observations of vertical air velocities and raindrops using a cloud radar,” *Bulletin of the American Meteorological Society*, vol. 83, no. 10, pp. 1471–1484, 2002.

[22] P. Kollias, “Cloud radar observations of precipitation,” in *Proceedings of ERAD*, vol. 126, 2002.

[23] R. M. Lhermitte, “Observation of rain at vertical incidence with a 94 ghz doppler radar: An insight on mie scattering,” *Geophysical Research Letters*, vol. 15, no. 10, pp. 1125–1128, 1988.

[24] F. Tridon, A. Battaglia, and P. Kollias, “Disentangling mie and attenuation effects in rain using a ka-w dual-wavelength doppler spectral ratio technique,” *Geophysical Research Letters*, vol. 40, no. 20, pp. 5548–5552, 2013.

[25] F. Tridon and A. Battaglia, “Dual-frequency radar doppler spectral retrieval of rain drop size distributions and entangled dynamics variables,” *Journal of Geophysical Research: Atmospheres*, vol. 120, no. 11, pp. 5585–5601, 2015.

[26] J. M. Firda, S. M. Sekelsky, and R. E. McIntosh, “Application of dual-frequency millimeter-wave doppler spectra for the retrieval of drop size distributions and vertical air motion in rain,” *Journal of Atmospheric and Oceanic Technology*, vol. 16, no. 2, pp. 216–236, 1999.

[27] S. Y. Matrosov, “Characteristic raindrop size retrievals from measurements of differences in vertical doppler velocities at ka-and w-band radar frequencies,” *Journal of Atmospheric and Oceanic Technology*, vol. 34, no. 1, pp. 65–71, 2017.

[28] A. Myagkov, S. Kneifel, and T. Rose, “Evaluation of the reflectivity calibration of w-band radars based on observations in rain,” *Atmospheric Measurement Techniques*, vol. 13, no. 11, pp. 5799–5825, 2020.

[29] S. Trömel, M. R. Kumjian, A. V. Ryzhkov, C. Simmer, and M. Diederich, “Backscatter differential phase—estimation and variability,” *Journal of applied meteorology and climatology*, vol. 52, no. 11, pp. 2529–2548, 2013.

[30] C. M. H. Unal, “Scattering simulation for cloud radar data,” *Internal Report at Delft University of Technology*, 2021.

[31] C. Gatidis, M. Schleiss, C. Unal, and H. Russchenberg, “A critical evaluation of the adequacy of the gamma model for representing raindrop size distributions,” *Journal of Atmospheric and Oceanic Technology*, vol. 37, no. 10, pp. 1765–1779, 2020.

[32] *Confidence intervals*. [Online]. Available: `http://www.stat.yale.edu/Courses/1997-98/101/confint.htm#:~:text=For%20a%20population%20with%20unknown%20mean%20and%20unknown%20standard%20deviation,t(n-1).`.

[33] B. Ci and R.-O. Rule, “Confidence intervals,” *Lancet*, vol. 1, no. 8531, pp. 494–7, 1987.

[34] A. Green, “An approximation for the shapes of large raindrops,” *Journal of Applied Meteorology and Climatology*, vol. 14, no. 8, pp. 1578–1583, 1975.

Appendix A - Non Used Parameters

A.1. Power Based Parameters

A.1.1. Linear Depolarization Ratio

Very similar to the differential reflectivity, there is the linear depolarization ratio. The linear depolarization ratio is defined as the measured reflected vertically polarized electromagnetic wave after transmitting a horizontally polarized electromagnetic wave (which scatters) divided by the vertically polarized transmitted and measured electromagnetic wave:

$$l_{dr} = \frac{\left\langle |S_{vh}|^2 \right\rangle}{\left\langle |S_{vv}|^2 \right\rangle} = \frac{z_{vh}}{z_{vv}} \tag{A.1}$$

and often used in dB:

$$L_{dr} = 10\log_{10}(z_{vh}) - 10\log_{10}(z_{vv}) = Z_{vh} - Z_{vv} \tag{A.2}$$

The linear depolarization ratio depends on the particle shape, orientation and relative permittivity. When one takes a constant shape ratio (b/a), L_{dr} strongly depends on the relative permittivity. For rain, L_{dr}< -27 dB, which is difficult to measure. The melting layer is between -20 dB and -10 dB, therefore, it is a good melting layer detector. Hail stone will lead to L_{dr}> -20 dB. Figure A.1 shows the slanted linear depolarization ratio of the 35 GHz and 94 GHz radar.

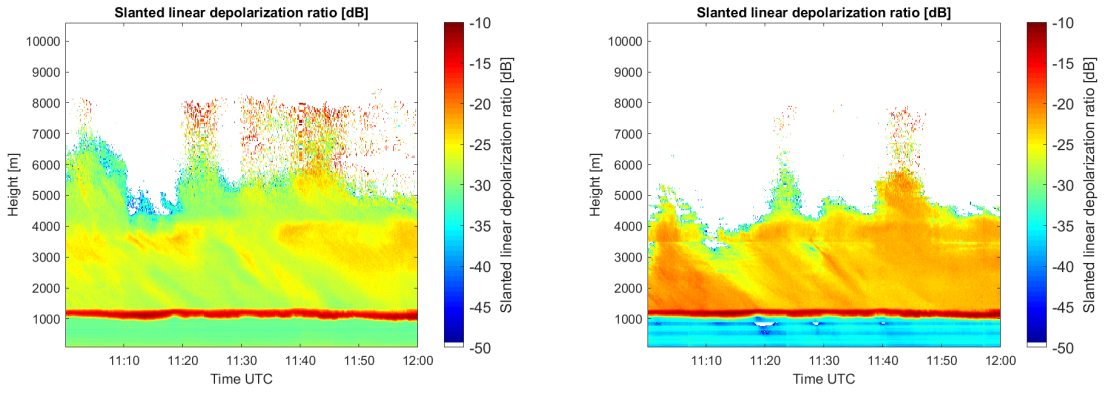

(a) 35 GHz (b) 94 GHz

Figure A.1: Slanted linear depolarization ratio of the 35 GHz and 94 GHz radar.

A.2. Phase Based Parameters

A.2.1. Mean Doppler Velocity and Spectrum Width

The Doppler effect can be used to determine the velocity component of an object in the radial direction from the radar. When an object is moving towards the radar, the frequency of the reflection will be higher than the incoming frequency, this is called blueshifting. When an object is moving away from the radar, the frequency of the reflection will be lower than the incoming frequency, this is called red-shifting. In practise, we do not measure the frequency directly, but we measure the phase over time and can derive the frequency from this and thus also the frequency shift. With this frequency shift, one can calculate the velocity component of an object in the radial direction from the radar.

In practise, however, one does not measure the reflection of one target, but of a lot of targets at the same time. This means that a statistical approach is required to obtain velocity information. Usually, a wide sense stationary random process is assumed. There are two possible approaches, the first is taking the fast Fourier transform of the measured signal and then taking the modules squared. The second option is to use the autocorrelation function of the measured signal and then taking the fast Fourier transform. The obtained result is called a periodogram, also P(f). From this periodogram, some other statistical parameters can be obtained. The easiest one to obtain is the total power:

$$P = \int P(f)df \tag{A.3}$$

The next statistical parameter is the mean Doppler frequency:

$$f_D = \frac{1}{P}\int fP(f)df \tag{A.4}$$

and the last one is the Doppler spectrum width:

$$\sigma_{f_D} = \sqrt{\frac{1}{P}\int (f - f_D)^2 P(f)df} \tag{A.5}$$

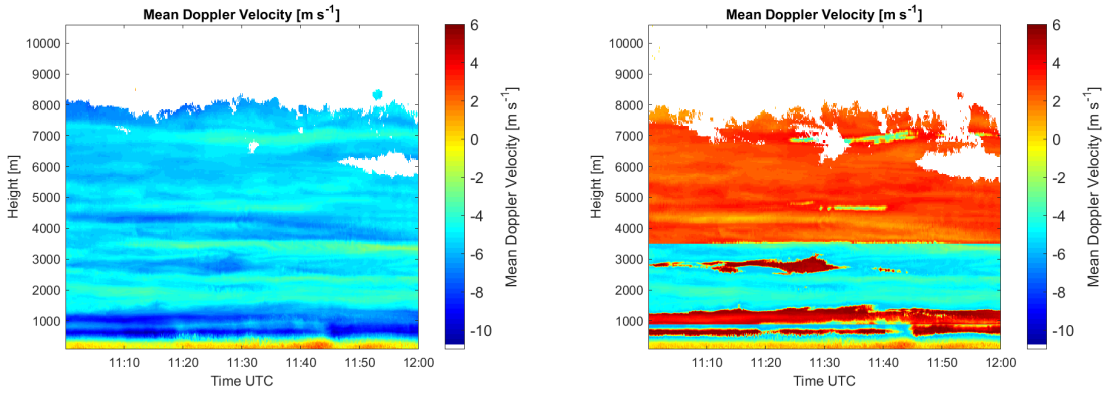

(a) 35 GHz (b) 94 GHz

Figure A.2: Mean Doppler Velocity of the 35 GHz and 94 GHz radar.

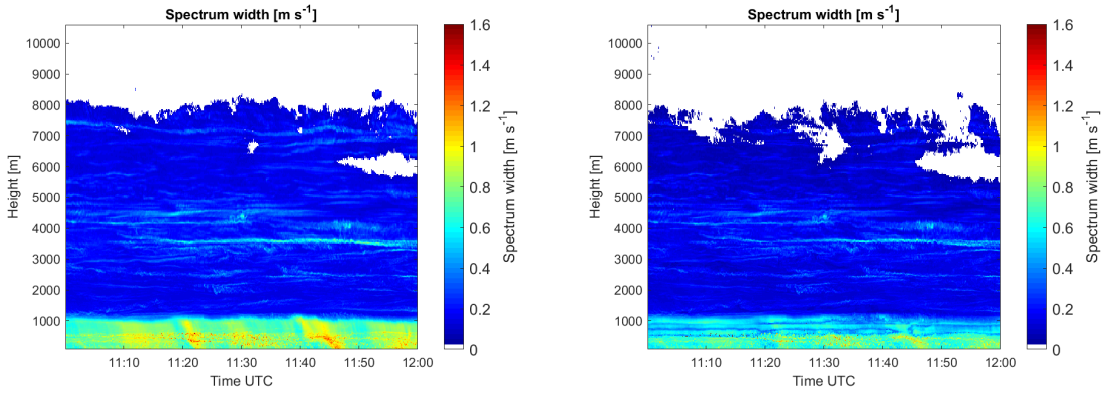

(a) 35 GHz (b) 94 GHz

Figure A.3: Spectrum width of the 35 GHz and 94 GHz radar.

A.3. Remaining Parameters without Explanation

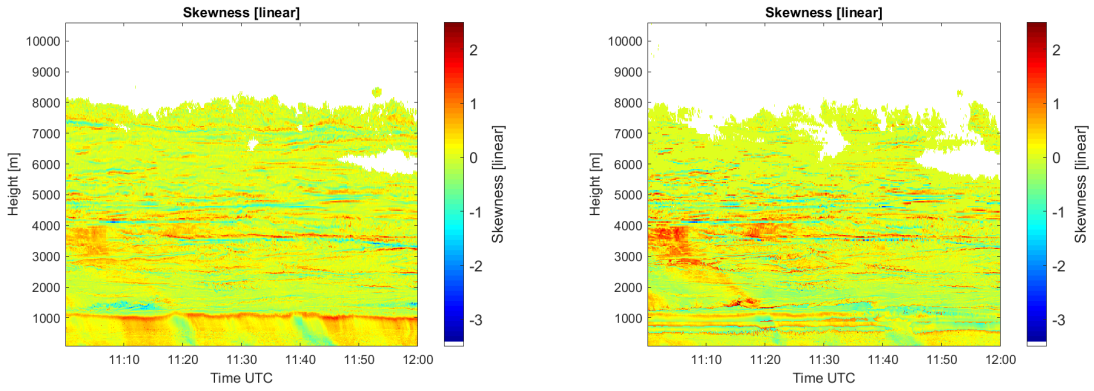

(a) 35 GHz (b) 94 GHz

Figure A.4: Skewness of the 35 GHz and 94 GHz radar.

B

Appendix B - Polarimetric Calibration Correction Table

Table B.1: Polarimetric calibration corrections for the differential reflectivity z_{dr} and the differential (propagation) phase for the 35 GHz and the 94 GHz frequency bands and their corresponding margin of error (95% confidence) calculated as explained in section 3.6

Height [m]	zdr 35 GHz [-]	error zdr 35 GHz [-]	zdr 94 GHz [-]	error zdr 94 GHz [-]	Φ_{dp} 35 GHz [deg]	error Φ_{dp} 35 GHz [deg]	Φ_{dp} 94 GHz [deg]	error Φ_{dp} 94 GHz [deg]
84.3	0.0521	0.00012	0.0058	0.00014	2.366	0.003	0.62	0.0108
105.4	0.043	0.00012	-0.0078	0.00015	2.565	0.003	0.62	0.0108
126.5	0.034	0.00008	-0.0049	0.00011	2.611	0.003	0.61	0.0108
147.6	0.032	0.00008	-0.0079	0.00016	2.581	0.003	0.61	0.0107
168.7	0.033	0.00008	-0.0127	0.00015	2.520	0.003	0.61	0.0107
189.8	0.033	0.00008	-0.0198	0.00013	2.449	0.003	0.61	0.0107
210.8	0.035	0.00007	-0.0208	0.00015	2.375	0.003	0.61	0.0107
231.9	0.033	0.00010	-0.0205	0.00016	2.305	0.003	0.61	0.0107
253.0	0.031	0.00014	-0.0222	0.00012	2.232	0.003	0.61	0.0107
274.1	0.031	0.00013	-0.0193	0.00019	2.162	0.003	0.61	0.0106
295.2	0.033	0.00011	-0.0158	0.00015	2.096	0.003	0.61	0.0106
316.3	0.031	0.00007	-0.0188	0.00017	2.031	0.003	0.60	0.0106
337.3	0.032	0.00007	-0.0178	0.00019	1.969	0.003	0.60	0.0107
358.4	0.032	0.00009	-0.0196	0.00017	1.908	0.003	0.60	0.0106
379.5	0.031	0.00005	-0.0191	0.00024	1.848	0.003	0.60	0.0106
400.6	0.030	0.00009	-0.0199	0.00015	1.785	0.003	0.59	0.0104
421.7	0.034	0.00015	-0.0166	0.00020	1.720	0.003	0.59	0.0105
442.8	0.034	0.00015	-0.0165	0.00015	1.653	0.003	0.59	0.0103
463.8	0.035	0.00008	-0.0125	0.00018	1.581	0.003	0.59	0.0100
484.9	0.034	0.00011	-0.0082	0.00011	1.503	0.003	0.59	0.0099
506.0	0.035	0.00008	-0.0062	0.00022	1.419	0.003	0.59	0.0099
527.1	0.034	0.00010	-0.0100	0.00015	1.328	0.003	0.58	0.0099
548.2	0.035	0.00009	-0.0145	0.00016	1.231	0.003	0.58	0.0100
569.3	0.031	0.00011	-0.0153	0.00020	1.129	0.004	0.57	0.0102
590.3	0.034	0.00009	-0.0158	0.00025	1.021	0.003	0.57	0.0100
611.4	0.031	0.00017	-0.0194	0.00012	0.908	0.003	0.57	0.0100
632.5	0.034	0.00015	-0.0202	0.00021	0.794	0.003	0.57	0.0100
653.6	0.034	0.00007	-0.0219	0.00023	0.684	0.003	0.57	0.0100
674.7	0.035	0.00010	-0.0226	0.00017	0.584	0.003	0.56	0.0100
695.8	0.035	0.00018	-0.0236	0.00017	0.501	0.003	0.56	0.0100
716.8	0.038	0.00021	-0.0245	0.00016	0.446	0.003	0.55	0.0100
737.9	0.036	0.00011	-0.0239	0.00015	0.433	0.003	0.55	0.0101
759.0	0.037	0.00013	-0.0214	0.00017	0.483	0.003	0.54	0.0103
780.1	0.039	0.00019	-0.0137	0.00014	0.614	0.003	0.54	0.0100
801.2	0.037	0.00010	-0.0127	0.00022	0.845	0.003	0.53	0.0106
822.3	0.033	0.00012	-0.0133	0.00016	1.179	0.006	0.52	0.0112
843.4	0.033	0.00006	-0.0120	0.00026	1.658	0.006	0.51	0.0121
864.4	0.037	0.00016	-0.0230	0.00023	1.717	0.004	0.86	0.0152
885.5	0.036	0.00023	-0.0226	0.00012	1.692	0.004	0.85	0.0156
906.6	0.034	0.00025	-0.0231	0.00011	1.659	0.006	0.85	0.0159

C

Appendix C - Specific Differential Reflectivity

The previous chapter focused on estimating δ_{co}, which can be used to estimate D_0. The first estimate of K_{dp} turned out to be unusable for the retrieval of D_0, μ or N_w as the estimate of K_{dp} was highly affected by noise. The way of estimating K_{dp} should thus be improved. Further, K_{dp} has little sensitivity to μ and lacks in sensitivity to D_0 and N_w for small D_0 and N_w values. Thus, other variables need to be found to be able to estimate N_w and μ, which cannot be determined by δ_{co}. In this chapter, a self-invented variable will be introduced and it will be discussed whether this variable has the potentiality to be useful for a raindrop size distribution retrieval. This variable will be referred to as the specific differential reflectivity (K_{dr}) and is defined in the following way:

$$K_{dr} = \frac{1}{2}\left(\frac{dz_{hh}}{dr} - \frac{dz_{vv}}{dr}\right) = \frac{1}{2}\frac{d\mathrm{P}_{dr}}{dr} \approx \frac{1}{2}\frac{\mathrm{P}_{dr}(r_2) - \mathrm{P}_{dr}(r_1)}{r_2 - r_1} \tag{C.1}$$

where

$$\mathrm{P}_{dr} = z_{hh} - z_{vv} \tag{C.2}$$

where K_{dr} is the specific differential reflectivity in mm^6/m^4 and P_{dr} is the difference in equivalent reflectivity between the horizontal and vertical polarization in mm^6/m^3, which is not equal to the differential reflectivity, as that is calculated by taking the ratio and not by taking the difference (when using linear values). In Figure C.1, one can see an example plot of the specific differential reflectivity as a function of height and time for the 35 GHz and 94 GHz frequency band. One can clearly see that the height bins that correspond to the lowest 150 meters show different behaviour than the higher height bins, like also happened for the differential backscatter phase in section 4.2. These first height bins of K_{dr} especially show more extreme values. Again, a possible explanation is that the far-field approximation for polarimetric measurements is not valid. In section 4.2, an other mentioned possible explanation was that the polarimetric calibration is not valid at these heights. For K_{dp}, this explanation is not possible, as no extra polarimetric calibration correction was applied for it. However, it might be good to apply an extra polarimetric calibration. The same polarimetric calibration procedure as applied to z_{dr} and Ψ_{dp} is also possible for P_{dr}. P_{dr}, which is equal to $z_{hh} - z_{vv}$, is expected to be 0 mm^6/m^3 for drizzle measurements, as z_{hh} is expected to be the same as z_{vv} in drizzle, as all rain drops are close to spherically shaped in drizzle. In this research, this calibration correction was not applied, because the focus was given to estimating δ_{co} to be able to estimate D_0 and the limited time of the master thesis research.

When exploring the new variable (K_{dr}), it was notable that this variable might be related to the rainfall rate. To investigate this, the mean over height of the specific differential reflectivity is plotted as a function of time. The mean is taken to reduce noise effects and calculating this mean implies the assumption that the rainfall rate is about constant with height. The lowest 4 height bins are not used for this averaging, as these show unexpected behaviour, as mentioned before. The resulting plots

can be seen in Figure C.2. One can see that K_{dr} at 35 GHz seem to be correlated to the rainfall rate (Figure C.3), as local peaks at Figure C.2(a) often correspond to local peaks at Figure C.3. Moreover, the up- and downward small time trends seem to be the same in these figures. The trend over the whole hour, however, is not the same, as the rainfall rate clearly increases over time during this hour, while this is not clear for K_{dr} at 35 GHz. More research on K_{dr} has to be done to find out if this variable might be useful for a raindrop size distribution retrieval or a rainfall rate retrieval. Creating simulations is advised to get a better understanding of this rather complex variable.

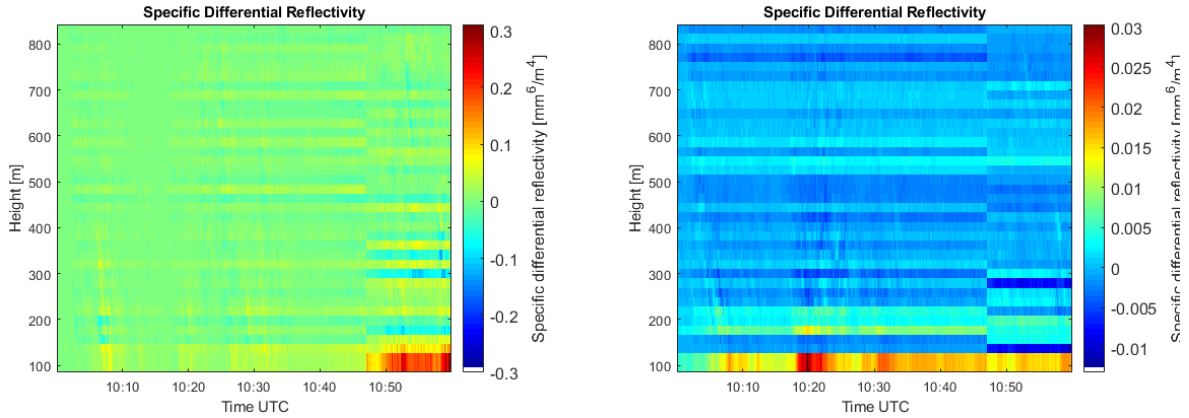

(a) 35 GHz (b) 94 GHz

Figure C.1: The specific differential reflectivity as a function of height and time for the 35 GHz band and 94 GHz band.

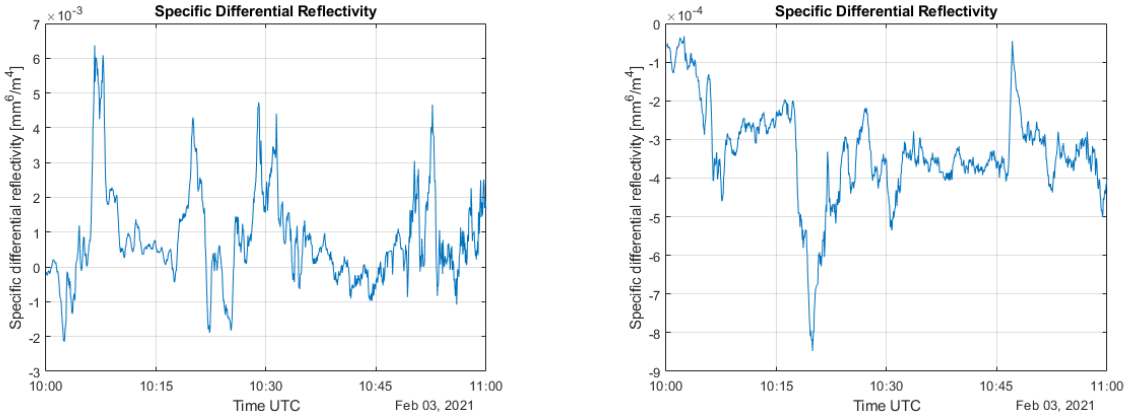

(a) 35 GHz (b) 94 GHz

Figure C.2: The mean specific differential reflectivity between 179 m height and 833 m height as a function of time for the 35 GHz band and 94 GHz frequency band.

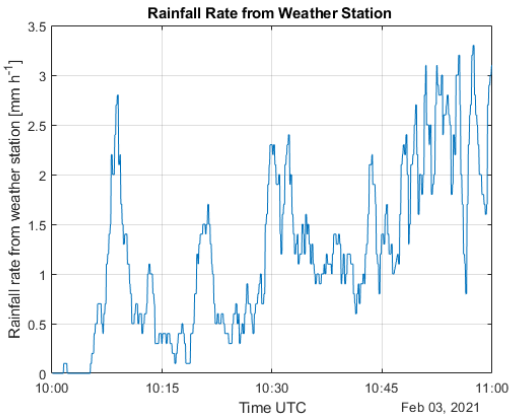

Figure C.3: Rainfall rate at the third of February 2021 measured from the weather station on the cloud radar.